UNIVERSITE DE LIMOGES

ECOLE DOCTORALE Science et Ingénierie en Matériaux, Mécanique, Energétique et Aéronautique (SI-MMEA)

Groupe d'Etude des Matériaux Hétérogènes

Thèse N° [94]

Thèse
pour obtenir le grade de
DOCTEUR DE L'UNIVERSITÉ DE LIMOGES
Discipline / Spécialité : Matériaux céramiques et traitements de surface

Présentée et soutenue par
Renaud GRASSET-BOURDEL

le 24 Novembre 2011 à Leoben (Autriche)

Structure/property relations of magnesia-spinel refractories: experimental determination and simulation

---

Thèse dirigée par : Marc HUGER et Thierry CHOTARD

JURY :

Rapporteurs :

M. T. Cutard	Maître-Assistant HDR	ICA-Albi, Mines d'Albi
M. H. Harmuth	Professeur des Universités	Chair of Ceramics, Montanuniversität (Autriche)

Examinateurs :

M. T. Chotard	Professeur des Universités	GEMH, Université de Limoges
M. M. Huger	Professeur des Universités	GEMH, ENSCI
M. P. Kirschenhofer	Professeur des Universités	Chair of Mathematics and Statistics, Montanuniversität (Autriche)

To my brother Julien

Acknowledgments

This work has been accomplished in the context of collaboration between the department of the Heterogeneous Materials Research Group (G.E.M.H.) of the Centre Européen de la Céramique (Limoges, France) and the Chair of Ceramics (Department Mineral Resources and Petroleum Engineering) of the Montanuniversität (Leoben, Austria). I gratefully acknowledge the Austrian Federal Government and the Styrian Provincial Government (Österreichische Forschungsförderungsgesellschaft and Steirische Wirtschaftsförderungsgesellschaft) within the K2 Competence Centre on "Integrated Research in Materials, Processing and Product Engineering" (MCL Leoben) in the framework of the Austrian COMET Competence Centre Programme, for its financial support.

This study would not have been possible without the guidance of my French and Austrian supervisors.

First and foremost, I would like to express my utmost gratitude to Prof. Marc Huger (GEMH, Limoges) for all the scientific helpful discussions we had since my Master's study, his availability and his confidence in my work. His high requirements have helped me not to stop questioning and always trying to look for solutions to, a-priori, unsolvable problems.

I also would like to thank Prof. Harald Harmuth (Chair of Ceramics, Leoben) for his scientific rigor and for having explained to me many things related, for example, to basic refractories or fracture mechanics. His very interesting remarks and the freedom he gave me during these three years are also acknowledged.

I am also grateful to Prof. Thierry Chotard (GEMH, Limoges) for his help concerning various scientific and administration aspects, and his encouragement.

I also acknowledge Dr. Dietmar Gruber (Chair of Ceramics, Leoben) for many aspects of my PhD but, first of all, for having been my main foreign interlocutor when I was in France and for having presented my work several times in some internal meetings.

I could not forget to thank Dr. Arnaud Alzina, newly arrived at the G.E.M.H. at the end of my first year of PhD, who introduced me in the Linux environnement, proposed me to work with

the Code Aster software package, brought me his support concerning python programming and many other things.

Of course, I would like to thank several people who in one way or another also contributed and extended their valuable assistance in the preparation and completion of this study. Thanks to Prof. Nicolas Schmitt (LMT, ENS Cachan), for his help concerning numerical homogenisation methods and his scientific rigor, Dr. Nicolas Tessier-Doyen (GEMH, Limoges), for having provided me some of his experimental results needed in a preliminary numerical work and for his support, and Mr Robert Emler (Chair of Ceramics, Leoben), for the elaboration of the magnesia based materials studied in the present work, as well as the performed wedge splitting tests.

Furthermore, I am grateful to the academic and industrial partners which were involved in this project. For that, I thank Prof. Michel Rigaud (Federation for International Refractory Research and Education FIRE), Prof. Reinhold Ebner (Materials Center Leoben MCL), Mr. Bernd Buchberger (RHI AG), Mr. Roman Roessler (Voestalpine AG) and Mr Marc Fréchette (Pyrotek Inc).

These last three years, mostly spent in Limoges, would not have been the same without the good atmosphere prevailing among the PhD students, and engineers, at the G.E.M.H. laboratory. I have a special thought for the “US team” with Cédric, Alexandra and Romuald, with whom I spent very good time and, sometimes, studious hours concerning some experimental devices. I will not forget all the activities shared with them, as well as with Aurélien, Elodie, Marianne, Samir, Sarah, Stéphanie, Younes, Emilie... and many others. Thanks to all of you for these good memories!

Last but not least, I would like to thank my parents, my grand-parents, my twin brother Romain and my future wife Monika, for their moral support and their love.

Table of Content

General introduction

Due to their large panel of applications, refractory materials are used in many industrial areas such as the steel, cement, lime, non-ferrous metals and glass processing. Indeed, they can provide, first, high temperature resistance to specific parts required for many industrial installations. Moreover, if well selected, in accordance with the desired application, refractory materials can also ensure enhanced resistance against corrosion mechanisms and external mechanical loads. These features are essential to both increase the security of workers and save production costs. Nevertheless, in the special case of thermal shock applications, involving high local thermal stresses, the fulfilment of these previous required specifications is not sufficient to select the more appropriate refractory material. The thermal shock resistance of refractories is an old issue, but still not fully explored, known to be closely related to the crack growth resistance of such materials, as well as their mechanical behaviour which deviates from pure linear elasticity when increasing strain. Indeed, the mechanical behaviour of refractories, most of the time, do not fulfil the main conditions of pure linear elasticity since the relation between stress and strain is not proportional, irreversible strain occurs when unloading and the consumed energy is not only located in front of the crack tip but also behind it. To simplify the denomination, this specific behaviour will be called “non-linear mechanical behaviour” in the present thesis. The improvement of thermal shock resistance of refractories requires a better understanding of the relationships existing between the microstructure and the associated thermo-mechanical properties, at macroscopic scale.

In order to investigate these microstructure/property relationships, previous works at the Heterogeneous Materials Research Group (GEMH, Limoges, France) were carried out, proposing to consider model two-phase materials with simple microstructure, namely glass-alumina composites, with thermal expansion mismatch. Indeed, these model materials, much less complex than industrial ones, allowed to get preliminary experimental and numerical results concerning the identification of parameters influence, in relation with the microstructure. Nonetheless, in order to improve the knowledge of real refractory materials, other closer model materials have to be considered.

Otherwise, previous studies were carried out at the Chair of Ceramics of Leoben (CoC, Leoben, Austria) in order to investigate the fracture behaviour of industrial refractory materials, mainly magnesia-based ones (ex: magnesia-chromite, magnesia-MA spinel, magnesia-carbon materials, etc.), showing the interest of using the so-called wedge splitting test [TSC-91]. Moreover, in close collaboration with industry, many numerical studies have also been done, for several years, so as to bring solutions to industrial issues. Nevertheless, these simulations, at the industrial structure scale, did not consider the microstructure of the refractory materials.

One of the challenges of this co-supervised PhD thesis was to combine the different experiences of these two laboratories, and go beyond their previous results by investigating new directions and using new numerical tools.

The first chapter is dedicated to establish the state of the art concerning thermal shock of refractory materials. After presenting the different possible origins of thermal stresses, the well known thermo-elastic and energetic analytical approaches are briefly presented with their limitations. The non-linear mechanical behaviour and crack growth resistance of refractories are, then, discussed and possible routes of improving the thermal shock resistance are given. The progress in numerical approaches and resources is presented as a promising support to reach this goal.

In Chapter II, the two-phase materials considered in the study, namely thermally damaged magnesia-spinel composites, but also non-thermally damaged glass-alumina composites, are presented. Furthermore, the experimental characterisation techniques, mainly used to determine the elastic properties at high temperature and the mechanical behaviour in tension, are also detailed, as well as the numerical homogenisation method chosen for the simulation part of this work to assess the effective thermo-elastic properties of the modelled composites.

The main objective of the preliminary numerical work, detailed in Chapter III, is to find a suitable Representative Volume Element (R.V.E.) for the design of the studied two-phase materials which should remain as simple as possible, i.e. minimising the calculation time and consumed resources, in order to be able to consider damage in a further step (Chapter V). Therefore, in this part, only linear elastic mechanical behaviour is considered and the numerical results, obtained with the periodic homogenisation method, are compared to the experimental ones obtained on the non-thermally damaged glass-alumina composites.

In Chapter IV, the magnesia-spinel composites, with different spinel inclusions contents, are experimentally characterised. The thermo-elastic properties are determined at local and macroscopic scale in order, first, to collect data allowing to assign material properties in simulations but, also, to highlight and quantify, if possible, the thermal damage, which occurs in such materials during the cooling stage of the process. Then, destructive mechanical tests are performed at room temperature to study the influence of the thermal history, which is closely linked to the spinel inclusions content, on the mechanical behaviour in tension of such materials.

After having studied experimentally the thermo-mechanical properties of magnesia-spinel composites in Chapter IV, numerical investigations are done, and presented in Chapter V, so as to find a way to depict well the thermal micro damage occurrence, during the cooling step, as well as the specific induced macro-mechanical behaviour. To reach this target, a numerical damage model, combined with periodic conditions, is proposed.

Chapter I. State of the art concerning the thermal shock resistance of refractories

I. Possible origins of thermal stresses

During a thermal shock, thermal stresses are induced by different thermal strains within the material due to different possible origins.

First, at local scale, the temperature field can be assumed to be uniform. Thus, the simplest case consists of a homogeneous material with uniform initial temperature field T_0, subjected to a uniform final temperature field T_f, with external mechanical conditions preventing from free deformation (example in 1-Dimension):

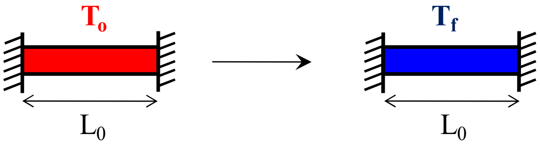

As a rule, the total strain ε_{tot} can be expressed according to the following form:

$$\varepsilon_{tot} = \varepsilon_{th} + \varepsilon_{el} \qquad \text{Eq. I-1}$$

where ε_{th} and ε_{el} are the thermal strain and the elastic strain. No residual strain is considered here.

In the present case, since the boundaries are blocked, $\varepsilon_{tot} = 0$. Thus, the expression of the elastic strain ε_{el} becomes:

$$\varepsilon_{el} = -\varepsilon_{th} = -\alpha \cdot \Delta T \qquad \text{Eq. I-2}$$

where α is the thermal expansion coefficient and ΔT is the imposed uniform temperature variation (T_f-T_0).

Then, according to the Hooke's law for the one directional case:

$$\sigma = E \cdot \varepsilon_{el} = -E \cdot \varepsilon_{th} = -E \cdot \alpha \cdot \Delta T \qquad \text{Eq. I-3}$$

where E is the Young's modulus (material assumed to be isotropic).

With free motion at the boundaries, the uniform cooling (or heating) of the sample, from T_0 to T_f, would induce a thermal contraction (or expansion) but with no stress. Here, in the case of fixed boundaries, an imposed uniform temperature variation ΔT induces a stress level σ directly related to the thermal expansion coefficient α and the Young's modulus of the material.

This simple case can be extended to a heterogeneous material with thermal expansion mismatch between the contained phases or to a homogeneous polycrystalline material with anisotropic thermal expansion for the grains. Let's consider the special case of a two-phase material composed of a matrix (m) and spherical inclusions (i). During a uniform cooling stage, from T_0 to T_f, three different configurations [TES-06] are possible depending on the sign of the difference between the thermal expansion coefficients of these two phases (Figure I-1). First, if there is no difference between the coefficients (Figure I-1 a), no internal stress appears during cooling, and thus, no damage is observed. Secondly, if the thermal expansion coefficient of the inclusions is higher than the one of the matrix (Figure I-1 b), the inclusions will contract faster than the matrix, inducing circumferential compressive stresses and radial tensile stresses. Since, in ceramics, cracks occur, most of the time, in tension, this special case will induce debonding around the inclusions. Thirdly, if the coefficient of the matrix is higher than the one of the inclusions, radial compressive stresses will appear during cooling, as well as circumferential tensile stresses responsible for the radial matrix microcracking around the inclusions.

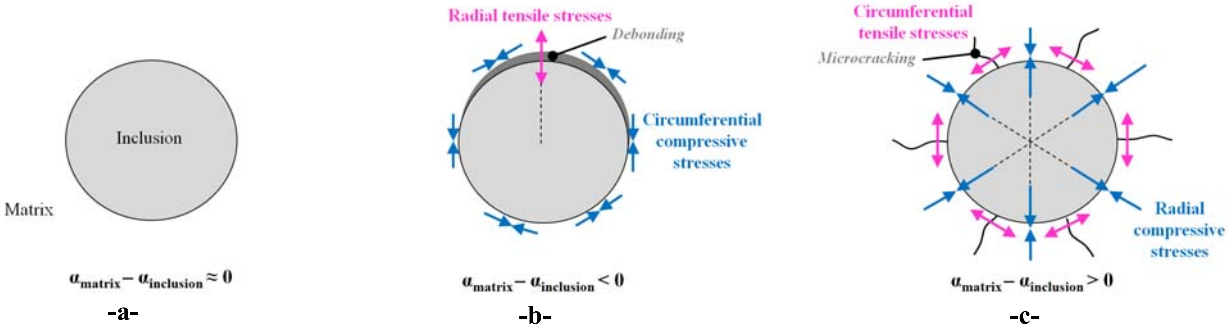

Figure I-1: Three possible configurations which can occur during cooling according to the sign of the difference between the thermal expansion coefficients of the two phases

Thermal shock (e.g. Figure I-2) is another origin of thermal stresses acting at the structure scale where the material is considered as homogeneous. Here, the differential thermal strains are caused by temperature gradients. By definition, for a solid initially at the uniform temperature T_0 and suddenly placed in a medium at the temperature $T \neq T_0$:

- if $T > T_0$, the thermal shock is a hot thermal shock,
- if $T < T_0$, the thermal shock is a cold thermal shock.

During a cold thermal shock, the surface, suddenly cooled down, tends to contract, but the centre of the sample, not cooled down yet, prevents from the surface contraction. Therefore, tensile and compressive stresses are induced on the surface, and in the centre, respectively (Figure I-2 a). The situation is inversed in the case of an ascending thermal shock (Figure I-2 b).

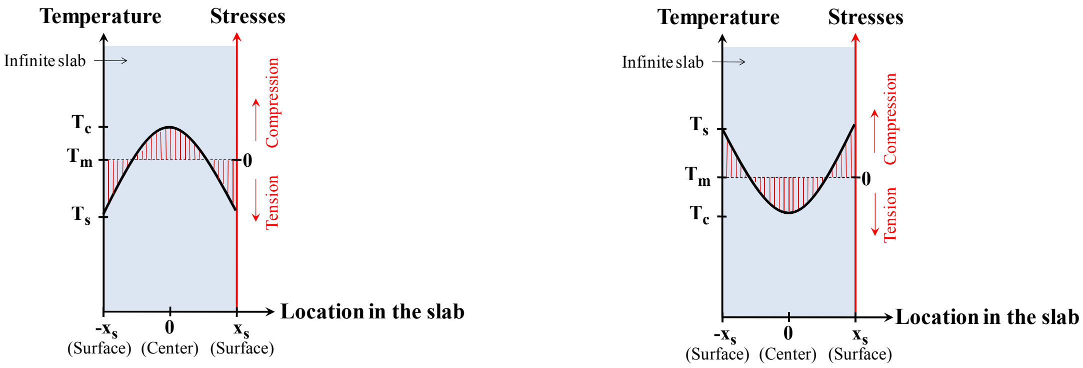

-a-

-b-

Figure I-2: Temperatures and stresses distribution within an infinite slab suddenly cooled down (a) or heated up (b) (Thermal shock)

In fact, thermal stresses resulting from a thermal shock applied on a refractory material are obviously a complex combination of the different configurations presented above. Indeed, even if a refractory material is generally assumed to be homogeneous at structure scale (to simplify calculations), one should also keep in mind that their heterogeneous microstructure also involves important effects at lower scale. Moreover, these effects within the microstructure greatly affect macroscopic properties. As the present thesis concerns the study of the microstructure-property relationships, it will essentially focus on the case where damage is caused by thermal expansion mismatch (uniform temperature). One main objective will be to study this thermal damage and its influence on the non-linearity of the mechanical behaviour (growth of a diffuse microcracks network). To do that, the case where radial microcracks occur during cooling, namely $\alpha_{matrix} > \alpha_{inclusion}$, will be chosen.

II. Fracture of refractories

II.1. Thermo-elastic approach versus energetic approach

The thermo-elastic and energetic approaches are two famous approaches developed during the 50’s and the 60’s in order to deal with thermal shocks resistance in the framework of linear fracture mechanics.

The thermo-elastic approach, proposed by Kingery [KIN-55], was developed for the special case where the material is an infinite slab (initial temperature T_i) suddenly placed in a medium at a temperature T_f (see Figure I-3). The main hypotheses of this analysis are that the stress field is bi-axial, and the material is assumed to be continuous, homogeneous and isotropic with a linear elastic mechanical behaviour.

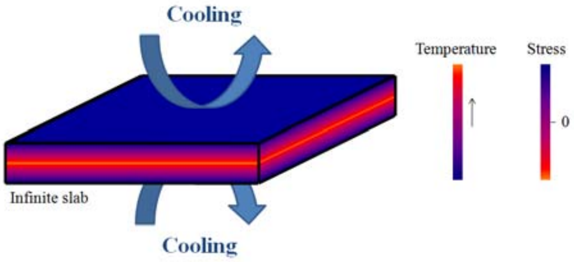

Figure I-3: Thermo-elastic approach of Kingery – Temperature and stress fields within the infinite slab in the case of a cold thermal shock

It appeared that this approach was well suited when the resistance to thermal shock consists in resisting to crack initiation. Two parameters are, thus, defined according to the rate of heat transfer. In the case of high rate of heat transfer, if the thermal stress σ_{th} becomes equal to the tensile strength σ_t of the material, then, the minimum temperature difference ΔT_c to produce fracture is reached. The first thermal shock resistance parameter R is proportional to this critical value ΔT_c and is equal to:

$$R = \frac{\sigma_t \cdot (1-\nu)}{E \cdot \alpha} \qquad \text{Eq. I-4}$$

where E, ν and α are the Young’s modulus, the Poisson’s ratio and the thermal expansion coefficient of the material, respectively.

In other words, this parameter represents the critical temperature difference for which the material can resist without any damage. In the case of low rate of heat transfer, the critical temperature difference also depends on the thermal conductivity. Therefore, a second thermal shock resistance parameter, R', was introduced so that: $R' = \lambda \cdot R$. According to these parameters, a high thermal shock resistance involves high thermal conductivity and tensile strength, and low Young's modulus and coefficient of thermal expansion. R and R' quantify the capacity to resist to crack initiation but, in case of refractory materials (with coarse grains), the capacity to resist to crack propagation is often preferred.

The energetic approach of thermal shock was introduced by Hasselman [HAS-63b, HAS-69]. In this approach, the material is assumed to present initial microcracks and the cracks stability is studied in relation with the induced thermal stresses. Since this approach is based on energy, cracks evolve towards a configuration minimising the total energy of the system. The main hypotheses of this approach are the following ones:

- Solid body with uniform state of tri-axial stress σ (uniform cooling with fixed external surfaces) of magnitude:

  $$\sigma = \frac{\alpha \cdot E \cdot \Delta T}{1 - 2 \cdot \nu}$$

  (worst possible condition of thermal stress as the body as a whole is stressed to the maximum value of thermal stress).

- The cracks are homogeneously distributed.
- The cracks are all identical: penny-shaped cracks with a length l (initial value equal to l_0).
- The propagation of all the cracks is radial and simultaneous.
- There is no interaction between stress fields of neighbouring cracks.
- There is no stress relaxation (any dislocation motion, viscous flow...).

It appeared that this approach is well suited when the resistance to thermal shock consists in resisting to crack propagation (dynamic or quasi-static). Two parameters were, thus, introduced, namely R'''' and R_{st}:

$$R'''' = \frac{\gamma_s \cdot E}{\sigma_t^2} \qquad \text{Eq. I-5} \qquad \text{and} \qquad R_{st} = \sqrt{\frac{\gamma_s}{\alpha^2 \cdot E}} \qquad \text{Eq. I-6}$$

where γ_s is the surface fracture energy of the material.

The parameter R'''' (in m) was introduced by Hasselman as a “thermal shock damage resistance parameter” [HAS-63b] in order to be able to compare the degree of damage of materials with widely different values of effective surface energies such as brittle and ductile materials. Its maximization was expected to reduce dynamic (or unstable) propagation.

The “thermal stress crack stability” parameter R_{st}, referring to the maximal temperature difference for crack initiation (in K.m$^{1/2}$), was proposed later [HAS-69]. The maximisation of this parameter by selecting suitable material properties was expected to reduce the probability of fracture initiation. In case of mild heat transfer conditions, the thermal conductivity λ is taken into account by the following parameter [HAS-69] (similarly to the R' parameter of Kingery):

$$R'_{st} = \lambda \cdot R_{st} = \lambda \cdot \sqrt{\frac{\gamma_s}{\alpha^2 \cdot E}} \qquad \text{Eq. I-7}$$

A first glance at Eq. I-5 and Eq. I-6 could make thinking that the dependency of R'''' and R_{st} on the elastic properties are opposite. But, in fact, the Young’s modulus and the strength are inseparable since they directly refer to the stored elastic strain energy (σ^2/E). Indeed, in the expression of R_{st}, the term ($\alpha^2 \cdot E$) can be replaced, by approximation, with the term (σ^2/E), which is mainly the stored elastic strain energy in an object at the stress level σ [POP-99]. Thus, the parameters R'''' and R_{st} present the same dependency on the elastic modulus and strength since they are inversely related to this stored elastic strain energy [BRA-04] which is the driving force for fracture or crack extension.

According to this approach, the crack propagation kinetics, and the loss in strength, highly depends on the pre-cracking of the material. Indeed [LAR-74], in the case of high-strength technical ceramics and glasses (Figure I-4 A and B), the loss in strength is usually catastrophic and should be related to the R'''' parameter. In the case of refractories (Figure I-4 C and D), the loss in strength is often more quasi-static, depending on the temperature difference and so, should be related to the R_{st} (or R'_{st}) parameter.

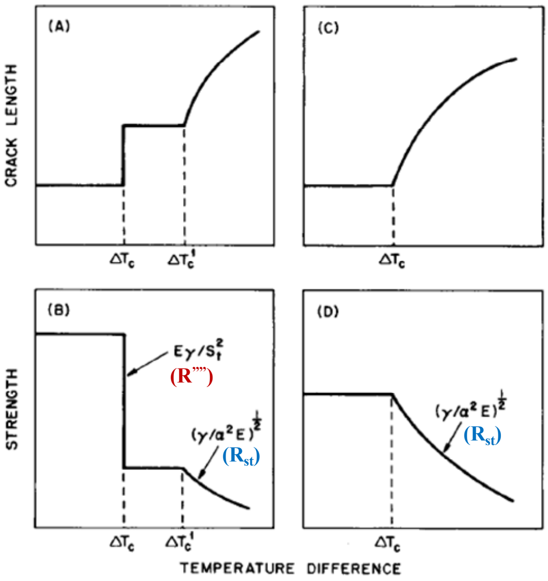

Figure I-4: Crack propagation and strength behaviour for (A) and (B) unstable and (C) and (D) stable crack propagation under conditions of thermal shock [LAR-74]

II.2. Non-linear mechanical behaviour and associated experimental techniques

The non-linear character of the mechanical behaviour (deviation from the linear elastic mechanical behaviour) of refractories is rather well known and some concepts like the brittleness number [GOG-78, HAR-97], were introduced to quantify the gap to the linear elastic case from measured fracture energies. Indeed, non-linear mechanical behaviour, reduced brittleness and rather low tensile strength (5-40 MPa) are characteristic for refractories. Some experimental techniques were then developed to measure, in particular, fracture energy.

To measure the fracture energy of brittle materials, different techniques were originally proposed. Some of them used the Griffith energy equation [GRI-20] for a two-dimensional crack [KER-62, IRW-58, SHA-61, WIE-64, BER-57]. Others developed cone fracture [ROE-56] or cleavage fracture [GIL-60] techniques. But, the main disadvantage of all these methods was their restriction to homogeneous materials. Nakayama and Ishizuka proposed the work-of-fracture technique [NAK-65, NAK-64, NAK-66], also developed by Tattersall and Tappin [TAT-66], to measure the fracture energy (γ_{WOF}) consumed to propagate a crack through a sample. This method (shown in Figure I-5a) corresponds to a three-point bending test on a sample having a special artificial crack providing stable propagation. A hard-beam machine must be used to reduce to the elastic energy stored in the apparatus. The value of γ_{WOF} is calculated from the total energy (W) to propagate the energy and the area A as follows:

$$\gamma_{WOF} = \frac{W}{2A} \qquad \text{Eq. I-8}$$

Then, it was suggested to use this effective fracture energy to apply the Hasselman's theory by considering macroscopic energy rather than microscopic one [NAK-65, LAR-74]:

$$\begin{cases} R'''' = \dfrac{\gamma_{WOF} \cdot E}{\sigma_t^2} \\ R_{st} = \sqrt{\dfrac{\gamma_{WOF}}{\alpha^2 \cdot E}} \end{cases} \qquad \text{Eq. I-9}$$

Another technique, namely the notched-beam test [BRO-66] (Figure I-5b), can provide the energy required to initiate propagation of a crack, γ_{NBT}, from the measurement of the critical stress intensity factor K_{Ic} as follows:

$$K_{Ic} = \sqrt{2 \cdot \gamma_{NBT} \cdot E} \qquad \text{Eq. I-10}$$

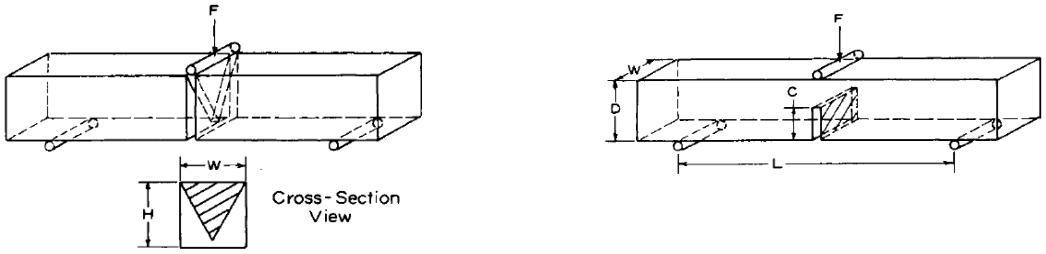

-a-

-b-

Figure I-5: Typical specimen configurations for (a) work-of-fracture method and (b) notched-beam method (area of fracture crosshatched) [NAK-65]

As a remark, the strength of a refractory is described better by γ_{NBT} than γ_{WOF} ($\sigma_t \propto \sqrt{\gamma_{NBT} \cdot E/l_0}$) [LAR-74]. Therefore, it comes:

$$R'''' = \frac{\gamma_{WOF} \cdot E}{\sigma_t^2} \propto \frac{\gamma_{WOF} \cdot E}{\gamma_{NBT} \cdot E/l_0} = \frac{\gamma_{WOF}}{\gamma_{NBT}} \cdot l_0 \propto \frac{\gamma_{WOF}}{\gamma_{NBT}} \qquad \text{Eq. I-11}$$

That is why some authors suggest to estimate the thermal shock resistance of heterogeneous materials from this $\gamma_{WOF}/\gamma_{NBT}$ ratio [AKS-03a]. As a remark, the energetic approach was initially developed for brittle materials, using the surface fracture energy in the Griffith's sense. The material behaviour of many refractory materials being, in fact, non purely brittle, there is still open discussions about the best physical parameters which should be taken into account into formulas describing the thermal shock resistance.

In fact, some researchers began to realise, during the 70's and 80's, the necessity of conducting measurements on individual or single cracks to investigate the fracture of refractories. Sakai and Bradt reviewed [SAK-93] different fracture mechanics test specimens in relation with the work-of-fracture measurement. Then, it appeared that usual laboratory-scale specimens for work-of-fracture tests could not allow to get a representative sampling of refractories due to their coarse aggregate microstructure. Indeed, with these too small samples, the different phenomena occurring around the crack (see next paragraph II.3), could not reach a steady-state configuration. In order to come up with this problem, the wedge splitting test [TSC-86, TSC-91] was promoted by researchers in Leoben, Austria, because it offered the possibility of having larger specimen and having a stable crack propagation [HAR-95, BUC-99]. This test, detailed in Chapter II, presents some similarities with the J-integral compliance method, first introduced by Rice [RIC-68], for metals, and, then, applied by Homeny et al. [HOM-80] to the fracture of refractories. Indeed, in a different way, they both allow to determine fracture energy which is crucial for a better understanding of the fracture process of refractories, and its relationship to microstructural design.

II.3. Crack growth resistance in refractories and associated R-curve phenomenon

According to the theory of linear elastic fracture mechanics, a crack propagates when the stress intensity factor K, at the crack tip, reaches the critical constant value K_c of the material. However, some materials, like refractories, exhibit an increasing crack propagation resistance (or toughness) when the crack length increases [HUE-77], also called R-curve or K^R-curve behaviour. This behaviour is due to energy-absorbing phenomena occurring around the cracks and demanding more energy to make the crack front advance [BRA-81, MAR-87, RIT-88, STE-83]. Two main regions around the crack can be distinguished, namely the process zone in front of the advancing crack and the following wake region, behind (Figure I-6). In the frontal process zone, microcracking and multiple crack branching are usually observed. Otherwise, the phenomena occurring behind the crack front, in the following wake region, such as aggregate bridging (Figure I-6), are known to be the most crucial ones for the increasing crack resistance [STE-83] of refractories. The size of these regions is rather large for most of refractory materials, that is why laboratory-scale specimens have to be large enough.

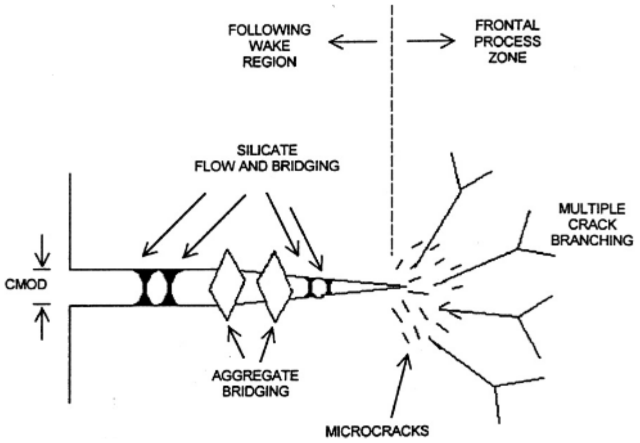

Figure I-6: Schematic of the crack process zone for refractory materials [BRA-04]

The R-curve measurement consists in determining the energy consumed to resist to crack propagation as a function of the crack extension Δa. By definition, crack propagation occurs when:

$$G \geq R \qquad \text{Eq. I-12}$$

where G and R are the total energy released per unit surface of propagation (or strain energy release rate) and the resistance to crack propagation (or energy dissipation rate), respectively.

An unstable crack propagation is guaranteed when an excess of driving force remains as the crack extends, which leads to the additional condition:

$$\frac{\partial G}{\partial a} \geq \frac{\partial R}{\partial a} \qquad \text{Eq. I-13}$$

Two different kinds of R-curves can be distinguished, namely flat R-curves (R is constant with crack length) corresponding to brittle linear elastic materials and rising R-curves often observed for large grained ceramics, like refractories [ADA-81]. For rising R-curves, different cases can be considered according to the stress level, namely no extent of the crack, extent with stable crack propagation, and extent with unstable crack propagation [WAC-09]. For example, if the stress level causes G>R, the value of R increases by increasing the crack size until that G=R and, then, stops if $\partial G/\partial a < \partial R/\partial a$. This stable propagation corresponds to the so-called quasi-static crack propagation proposed by Hasselman several decades before knowing the existence of R-curves. As a remark, the R-curve is not an intrinsic parameter of the material [STE-83, MAR-88, ROS-86] since it depends on the sample volume, the depth and location of the crack initially introduced, the testing conditions and the evaluation technique.

Sakai and Bradt described [SAK-86] different methods to determine the complete R-curve of a material. Most of these techniques involve loading/unloading cycles during the test in order to distinguish the elastic and irreversible contributions. But, by applying total unloading steps, the microstructure of the material can be strongly affected [SAK-86, CLA-76] by frictional effects in the process wake, especially for coarse-grained refractories due to the formation of grain bridges [HAR-96]. Therefore, another graphical method was introduced [SAK-86] in order to determine the R-curve from the stable load-displacement curve obtained by a wedge splitting test without unloading step. This method was used by Harmuth et al. [HAR-96, TAN-95].

II.4. Importance of the aggregates character and arrangement on thermal shock damage resistance

One can easily understand that the ability of delaying the unstable crack propagation (when $\partial G/\partial a < \partial R/\partial a$ the crack stops) in a refractory material will increase its thermal shock damage resistance. In fact, the non-linearity of the mechanical behaviour, the rise of the R-curve and the thermal shock damage resistance are very linked together [GOG-78, GOG-93, SWA-83, SWA-90, LUT-91a, LUT-91b, SAK-92, SCH-93a]. Therefore, it seems quite clear that the main route of improving the thermal shock damage resistance of refractories is to optimise the non-linearity of their mechanical behaviour, as well as the rise of their R-curve behaviour, through suitable microstructure designs [SCH-94, LUT-91a]. Indeed, the choice of the aggregates (geometry, size distribution, strength, thermal expansion coefficient, etc.), their spatial distribution and bonding to the matrix will be crucial to promote dissipation mechanisms, especially in the following wake region.

Although fracture toughness and R-curve behaviour were rather widely investigated for technical ceramics, such as magnesia-partially-stabilized zirconia (Mg-PSZ) ceramics [SWA-83, MAR-88], alumina materials [STE-83], or Al_2O_3-ZrO_2 composites [SWA-90, LUT-91c], not so many studies dealing with refractory materials [HAR-96, HAR-97, HEN-97, HEN-99] have, up to now, been carried out, despite the high toughness potential of such materials compared to common ceramics. Thus, microstructure design optimization in relation with thermal shock damage resistance is still a promising area of refractory research. Numerical studies, by finite element method for example, could bring, in the future, very interesting results in addition to experimental ones.

III. Numerical approaches

Although the analytical approaches allow to get valuable information on the required material properties and to compare materials, the thermal shock resistance analyses are limited to simple cases and, most of the time, cannot predict well the resistance of a real part (complex geometry, heterogeneities, etc.). Therefore, numerous numerical methods have been developed over the last several decades without stopping proposing new areas of investigation, for both macromechanics and micromechanics problems. These methods aim at solving continuum mechanics problems involving constitutive equations and conservation law. Among them, the most famous are the finite difference method (FDM), the finite element method (FEM), the boundary element method (BEM) and the discrete element method (DEM). Nevertheless, the most used method remains the FEM since it is applicable for most of the continuum mechanics problems. This is the numerical method considered here.

III.1. Macromechanics-based simulations of homogeneous parts of a structure

At the macroscopic scale, industrial refractory structures, or some parts of them, are considered as homogeneous. Thus, thermal shocks (see paragraph I) can appear as a combination of an imposed temperature gradient in the material and external mechanical conditions preventing from free deformation in some regions, which can lead to an early failure. The use of the FEM has allowed to investigate, over the past twenty years, the evolution of the thermal stresses and cracks, occurring in these installations, in order to predict the refractory lining behaviour under thermo-mechanical loading. The first numerical works were based on linear elastic mechanics [RUB-99, BRA-87, KNA-90, SCH-93b, KEI-89] and, then, quasi-brittleness of refractories was considered by using fictitious crack models [AND-02, AND-03, GIL-97]. Since coarse-grained refractories develop a diffuse damage before localization of a macrocrack [SIM-00, AKS-04a], continuum damage mechanics [CHA-88] was expected to be suitable to model the material behaviour [BOU-01, BOU-04]. Many other authors worked on numerical modelling of the thermo-mechanical behaviour of refractories based on damage mechanics [PRO-01, GAS-01, NEN-02, LUC-03, GRU-04, HEA-05, LIA-05, BLO-05, DAM-08].

III.2. Micromechanics-based simulations of heterogeneous materials

Another aspect of thermal stresses, already presented in paragraph I, concerns the microstructure scale at which the temperature field can be considered as uniform and the stresses are mainly caused by either thermal expansion mismatch between phases, or anisotropic thermal expansion. The numerical investigation in this area requires to use micromechanics-based simulations, which is preferred in the present thesis since it aims at studying the structure/property relationships in refractory materials. Reviews of interest can be found in [PIN-09, MIS-01].

Micromechanics-based simulations of heterogeneous materials, like refractories, are presently developed to increase the understanding of the material behaviour. They could allow to identify and choose the appropriate constituents, with appropriate spatial arrangements and mechanical properties of each constituent, providing the desired effective (macro) thermo-mechanical properties. Ideally [PIN-07], these simulations should allow complex microstructures and possible elastic/inelastic material properties for constituents.

Many works were carried out and many micromechanical concepts were developed during the last years to build constitutive models allowing to determine the macroscopic properties from microscopic ones. Concerning the case of spatially uniform microstructure, two main approaches can be distinguished, namely the deterministic ones, and the probabilistic [OST-08] ones. The deterministic approaches can be separated into three categories [PIN-09], namely “microstructural detail-free approaches”, “approaches based on statistically homogeneous microstructures” and “approaches based on periodic microstructures” (see Chapter II). The two last ones allow to consider the actual microstructure details from unit cell models.

Some examples of micromechanical studies dealing with refractory materials can be found in [SCH-02, GAS-05, SAN-07, JOL-08].

III.3. Brief review of damage models

Two main categories of crack modelling exist in literature, namely discrete crack models and continuum damage models.

Discrete crack models allow to represent explicitly a crack within the material and to simulate its growth thank to propagation criteria. Mainly used for crack modelling at the structure scale, they are also used with unit cell micromechanics approaches. Among this category of models, the node-release-technique (NRT) [BRU-85] allows to propagate a crack by mesh opening from fracture mechanics criteria (critical stress, critical crack opening displacement, critical crack length versus time, etc.). This method has been used in [JOL-08, QI-09] (“Debond” tool in Abaqus software package) to simulate the microcrack opening and closure of two-phase (glass/alumina) refractory materials, with thermal expansion mismatch, and get their Young's modulus evolution versus temperature. This method exhibits some disadvantages: it is only available in 2D, the crack path has to be known in advance, and a pre-crack has to be introduced. Similarly to the NRT, the cohesive zone models (CZM) [TVE-97] allow to simulate crack propagation along a known crack surface, but either in 2D or in 3D. The crack path is represented by a thin material layer having its own behaviour (traction-separation law). Indeed, the crack initiates when the cohesive traction stress exceeds a critical value. This method was used in [MAT-08] to model the interfacial debonding occurring during cooling of glass/alumina composites with thermal expansion mismatch. Otherwise, other discrete crack methods exist. A promising one is the extended Finite Element Method (XFEM) [MOE-99], or Generalised Finite Element Method (GFEM), which extends the classical FEM approach by "enriching the solution space for solutions to differential equations with discontinuous functions". Therefore, cracks can propagate inside elements without having to prescribe crack path in advance, and use remeshing.

Continuum damage models are of significant interest for the present work. They represent, with more or less sophisticated features, microcracking effect by decreasing the bulk stiffness of the element thank to a behaviour law. Many variants of such models, like smeared crack models [WEI-95, WEI-98], have been developed over the past several decades, and are still being developed. Some of them are based on elastic-brittle damage (irreversible strains are negligible) and others on plastic-brittle (permanent unrecoverable strains after unloading, in addition to the modification of the elastic properties). Furthermore, some of the last versions of such models consider anisotropy of damage [GOD-05, SAN-07], which allows to simulate the decrease of stiffness only in the stressed direction (more realistic). Nevertheless, problems of mesh dependency are usually observed with all of these damage models because of damage localization in one element. Indeed, the dissipated energy tends towards zero when the element size is decreased infinitely, which is not physically acceptable. Regularisation methods are introduced to fix these localisation problems.

III.4. Advantage of regularisation methods

Several approaches of regularisation method have been developed. All of them aim at introducing an internal length characteristic of the microstructure scale. Indeed, they take the neighbourhood into account in order to prevent the numerical solution from spatial discretization (mesh) dependency.

The most famous methods for continuum damage models are the following ones:

- Methods with fracture energy conservation [BAZ-76, BAZ-83, PIE-81] which allow to ensure that the energy dissipated during the fracture of the material remains the same whatever the fineness of the mesh.
- Methods with regularised variables, dealing with nodal variables gradients, for which regularisation is introduced by spatial averaging, either from integral form [PIJ-87, BAZ-02] or from spatial gradient terms (see below for the strain gradient method).
- Methods with gradients of internal variables (like damage variables) [LOR-05]

As a remark, other alternative methods are also used to come up with this mesh dependency problem. They consist in adding a discontinuous kinematics in the finite element discretization. The cohesive zone models are the most used ones but the main disadvantage is that the crack path has to be known. Moreover, methods with possible discontinuities inside the elements (ex: XFEM) have been developed for several years but this approach does not aim at describing precisely the behaviour inside the localisation bands since the main goal is to represent their effects at the structure scale.

In the present thesis, a method with regularised variables, namely a strain gradient method, has been used. The origin of this method comes from [AIF-84]. The method was, then, developed by Peerlings [PEE-96, PEE-01] who proposed to regularise a scalar variable which is the Von Mises strain obtained from the total strain field. Then, Godard [GOD-05] proposed to regularise each component of the total strain tensor in order to get a better flexibility with the damage models used (ex: anisotropic damage models). The Godard’s method, available in Code Aster, has been used in the present work. Otherwise, for this kind of approach, the localisation band representing the structure damage often enlarges too much. In fact, this could come from the constant value of the characteristic length [GEE-98]. In the strain gradient method used in [GOD-05], the possible relaxation of the regularisation operator is implemented. As a remark, more recently, non-local modelling has also been discussed in [DAM-08, DAM-11] in relation with thermal shock damage in refractory materials.

IV. Conclusion

This first chapter aimed to establish the state of the art concerning thermal shock of refractory materials and the different approaches which have been developed for several decades to estimate and improve the thermal shock resistance.

After a reminder about the different possible origins of thermal stresses (mechanical constraints, thermal expansion mismatch or anisotropy, and thermal gradient), the analytical approaches of Kingery and Hasselman were briefly presented. The energetic approach of Hasselman, with its thermal shock resistance parameters R'''' and R_{st}, is very interesting to deal with refractory materials. Experimental techniques were, then, developed in order to study the non-linear mechanical behaviour (deviation from linear elastic behaviour) of refractories, especially to measure fracture energies on notched samples, like the work-of-fracture test, the notched-beam test, the J-integral compliance method and the wedge splitting test. The fracture energies delivered by these methods (ex: γ_{WOF}) can be incorporated in the traditional formula of R'''' and R_{st}, instead of the surface fracture energy (γ_s). The origin of the crack growth resistance in refractories is usually attributed to energy-absorbing phenomena occurring around the crack, such as microcracking and multiple crack branching in the frontal process zone and aggregate bridging in the following wake region. This crack growth resistance is associated to a rising R-curve. During the last two decades, the close relationship between aggregates, non-linear mechanical behaviour, rising R-curve and thermal shock resistance was investigated but still has to be investigated further in order to be able to optimize the thermal shock resistance by controlling the microstructure design of refractories. Numerical simulations seem to be an interesting route to reach this goal.

The numerical (FEM) approaches have the advantage to be able to deal with much more complex cases (complex geometry, heterogeneities...) than the analytical approaches can do, for the prediction of thermal shock resistance of a real part. According to the considered problem, either macromechanics or micromechanics-based simulations can be realised. In the present thesis, since the relationships between microstructure and macro-mechanical properties are investigated, micromechanics-based FEM simulations will be performed. More precisely, an approach based on periodic microstructures was chosen for the study and is detailed in Chapter II. Otherwise, in order to well depict the damage which can occur during a cooling step and during a subsequent mechanical test in tension, a brief review of damage models was proposed. Continuum damage models, with possible anisotropy, and combined with a regularisation method, seem to be interesting for the study. The damage model used here is detailed in Chapter V.

Chapter II. Materials and methods

I. Introduction

I.1. Brief history on industrial magnesia-spinel materials

Nowadays, refractories containing spinel $MgO\text{-}Al_20_3$ (MA) are called magnesia-spinel products (MSp). This kind of refractories was first patented in 1932 in Austria [AUS-32]. The manufacturing of this material was carried out by addition of alumina within the magnesia mixes followed by a firing stage. The formation of MA spinel was, then, obtained by reaction between alumina and periclase. Magnesia chromite refractories have been preferred for many years for their low cost and easiness in manufacturing. But, in the 80's, the toxicity of the Cr(VI) produced from Cr_2O_3 under alkaline conditions [BRA-85] leaded to strict European Union regulations which forced industrial companies to prefer alternative refractory materials without Cr_2O_3. Magnesite and dolomite refractories were good ones for a significant number of reasons but the thermal shock resistance was not high enough. Then, it appeared that the thermal shock resistance of a magnesia brick is increased by the addition of 9-30% of magnesium aluminate spinel ($MgAl_2O_4$) [COO-82, DAL-88]. In fact, the first evaluation of magnesia-spinel materials was carried out 50 years ago [EUS-60] but the efforts to use them as alternative materials started in the 90's approximately. An additional advantage of these refractories was their longer life (ex: 1.5-2 times for rotary cement kilns) compared to magnesia-chrome materials [TOK-91]. Then, industrial and academic studies were realised in order to understand better why the thermal shock resistance is increased and to find a way to improve it. This improved resistance was first attributed to increased toughness [SOA-91, TAB-92]. Then, it became clear [AKS-02, AKS-03b] that the thermal expansion mismatch between magnesia ($13\text{-}15 \cdot 10^{-6}\ K^{-1}$) and spinel ($8\text{-}9 \cdot 10^{-6}\ K^{-1}$), entailing microcracking [SOA-91] around the spinel inclusions, was one of the main causes of the thermal shock resistance.

The studies carried out by Aksel et al. are very interesting but concerned fine-grained magnesia-spinel composites [AKS-02, AKS-03a, AKS-03b, AKS-04a, AKS-04b, AKS-04c]. In the present thesis, coarse-grained magnesia-spinel composites, close to industrial ones, are investigated.

I.2. Industrial context of the studied materials

Magnesia-spinel materials are mainly used in the cement industry. Different MSp products exist, depending on the stoichiometry of the spinel aggregates. Indeed, theoretically, the stoichiometric MA Spinel contains 71.8 wt.% of alumina (Al_2O_3) and 28.2 wt.% of magnesia (MgO) with a melting temperature equal to 2135°C, as shown in Figure II-1. This is the only chemical compound in the MgO-Al_20_3 binary system but in fact, due to the large domain of existence of MA spinel, three different types of spinel can be manufactured, namely almost stoichiometric, sub-stoichiometric (magnesia rich) and super-stoichiometric (alumina rich) ones. Sub-stoichiometric spinel is often used in MSp products for cement rotary kilns. In this thesis, magnesia-spinel materials with sub-stoichiometric spinel, close to industrial ones (Figure II-2), were elaborated.

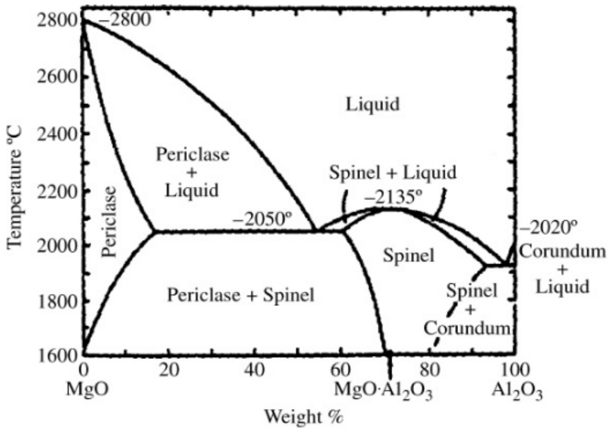

Figure II-1: Phase diagram of the MgO-Al_2O_3 system

-a- -b- -c-

Figure II-2: Industrial magnesia-spinel refractories – Cement rotary kiln (a) – Installation of these materials (b) – Microstructure (c)

I.3. Particular interest of studying model materials

As a rule, the specific thermomechanical evolutions (non-linearity, hysteresis...) of most refractory materials are due to their highly heterogeneous microstructure (number of phases, size and shape of the aggregates) with prefabricated microcracks. This is the case for the industrial magnesia-spinel materials presented in Figure II-2. In order to understand better this behaviour, the chosen approach consists in studying materials with only two constituents (magnesia and spinel) with simplified granulometries. These two-phase materials are so-called "model" materials since they allow to identity and quantify the direct impact of microstructural parameters on the thermomechanical properties through characterisation and predicting tools.

These elaborated model magnesia-spinel materials are of main interest in this thesis since the thermal expansion mismatch between the two phases is responsible for the presence of microcracks within the magnesia matrix. Nevertheless, other kinds of model materials without any damage in their microstructure were also considered for a preliminary work (Chapter III). These glass/alumina and glass/pores composites were elaborated in a previous work [TES-03] at the GEMH laboratory.

II. Model materials: presentation and processing route

II.1. Non thermally-damaged materials: glass/alumina and glass/pores composites

Glass/alumina (G/A) composites (Figure II-3) are composed of a dense aluminosilicate glass matrix with randomly distributed mono-sized alumina balls that are approximately spherical, with a mean diameter of 500 µm. They exhibit simple isotropic microstructures. The different stages of the processing are described in details in [TES-07]. The quite good agreement in terms of thermal expansion (Table II-1) for the two phases prevents from both microcracking and debonding which can occur during the cooling process.

Glass/pores (G/P) composites (Figure II-4) contain isolated spherical pores that were elaborated by the means of pore forming agent. The procedure consisted in mixing a fine glass powder - the same as the one for the G/A composites - with organic additives [TES-07] and perfectly spherical PMMA balls supplied by Degussa®. The pyrolytic degradation of PMMA particles during the debinding step leaded to the formation of isolated spherical pores randomly distributed in the glass sample. The maximum value of porosity is 42%. Above this value, the microstructure of porous glass materials exhibited an interconnected pores structure.

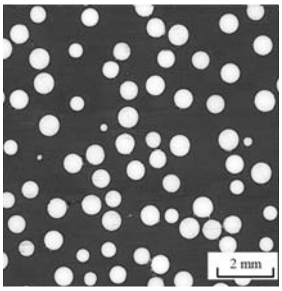

Figure II-3: Microstructure of a glass/alumina composite with $28_{v.}$% of alumina balls

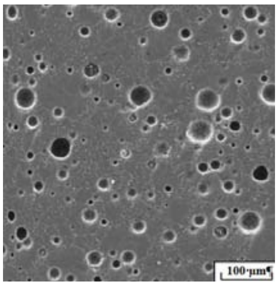

Figure II-4: Microstructure of a glass/pore composite with a porosity of $18_{v.}$%

Type of constituent	Dense glass	Alumina balls
Young's modulus E (GPa)	78	340
Poisson's ratio ν	0.21	0.24
Thermal expansion coefficient (K^{-1})	$6.5\cdot10^{-6}$	$7.6\cdot10^{-6}$

Table II-1: Thermoelastic properties at room temperature of the single constituents of G/A and G/P composites

II.2. Thermally-damaged materials: magnesia-spinel composites

II.2.1. Single constituents

Concerning the raw materials used in this study, industrial magnesia (with low iron content) and sub-stoichiometric (excess of magnesia) spinel aggregates, from fines (<0.1 mm) up to aggregates of 1-3 mm (for spinel) or 3-5 mm (for magnesia), have been used for the elaboration of single constituents samples (and two-phase materials). The bulk density and porosity of these magnesia and spinel aggregates (1-3 mm), as well as the true density of the magnesia and spinel powders (grain size < 40µm), are presented in the columns 2, 3 and 4 of Table II-2. The different granulometry categories, used for the bricks elaboration, are given in the first column of Table II-3.

Nature	**Powder (<40µm)**	**Aggregates (1-3mm)**		**Porous disc samples**	**Bricks ***		
	True density ($g.cm^{-3}$)	Bulk density ($g.cm^{-3}$)	Closed porosity (%)	Studied porosity range (%)	Bulk density ($g.cm^{-3}$)	Total porosity (%)	Thermal expansion coefficient (200-400°C) (K^{-1})
Magnesia	3.61	3.51	2.9%	17-32%	2.98	17.5%	**$13.3\cdot10^{-6}$**
Spinel	3.66	3.41	6.8%	8-19%	2.99	18.21%	**$8.9\cdot10^{-6}$**

* The magnesia brick is the reference brick for the composite materials

Table II-2: Properties of the magnesia and spinel used as matrix and inclusions, respectively, in magnesia-spinel composites

Concerning the processing routes, two different types of magnesia or spinel samples were elaborated, namely disc samples of small size with variable porosity and bricks of large size allowing to extract samples for mechanical characterisation.

- The disc samples with diameter of 50 mm were fabricated by uniaxial pressing of fine powders of either magnesia or spinel. Porosity was here mainly introduced by changing the applied pressure, from 60 MPa to 7 MPa, but also by lowering the firing temperature (1300°C instead of 1600°C). The obtained porosity was ranged between 17 and 32 v.%, for magnesia samples, and between 8 and 19 v.% for spinel samples (see Table II-2). Since the idea was here to cover the potential porosity of the magnesia matrix within the composite materials, no pore forming agent has been used additionally. These samples were elaborated to get accurate relations between Young's modulus and porosity. Moreover, the knowledge of the Young's modulus evolution versus porosity of magnesia also allows to estimate the actual Young's modulus of the magnesia matrix of each composite. These homogeneous polycrystalline materials are not thermally damaged since there is no anisotropic thermal expansion within the grains (cubic structures).
- The bricks were obtained, with semi-industrial means, according to the pressure cycle shown in Figure II-5a and the thermal cycle shown in Figure II-5b. The average dimensions are approximately 230mm·114mm·75mm. Information concerning these bricks, such as density, porosity and thermal expansion coefficient, are given in Table II-2. These bricks were elaborated in order to be able to carry out macro-scale experiments, like ultrasonic techniques and mechanical tests. Moreover, the magnesia brick was, then, considered as a reference for the magnesia-spinel composites since their constitution were based on the same granulometry of magnesia grains.

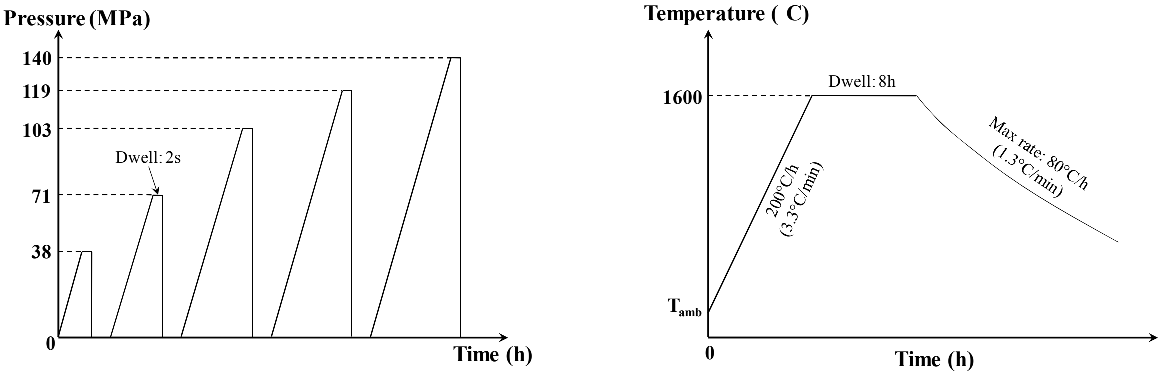

-a- -b-

Figure II-5: Pressure cycles of the green bricks (a) and thermal cycle to fire these bricks (b)

II.2.2. Magnesia-spinel composites with different spinel inclusions contents

The magnesia-spinel composites, composed of a magnesia matrix and spinel inclusions, were elaborated according to the same pressure and heating cycles (Figure II-5) used for the magnesia and spinel bricks. As for the glass/alumina composites, the aim here was to produce composites consisting of a monophase matrix (magnesia) with introduced inclusions (spinel), which is easier to model numerically. For this reason, contrary to the usual definition of the term “matrix” which designates fines, in the present thesis, the name “magnesia matrix” will represent the whole composite excepting the spinel inclusions (with coarse magnesia grains). The spinel content ranged between 5wt.% and 34wt.% for the main spinel grain size of 1-3 mm (Table II-3). A complementary composition of 15wt.%, with the 0-1 mm grain size, was also elaborated (Table II-3). The granulometric composition of these two-phase materials were deduced from the composition of the magnesia reference brick. Indeed, the spinel aggregates content replaced the same content of magnesia aggregates having the same size (1-3 mm or 0-1 mm).

Granulometry	**Magnesia reference brick**	**Magnesia-spinel composites**							
		Spinel 1-3 mm							**Spinel 0-1mm**
Spinel 1-3mm	-	**5%**	**10%**	**15%**	**20%**	**25%**	**30%**	**34%**	-
Spinel 0-1mm	-	-	-	-	-	-	-	-	**15%**
MgO 3-5mm	13.5%	13.5%	13.5%	13.5%	13.5%	13.5%	13.5%	13.5%	13.5%
MgO 1-3mm	34.0%	**29.0%**	**24.0%**	**19.0%**	**14.0%**	**9.0%**	**4.0%**	**0.0%**	34.0%
MgO 0-1mm	24.0%	24.0%	24.0%	24.0%	24.0%	24.0%	24.0%	24.0%	**9.0%**
MgO fines (<0.1mm)	28.5%	28.5%	28.5%	28.5%	28.5%	28.5%	28.5%	28.5%	28.5%

Table II-3: Granulometric compositions (wt.%) of the magnesia reference brick and of the magnesia-spinel composites

The properties of these magnesia-spinel materials are given in Table II-4, with those of the pure magnesia brick for reference. It appears that with increasing spinel content, the bulk density of the composites decreases and the open porosity increases. From the bulk densities of these composites and the bulk density of the spinel inclusions, assumed to be constant (3.41 $g.cm^{-3}$), the bulk densities of the matrices, as well as their total porosities, have been calculated and reported in Table II-4. Thus, the increase of spinel content induces an increase of the total porosity of the magnesia matrix. This can be due to the fact that densification, during sintering, is less well achieved when adding more and more inclusions in a homogeneous material. The presence of microcracks in such composites might also have an influence on these higher values of porosity.

		Magnesia reference brick	**Magnesia-spinel composites**							
			Spinel 1-3 mm							**Spinel 0-1mm**
Spinel content	wt.%	0%	5%	10%	15%	20%	25%	30%	34%	15%
	v.%	0%	4.3%	8.7%	13.0%	17.2%	21.5%	25.7%	29.2%	13.0%
Two-phase composite	Bulk density ($g.cm^{-3}$)	2.98 ◊	2.96	2.96	2.95	2.94	2.93	2.93	2.92	2.94
	Open porosity (%)	17.5% ◊	15.0%	15.1%	15.3%	15.4%	15.5%	15.6%	15.6%	15.8%
Magnesia matrix	Bulk density ($g.cm^{-3}$)	2.98 ◊	2.94 *	2.91 *	2.88 *	2.84 *	2.80 *	2.76 *	2.72 *	2.87 *
	Total porosity (%)	17.5% ◊	18.6% *	19.3% *	20.3% *	21.3% *	22.4% *	23.6% *	24.5% *	20.5% *

◊ These values of density/porosity correspond to those of the magnesia reference brick (without any spinel inclusion). Thus, values for the 0% inclusion – composite also correspond to those of the matrix.

* The properties of the matrices are here deduced from the properties of the composites taking into account spinel content and properties of spinel aggregates

Table II-4: Properties of the studied magnesia/spinel composites and the magnesia reference brick

An example for the microstructure of these magnesia-spinel materials is shown in Figure II-6. As expected, the thermal expansion mismatch (Table II-2) existing between the magnesia matrix ($13.3 \cdot 10^{-6}$ K^{-1}) and the spinel inclusions ($8.9 \cdot 10^{-6}$ K^{-1}) is responsible for the presence of radial microcracks around the spinel inclusions which appeared during the cooling stage of the process. For this reason, these composites are so-called thermally-damaged materials.

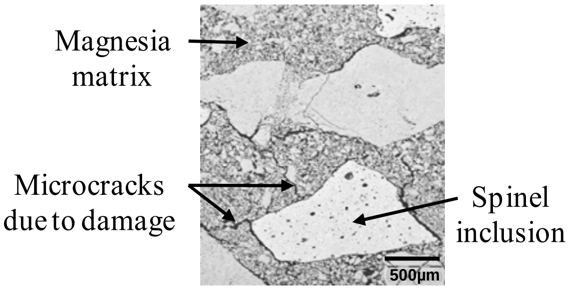

Figure II-6: Microstructure of a model magnesia-spinel composite

III. Experimental techniques

III.1. Nano-indentation test

The nano-indentation method allows to determine the local Young's modulus and hardness of the investigated grain. This technique consists in applying successive loading/unloading cycles on an indenter put in contact with the grain surface and to register the evolution of the applied load P versus depth d, as shown in Figure II-7a and Figure II-7b. Depth varies with the applied load (from 0.01 to 10N) but remains rather small (from the nanometer to several tens of micrometers).

The experimental device (Nanoindentation TM II) is composed of a diamond indenter in pyramid form with triangular base (Berkovich type [OLI-92]). The sample is first polished (~1µm) and, then, put on a support monitored in displacement (0.1µm). The conditions concerning the loading/unloading cycle are defined according to the nature of the investigated material [LAG-92, PAL-93].

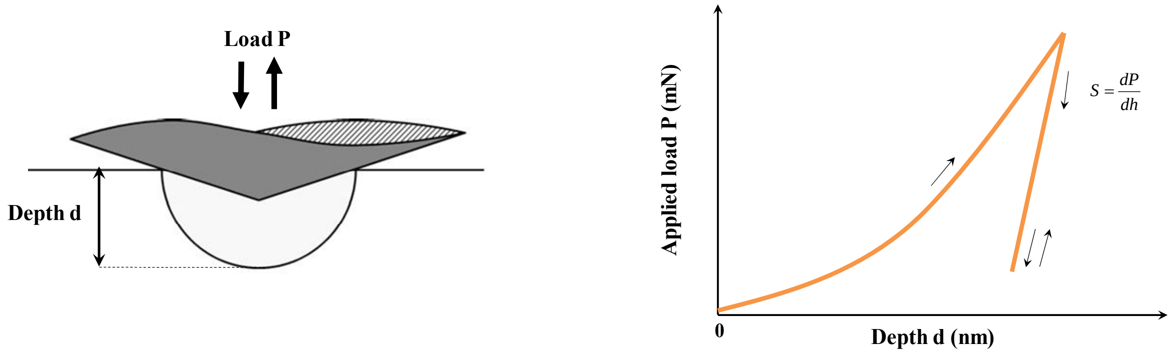

-a- -b-

Figure II-7: Scheme of the indenter penetrating the grain to characterise during a nano-indentation test (a) and typical obtained evolution of the applied load versus deepness (b)

The estimation of the Young's modulus is realised by determining the system rigidity S formed by the indenter/material couple and corresponding to the slope of the curve (dP/dh) during unloading (Figure II-7b). From this system rigidity S, the projected contact surface A, and a form factor ß depending on the tip used, a reduced Young's modulus (E_r), corresponding to the indenter/sample contact, can be calculated as follows:

$$S = \frac{dP}{dh} = \beta \cdot \frac{2}{\sqrt{\pi}} \sqrt{A} \cdot E_r \qquad \text{Eq. II-1}$$

Finally, the local Young's modulus of the grain, E_{exp}, is calculated by the following formula:

$$E_{\exp} = \frac{1-\nu^2}{\frac{1}{E_r} - \frac{1-\nu_i^{\,2}}{E_i}} \qquad \text{Eq. II-2}$$

where ν_i and E_i are the indenter Poisson's ratio and Young's modulus, and ν is the sample Poisson's ratio (assumed value).

III.2. Ultrasonic measurement in immersion mode

The ultrasonic measurement in immersion mode is another micro-scale technique for the determination of the elastic properties. The principle of this technique, shown in Figure II-8, is quite similar to usual contact ultrasonic measurements except that there is no contact (sample in water). Only longitudinal waves are used and higher frequencies are considered, typically 80MHz instead of 1-10MHz.

The sample with parallel surfaces, here a polished aggregate, is put on a support inside a tank full of water. A longitudinal wave is sent by an emitter-receiver transducer in the water and propagates into the aggregate. From the round trip time τ_L observed on a scope (Figure II-8), the Young's modulus E_{exp} is calculated according to the following formula:

$$E_{\exp} = \rho \cdot \left(\frac{2 \cdot t}{\tau_L} \right)^2 \cdot \frac{(1+\nu)\cdot(1-2\nu)}{(1-\nu)} \qquad \text{Eq. II-3}$$

where ρ, t and ν are the density, the thickness and the Poisson's ratio of the aggregate, respectively.

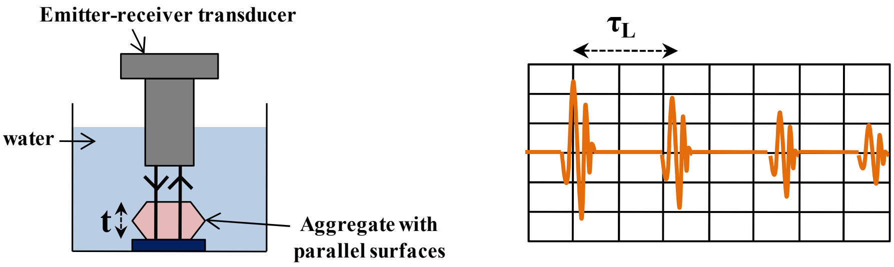

Figure II-8: Scheme of the ultrasonic measurement in immersion mode

III.3. Ultrasonic long bar mode method at high temperature

The ultrasonic long bar mode method at high temperature (Figure II-9a) allows to investigate the evolution of the Young's modulus in dependence of temperature for the studied material (Figure II-9b). The principle of this low frequency method in "long bar" mode is described elsewhere [GAU-85, HUG-92, CUT-93, CUT-94]. An ultrasonic wave is emitted by a magnetostrictive transducer linked to an alumina wave guide. This tension-compression ultrasonic wave is transmitted to the sample located in a furnace through the wave guide. From the round trip time τ, the length L and the bulk density ρ of the sample, the Young's modulus E can be calculated according to the following formula:

$$E = \rho \cdot V_L^2 = \rho \cdot \left(\frac{2 \cdot L}{\tau} \right)^2 \tag{Eq. II-4}$$

where V_L is the velocity of the longitudinal wave.

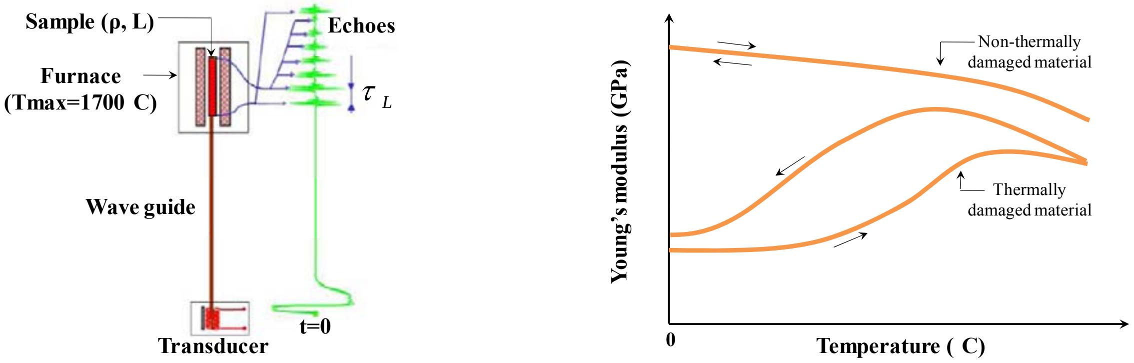

-a-

-b-

Figure II-9: Scheme of the ultrasonic long bar mode technique at high temperature [HUG-02] (a) and typical obtained evolutions of Young's modulus in dependence of temperature (b)

This method is often qualified as dynamic because of the low strain velocity imposed to the material. Moreover, it induces in the sample a low strain amplitude, around $3 \cdot 10^{-6}\%$ [BAH-09], compared to mechanical tests (tension, compression, flexural tests).

In order to achieve satisfactory propagation conditions in this particular ultrasonic mode (lateral sample dimensions < wavelength, [PAP-74]), the central frequency of the pulse and the specimens dimensions (parallelepipeds) are optimized according to the characteristics of the materials. Ultrasonic measurements of Young's modulus have been performed during thermal cycles made at a rate of 5°C/min for heating and cooling stages and a 1 h isothermal dwell at 1350°C.

III.4. High temperature acoustic emission

High temperature acoustic emission [CHO-08, BRI-08, PAT-09, PAT-10] is based on the record of acoustic waves induced by energy release phenomena occurring within the material (i.e: damage) during external solicitations (here thermal cycle). Formally speaking, it refers to the generation of transient elastic waves produced by a sudden redistribution of stress in the material. When a structure or a material is subjected to a stimulus (here change in temperature), localized sources trigger the release of energy, in the form of stress waves, which propagate to the surface and are recorded by sensors. Figure II-10 illustrates the experimental configuration.

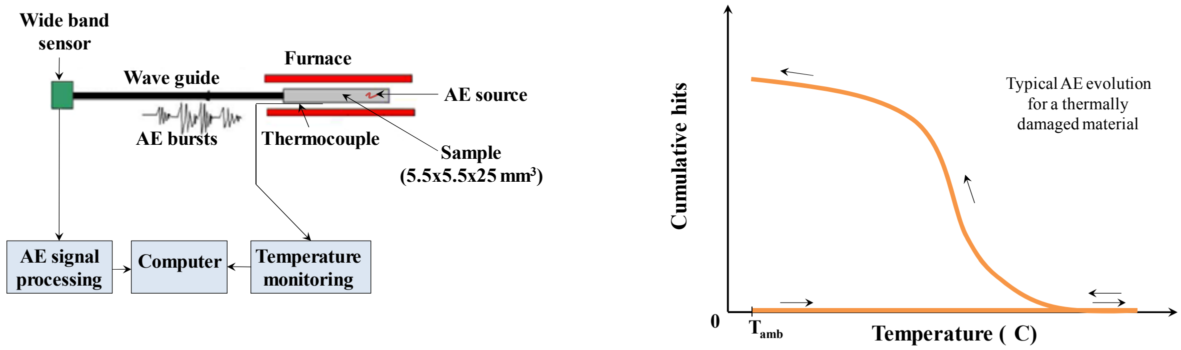

-a- -b-

Figure II-10: Scheme of the high temperature acoustic emission device (a) and typical obtained cumulative hits in dependence of temperature (b)

Acoustic Emission experiments have been performed in this study in order to obtain complementary information about the evolution of the microstructure in dependence of temperature, and especially on the chronology of in-situ phenomena (damage mechanism occurrence), by analysing the evolution of the cumulated number of hits (recorded signals) in dependence of temperature. The same heating – cooling cycles as those applied for ultrasonic measurements were used.

III.5. Tensile and wedge splitting tests for the characterisation of mechanical behaviour

Tensile tests are carried out with an INSTRON 8862 electromechanical device (Figure II-11a). This machine was adapted for high temperature measurements by M. Ghassemi Kakroudi [KAK-07, KAK-08, KAK-09]. The tests performed here, at room temperature, consist in applying a succession of loading/unloading cycles with a displacement increment at each cycle and with a constant displacement velocity (in this study around 1µm.s^{-1}).

Strain variations are measured by two capacitive extensometers equipped with silicon carbide rods and placed on two opposite sides on the sample. The gauge length of each extensometer is 25 mm. Otherwise, since the strain values of refractories are, as a rule, very low at rupture, the temperature of the extensometers is stabilised in order to avoid many deviations of measurement coming from temperature variation. Refractory samples are constituted of a cylindrical rod (20 mm in diameter) with two metallic parts glued at each end. The final geometry is obtained by machining simultaneously the middle zone of the sample (diameter: 16 mm) and the metallic parts in order to get a perfect co-axiality.

The stress-strain curve (Figure II-11b) obtained by a tensile test provides important information on the mechanical behaviour of the considered material, such as the initial slope, the non-linearity up to the maximum stress value, the post-peak behaviour and the fracture energy by integration of the whole curve. The different loading/unloading cycles allow to estimate the evolution of the Young's modulus during the test, and the evolution of the remaining strain value.

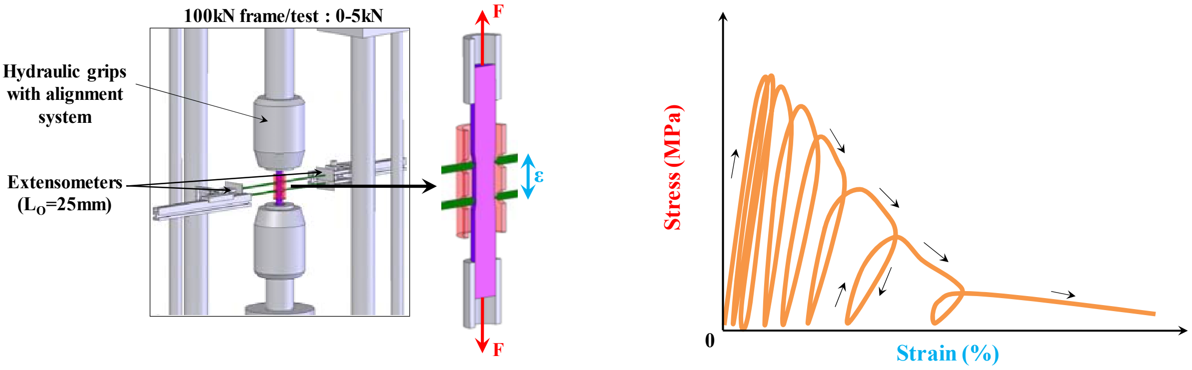

-a-

-b-

Figure II-11: Tensile test device (a) and typical obtained stress-strain curve for a thermally damaged material (b)

As other test methods like the notched beam test [SAK-93, CHI-85] and the compact tension method [SAK-93] , the wedge splitting test according to Tschegg [TSC-86, TSC-91] allows to specify the mechanical fracturing properties of refractory materials under uniaxial load (mode I loading). This test, patented in 1986, can also be applied on refractory materials to determine fracture mechanical properties (e.g. the specific fracture energy or the notch-tensile strength) at high temperature [TSC-94, HAR-97]. Biaxial tests are also possible [TSC-09].

The action of the wedge and the rather high rigidity of the equipment ensure a low energy accumulation in the specimen and the testing machine. Stable crack propagation can be achieved by displacement-controlled loading with a simple mechanical or hydraulic testing device. The test configuration is represented in Figure II-12a. The specific sample geometry is manufactured by machining. The vertical action of a metallic wedge, placed on the upper part of the sample and in contact with movable rolls, entails horizontal forces thank to load transmission pieces. Then, crack opening in mode I, with stable crack propagation, is obtained. Finally, the evolution of the horizontal force F_H versus the horizontal displacement δ is registered as shown in Figure II-12b.

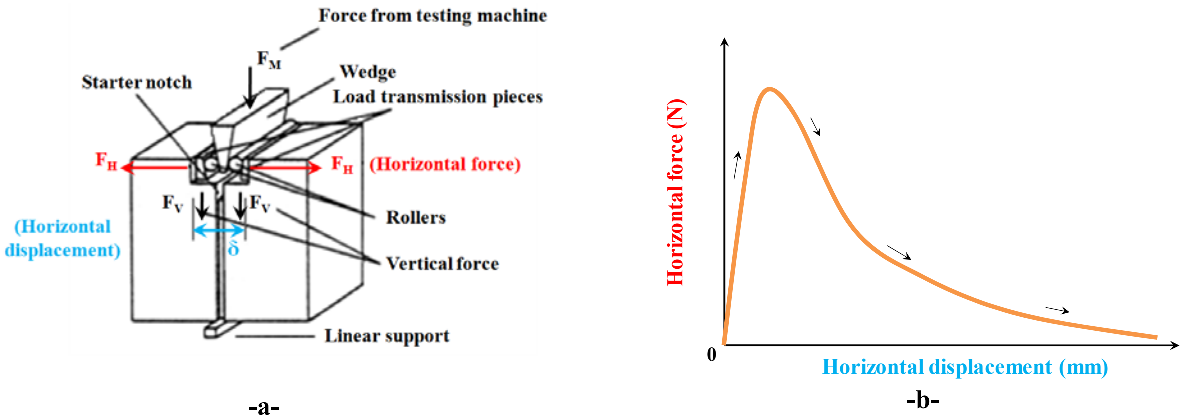

Figure II-12: Wedge splitting test device (a) and typical obtained force-displacement curve (b)

IV. Hashin and Shtrikman model as a reference for undamaged materials

For over a century, some models have been proposed in literature to estimate easily the thermoelastic properties of a two-phase composite from those of the two constituents. An interesting category of models is the category of bounds models providing the extrema behaviour of the composite. The simplest ones consider parallel and serial associations of the two phases. In elasticity, these bounds are the Voigt [VOI-1887] and Reuss [REU-29] bounds, corresponding to rules of mixtures for stiffness and compliance components, respectively.

The model proposed by Hashin and Shtrikman [HAS-62a, HAS-63a] is dedicated to isotropic materials composed of a matrix (m) and inclusions (i) with perfect matrix/inclusion interfaces. In the composite spheres assemblage (C.S.A.) constructed by Hashin [HAS-62b], each composite sphere consists of a spherical particle that is surrounded by a concentric matrix shell. The volume fractions of particle and matrix material are the same in each sphere, but the spheres themselves can be of any size. An arbitrary volume is then filled out with composite spheres of diminishing size, and the CSA is approached as a limit of complete filling. In the case where the bulk modulus of the matrix, K_m, is lower than the one of the inclusion, K_i, and the shear modulus of the matrix, μ_m, is lower than the one of the inclusion, μ_i, (glass/alumina and magnesia/spinel composites), the lower and upper K^{HS} and μ^{HS} bounds are expressed by:

$$K^{HS^-} = K_m + \frac{v_i}{\frac{1}{K_i - K_m} + \frac{3 \cdot v_m}{3 \cdot K_m + 4 \cdot \mu_m}} \quad \text{and} \quad \mu^{HS^-} = \mu_m + \frac{v_i}{\frac{1}{\mu_i - \mu_m} + \frac{6 \cdot v_m \cdot (K_m + 2 \cdot \mu_m)}{5 \cdot \mu_m \cdot (3 \cdot K_m + 4 \cdot \mu_m)}} \qquad \text{Eq. II-5}$$

$$K^{HS^+} = K_i + \frac{v_m}{\frac{1}{K_m - K_i} + \frac{3\cdot v_i}{3\cdot K_i + 4\cdot\mu_i}} \quad \text{and} \quad \mu^{HS^+} = \mu_i + \frac{v_m}{\frac{1}{\mu_m - \mu_i} + \frac{6\cdot v_m\cdot(K_m + 2\cdot\mu_m)}{5\cdot\mu_i\cdot(3\cdot K_i + 4\cdot\mu_i)}} \qquad \text{Eq. II-6}$$

where v$_i$ and v$_m$ are the volume fractions of inclusions and matrix, respectively.

In the case where $K_m > K_i$ and $\mu_m > \mu_i$ (glass/pores composites), the lower and upper HS bounds are inversed. The theoretical undamaged elastic properties of the glass/alumina and magnesia/spinel composites, namely the Young's modulus E and the Poisson's ratio ν, can be estimated from the lower HS bounds K^{HS-} and μ^{HS-} as the stiffness of the inclusion is sensitively higher than the stiffness of the matrix and those of the glass materials with pores can be estimated from the higher HS bounds K^{HS+} and μ^{HS+} (the lower bounds are equal to 0) [JOL-07]. For thermally-damaged materials, like magnesia-spinel materials, the experimental Young’s modulus is expected to be lower than the theoretical value provided by this model. Therefore, a thermal damage parameter D_{th} can be obtained by calculating the gap (%) to this model.

Concerning the coefficient of thermal expansion α, the lower and upper bounds are the following ones [ROS-70]:

$$\alpha^{HS^-} = \alpha_i + (\alpha_m - \alpha_i)\cdot\frac{\frac{1}{K^{HS^-}} - \frac{1}{K_i}}{\frac{1}{K_m} - \frac{1}{K_i}} \qquad \text{Eq. II-7}$$

and

$$\alpha^{HS^+} = \alpha_i + (\alpha_m - \alpha_i)\cdot\frac{\frac{1}{K^{HS^+}} - \frac{1}{K_i}}{\frac{1}{K_m} - \frac{1}{K_i}} \qquad \text{Eq. II-8}$$

V. Numerical techniques

The Code Aster software package [AST] has been used in the present thesis. Code Aster is an Open Source software package for Civil and Structural Engineering finite element analysis and numerical simulation in structural mechanics originally developed as an in-house application by the company EDF. It was released as free software under the terms of the GNU General Public License, in October 2001. The main interests of using Code Aster is the huge number of available libraries, the significant documentation with examples, the constant development and update of new functionalities, and the compatibility with python language programs. Indeed, python scripts have been used to automate writing of mesh and command files.

V.1. Advantage of numerical homogenisation techniques

V.1.1. Overview of the existing techniques

Industrial structures, or some parts constituting them, are usually considered as homogeneous at the macroscopic scale even if they are, in reality, heterogeneous at the microscopic scale (Figure II-13). In order to understand the microstructure key points allowing to develop non-linear mechanical behaviour, the best way would be to make direct FEM simulations by meshing the whole structure at the scale of each grain. This is not really possible because the calculations would be too much time consuming. Indeed, although numerical models based on finite element method (FEM) or fast Fourier transformation method (FFT) are suitable means for investigating microstructure-property relationships, they need high calculation resources and high computational cost, in particular for non linear analyses [MAD-07, BIL-05]. A common solution is to consider only a Representative Volume Element (R.V.E.) of the structure and to estimate its thermo-elastic properties by using homogenisation techniques. These methods allow to determine the global elastic behaviour of the Real Heterogeneous Material (R.H.M.) which would exhibit an Equivalent Homogeneous Material (E.H.M.) as shown in Figure II-13. As already mentioned, the R.V.E. corresponds to a volume of the heterogeneous material which is large enough to get stable properties when increasing its size. Moreover, this R.V.E. size depends on the homogenisation technique used.

Different homogenisation methods exist. The two main methods are the following ones [BOR-01]:

- application of uniform stress (force imposed) on the boundaries of the R.V.E.
- application of uniform strain (displacement imposed) on the boundaries of the R.V.E.

As a rule, these two techniques do not deliver the same results but tend towards the same value when the R.V.E. size increases. Another homogenisation technique is periodic homogenisation which involves such conditions on the boundaries with additional periodic conditions [HUE-90, BOR-01, MIC-99, DRAG-07].

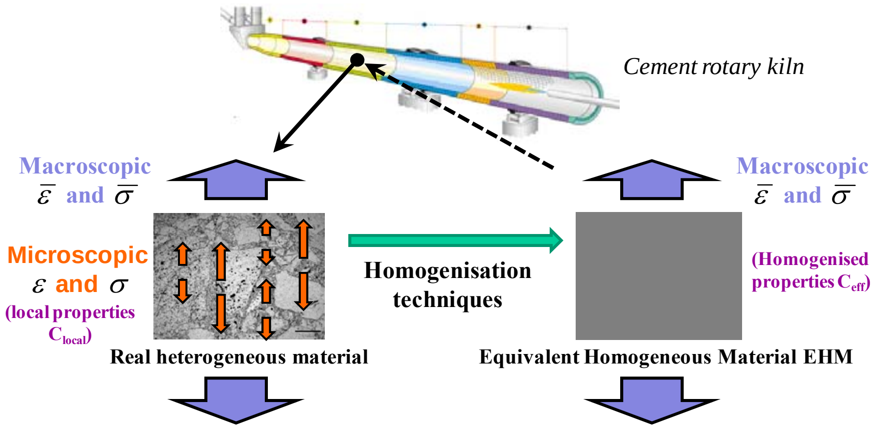

Figure II-13: Interest of using homogenisation techniques

V.1.2. Periodic homogenisation method

V.1.2.1. Periodic boundary conditions versus homogeneous displacement and homogeneous force boundary conditions

Numerical homogenisation of periodic heterogeneous media are widely used to derive the macroscopic behaviour of composites [NEM-93, MOU-98, YAN-04, BIL-05, ALZ-07]. When using FEM, the numerical analysis can be limited to a unit cell matching with the periodic representative pattern. The microstructure can then be obtained by translation in the three particular directions of periodic medium. The pattern can be a basic one or a more complex one. This method can also be used in the case of complex random microstructures [SUQ-83, SUQ-87, MOU-98]. In that case, the unit cell corresponds to the RVE. As a remark, some authors [PIN-09] prefer to distinguish the Repeating Unit Cell (RUC) concept, suited to periodic materials, from the RVE concept, suited to statistical homogeneous materials. Finally it must be emphasized that this approach is particularly advantageous to derive macroscopic behaviour when the local behaviour is non-linear.

In the present study, a numerical periodic homogenisation method [BOR-01, MIC-99] is used to estimate the thermo-elastic properties. This technique allows to define exact boundary conditions on the unit cell and then it allows a faster convergence to the homogenized properties than other numerical methods (Figure II-14) [BOR-01, KAN-03, DRAG-07]. Indeed, with traditional homogeneous displacement or force boundary conditions, the boundary deformations become independent of the applied boundary conditions type only when there is a sufficient number of inclusions in the volume whereas, with periodic boundary conditions, a single unit cell and a much bigger volume composed of this cell deform in the same way. For example, Figure II-15a and

Figure II-15b show simple simulated results of a tri-axial compression test on an asymmetric cell (inclusion not centred) without (homogeneous force instead) and with periodicity, respectively. An asymmetric cell is considered in order to be sure that periodicity is not caused by the symmetry of the cell. It appears that, without periodicity (Figure II-15a), the volume contour is much more deformed near the sides which the inclusion is closer to. Therefore, it seems obvious that the global deformation of such cell will be significantly different from a volume composed of an infinite number of this unit cell. Thus, the smallest representative volume element allowing to prevent from this deformation boundary effect will be necessarily rather high. In contrast, with periodicity (Figure II-15b), the deformation shape of the considered volume does not depend on the number of unit cells due to their perfect periodicity. Two other examples of simulation with periodicity are presented in Figure II-15c (shear test) and Figure II-15d (tensile test).

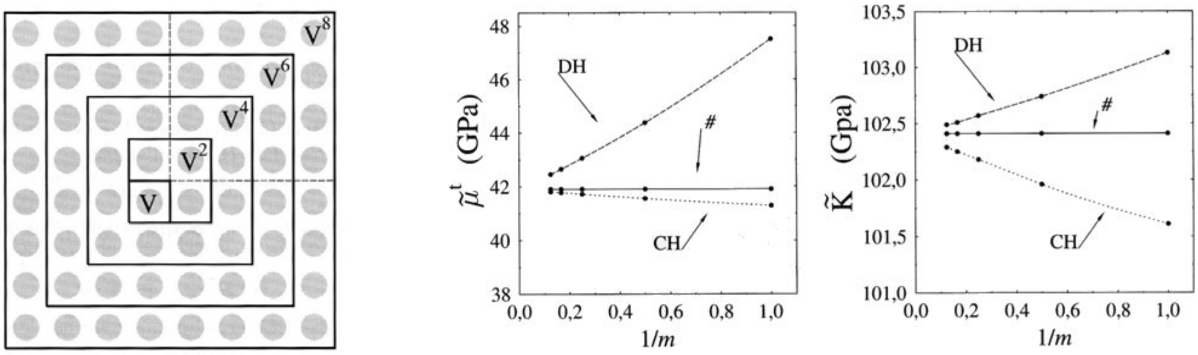

-a-

-b-

Figure II-14 [BOR-01]: Calculations with homogeneous displacement DH, homogeneous force CH and periodic # boundary conditions for a long fiber composite with square arrangement – (a) Element volumes considered for the study of the influence of boundary conditions (V^m contains $m \times m$ fibers) – (b) Evolutions of the shear $\tilde{\mu}^t$ and bulk $\tilde{K}$ moduli versus 1/m ratio

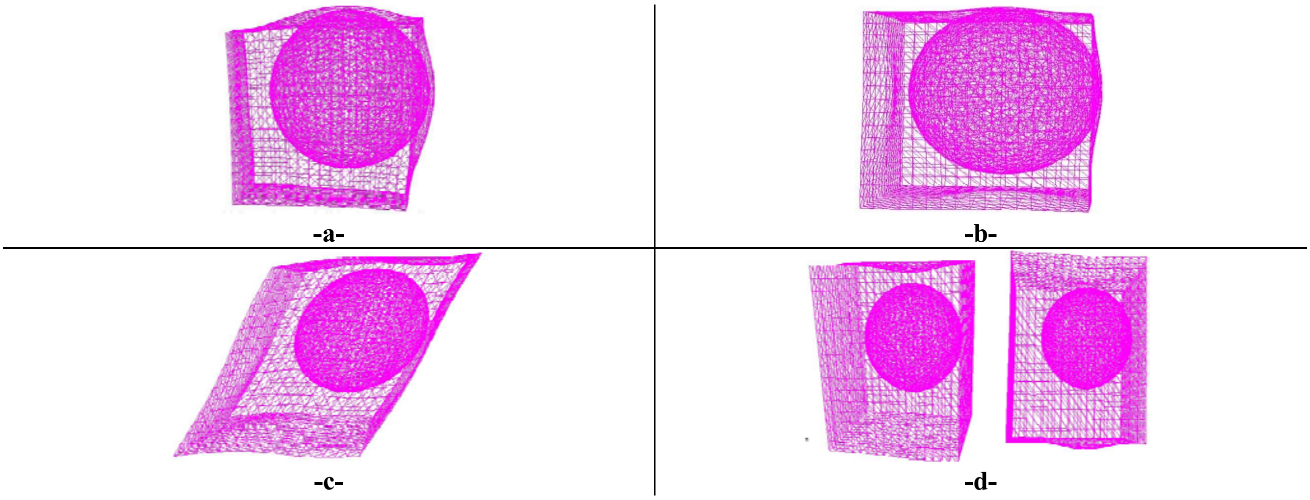

Figure II-15: Examples of simulated results (with Abaqus) obtained on an asymmetric volume cell (inclusion not centred) – Tri-axial compression test without periodicity, e.g. homogeneous force boundary conditions (a) and with periodicity (b) – Shear (c) and tensile (d) tests with periodicity

In fact, without periodic boundary condition, the deformation boundary effect on the contour of the volume is reverberated on the stress and strain fields. Figure II-16 allows to compare the maximum principal strain fields, without (homogeneous force) and with periodicity, after simulation of a bi-axial compression test on a 16 inclusion-cell. Visually, without periodic conditions (Figure II-16a), a boundary effect is observed near the boundaries. Therefore, it seems obvious that the number of repeated cells will have to be high enough in order to get stable elastic properties. This is not the case with periodicity (Figure II-16b) since the boundaries have not any influence on the internal strain field. Other examples of stress field periodicity, after simulation of a shear test (a) and a tensile test (b) with periodicity, are shown in Figure II-17 with an asymmetric cell.

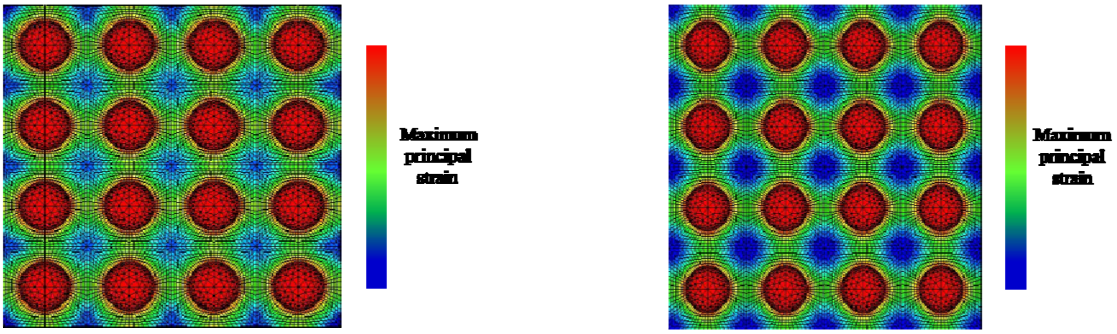

-a- -b-

Figure II-16: Visualisation of the maximum principal strain (Abaqus) obtained by simulation of a bi-axial compression test on a 16 inclusion-cell without (homogeneous force) (a) and with (b) periodic boundary conditions

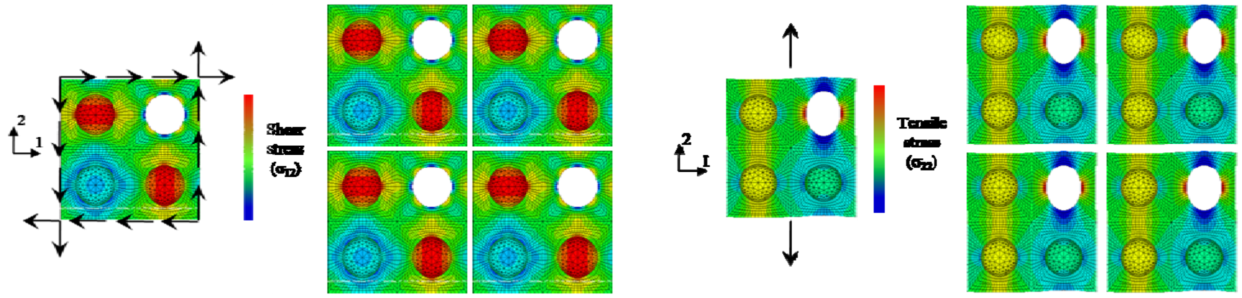

-a- -b-

Figure II-17: Examples of stress periodicity with an asymmetric cell (three inclusions and one hole) during a shear test (a) (σ_{12} stresses) and a tensile test (b) (σ_{22} stresses)

V.1.3. Numerical implementation

After having shown the relevance of using the periodic homogenisation method, the way of implementing such boundary conditions is detailed in this paragraph.

Here, to perform the computations of the effective elastic properties, a macroscopic uniform strain $\bar{\varepsilon}$ is imposed, which is done by imposing an affine displacement on the boundary of a periodic volume (with additional periodic conditions). Indeed, by applying this kinematic load, the $\bar{\varepsilon}$ strain tensor resulting in the homogenised medium is uniform (see Figure II-18). The stress field is also uniform in the equivalent homogenised medium with the effective stiffness tensor and is equal to $\bar{\sigma}$. At microscopic scale (Figure II-18), the presence of heterogeneities makes the local strain and stress fields fluctuate around the average values $\bar{\varepsilon}$ and $\bar{\sigma}$. Far away from the boundary surface, the displacement field $u(x)$ can be decomposed as follows [BOR-01]:

$$u(x) = \bar{\varepsilon} : x + u'(x) \qquad \text{Eq. II-9}$$

where $u'(x)$ is a periodic displacement field linked to the presence of heterogeneities. x, $u(x)$ and $u'(x)$ are vectors and $\bar{\varepsilon}$ is a matrix (3 x 3 in 3D). The sign ":" designs a matrix product.

By derivation of Eq. II-9 in the direction of x, one deduces the local strain field:

$$\varepsilon(u(x)) = \bar{\varepsilon} + \varepsilon'(u(x)) \qquad \text{Eq. II-10}$$

where $\varepsilon(u(x))$ is the local strain and $\varepsilon'(u(x))$ the periodic fluctuating strain with:

$$\langle \varepsilon(u(x)) \rangle = \frac{1}{|\Omega|}\int_{\Omega} \varepsilon dV = \bar{\varepsilon} \quad \text{and} \quad \langle \varepsilon'(u(x)) \rangle = \frac{1}{|\Omega|}\int_{\Omega} \varepsilon' dV = 0 \qquad \text{Eq. II-11}$$

In the previous expression, Ω is the domain of the unit cell and $|\Omega|$ its volume.

From Eq. II-9, the periodic fluctuation of the displacement reads:

$$u'(x) = u(x) - \bar{\varepsilon} : x \qquad \text{Eq. II-12}$$

or, in a Cartesian coordinate system:

$$u'_i = u_i - \sum \bar{\varepsilon}_{ij} x_j \qquad \text{Eq. II-13}$$

where x_j, u_i and u'_i are the components of the vectors x, $u(x)$ and $u'(x)$, respectively, and $\bar{\varepsilon}_{ij}$ are the components of the matrix $\bar{\varepsilon}$.

In practice, the implementation of this condition in a finite element code requires to mesh and analyse a unit cell V in which in one hand periodic conditions on u'_i are applied on the boundary of the cell (or ∂V), oriented by the normal n, and, in the other hand, the force vector $T(x,n) = \sigma \cdot n$ is anti-periodic on ∂V. Thus, in the finite elements discretisation of the unit cell, the displacements $u'_i(A)$ and $u'_i(B)$ of two opposite points A and B, belonging to ∂V and corresponding to each other by the translation of one period, are constant, so that:

$$u'_i(A) = u'_i(B) \qquad \text{Eq. II-14}$$

Combining Eq. II-13 with Eq. II-14 allows to write the following condition on ∂V, for each couple of opposite points:

$$u_i(B) - u_i(A) = \sum \bar{\varepsilon}_{ij}\left(x_j^B - x_j^A\right) \qquad \text{Eq. II-15}$$

It can be noticed that the mesh is of importance in order to apply these conditions: one possible solution is to make sure that the meshes of two opposite faces are identical (by projection for example), as shown in Figure II-19.

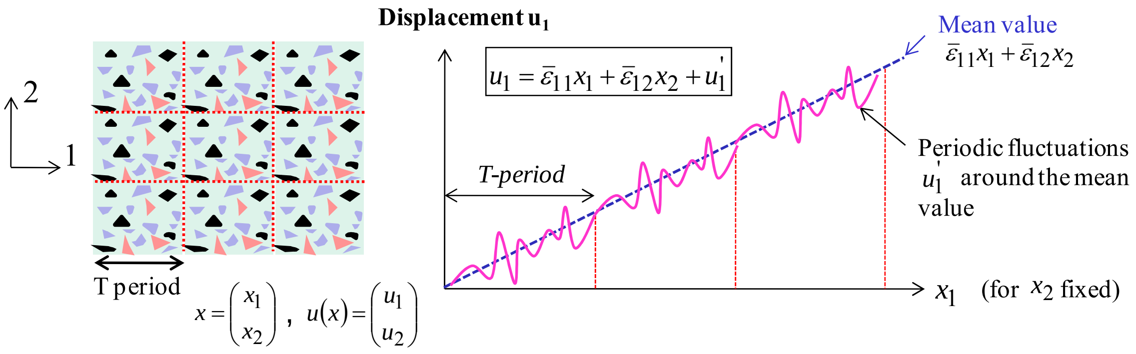

Figure II-18: Periodicity of the displacement field – decomposition into a mean part and a periodic fluctuating part

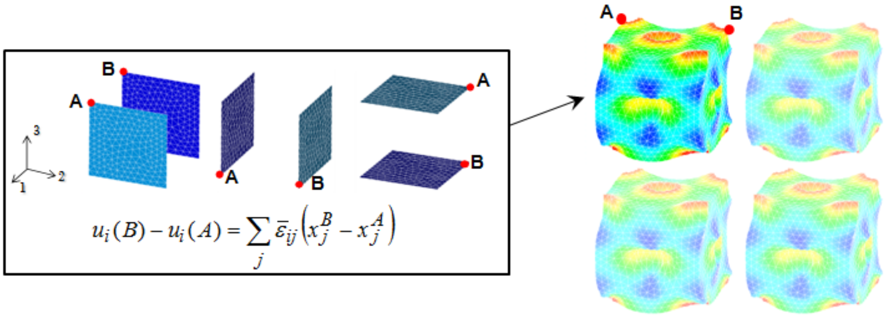

Figure II-19: Application of periodic conditions around the unit cell – relations between each couple of opposite nodes (same nodes distributions on the opposite faces)

After having presented how to implement periodic conditions around the cell, the means of determining the effective thermo-elastic properties of the homogenised material is of interest. In the present study (Chapters III and V), the macroscopic load which is imposed is always a macroscopic strain $\bar{\varepsilon}$. Then, the elastic properties can be determined by different techniques, namely either from the calculation of the effective elastic strain energy density $\tilde{w}$ or the calculation of the macroscopic stress tensor $\bar{\sigma}$ by volume average of the local stress. In Chapter III, for the determination of the effective stiffness tensor $\tilde{C}$, the energy method is preferred whereas, for the determination of the effective thermal expansion coefficient tensor, the stress method is used. In Chapter V, since the main objective is to get the macroscopic stress-strain behaviour in tension, the calculation of the macroscopic stress is used.

VI. Conclusion

This chapter has allowed to present the materials considered in the study, the experimental characterisation techniques and some numerical tools needed to simulate the thermomechanical behaviour of such materials.

In order to study the impact of microstructure effects (microcracks, debonds,...) on the non-linearity of the mechanical behaviour of refractory materials, magnesia-spinel materials were elaborated by simplification of industrial compositions. Indeed, these industrial materials, used for their high thermal shock resistance, present microcracks in their microstructure, due to CTE mismatch between the two main phases, and exhibit non-linear mechanical behaviour.

Local and macroscopic elastic properties of each constituent and the two-phase composites will be determined by different techniques either at room temperature (e.g. nano-indentation) or at high temperature (e.g. ultrasonic long bar mode method). Other high temperature techniques like acoustic emission and thermal expansion measurements will provide complementary information concerning the study of thermal damage occurrence during the cooling stage. Otherwise, the mechanical behaviour in tension will be investigated at room temperature by two different static techniques, namely a tensile test and a wedge splitting test.

The main objective of the present thesis was to implement in numerical models the microcracks occurrence during the cooling process and, then, to quantify the impact of this thermal damage on the non-linearity of the stress-strain law in tension. The interest of using a homogenisation technique combined with a rather small Representative Volume Element (R.V.E.) has been detailed. In the present work, a finite element periodic homogenisation method has been chosen and implemented for the next simulations. Before considering possible damage within the microstructure, a preliminary numerical work (Chapter III) has been dedicated to materials without any thermal damage.

Chapter III. Optimization of 3D RVE for anisotropy index reduction in modelling thermoelastic properties of two-phase composites using a periodic homogenisation method

I. Introduction

The magnesia-spinel materials are supposed to be isotropic. Therefore, the present chapter is dedicated to present the approach which has been used to find suitable quasi-isotropic Representative Volume Elements (R.V.E.) able to depict well the thermoelastic behaviour of two-phase materials. In this aim, the combination of the periodic homogenisation method with modelled cells as simple as possible has been considered. Moreover, since thermal damage is expected to occur during cooling in magnesia-spinel composites, other two-phase materials exhibiting no damage and linear elastic behaviour were preferred first: glass/alumina (G/A) and glass/pores (G/P) composites. Thus, this first step allowed to check the pertinence of the choice in terms of R.V.E. geometry, number of inclusions, spatial organisation of these inclusions, boundary conditions for application of periodic homogenisation method and loading conditions on the boundaries to obtain the desired homogenised properties. Later, in a second step (Chapter V), possible damage progression, which makes simulations much more complex, has been introduced in the magnesia matrix of these optimised RVE in order to handle the real case of magnesia-spinel materials including the occurrence of microcracks.

For the first step considered here, the investigated temperatures for this numerical study has been limited to the 20-500°C range. Indeed, for this temperature range, the isotropic properties of the single constituents, shown in Table III-1, can be assumed rather constant versus temperature.

	Dense glass	Alumina balls
Young's modulus E (GPa)	78	340
Poisson'ratio ν	0.21	0.24
Bulk modulus K (GPa)	44	218
Shear modulus μ (GPa)	32	137
Thermal expansion coefficient α (K^{-1})	$6.5 \cdot 10^{-6}$	$7.6 \cdot 10^{-6}$

Table III-1: Properties of the two single constituents used for calculations

II. Estimation of the effective stiffness and thermal expansion coefficient tensors

II.1. Effective stiffness tensor

The effective stiffness tensor $\tilde{C}$ of the equivalent homogeneous material is calculated by using an energy analysis. In practice, the components of the tensor are calculated by applying different macroscopic strain cases $\bar{\varepsilon}$ on the unit cell combined with the homogenisation conditions. The Hill's macro-homogeneity condition ensures that the macroscopic work density is equal to the spatial average of the microscopic work density [HIL-67]:

$$\langle \sigma(x) : \varepsilon(x) \rangle = \frac{1}{|\Omega|} \int_{\Omega} \left(\sigma(x) : \varepsilon(x) \right) dV = \bar{\sigma} : \bar{\varepsilon} \qquad \text{Eq. III-1}$$

where σ and $\bar{\sigma}$ are the local and macro stress tensors, respectively and ε and $\bar{\varepsilon}$ are the local and macro strain tensors. $\bar{\sigma} = \langle \sigma(x) \rangle$ is the average stress tensor.

For linear elasticity, the local strain energy density w has a quadratic form of the strain tensor ε and reads:

$$w = \frac{1}{2} \varepsilon(u(x)) : C(x) : \varepsilon(u(x)) \qquad \text{Eq. III-2}$$

where C is the local stiffness tensor, so that the local stress tensor can be written:

$$\sigma = \frac{\partial w}{\partial \varepsilon}(x, \varepsilon) \qquad \text{Eq. III-3}$$

Since the free energy density is additive, the effective macroscopic strain energy density $\tilde{w}$ reads:

$$\tilde{w}(\bar{\varepsilon}) = \langle w(\varepsilon(u)) \rangle \qquad \text{Eq. III-4}$$

Thus, the macroscopic stress-strain relation is expressed according to:

$$\frac{\partial \widetilde{w}}{\partial \bar{\varepsilon}}(\bar{\varepsilon}) = \bar{\sigma} \qquad \text{Eq. III-5}$$

Details concerning the variational formulation for the numerical resolution of the problem by the finite element method are given in [BOR-01]. In practice, the strain energy density $\widetilde{w}$ is obtained by finite element calculations for different imposed $\bar{\varepsilon}$ strain states allowing to activate only some components of the stiffness tensor $\widetilde{C}$. Finally, $\widetilde{C}$ can be identified, with its 21 possible elastic constants in the most general case.

II.2. Effective thermal expansion coefficient tensor

The effective CTE tensor is identified by a thermoelastic simulation by applying a uniform increase in temperature ΔT. It depends on the effective stiffness tensor calculated in a previous step. The local Hooke's law reads:

$$\sigma(x) = C(x) : \varepsilon^{e}(u(x)) = C(x) : \left(\varepsilon(u(x)) - \varepsilon^{th}(\Delta T, x)\right) \qquad \text{Eq. III-6}$$

where ε^{e}, ε and ε^{th} are the local elastic, total and thermal strain tensors, respectively and $\Delta T = T - T_0$.

From the previous remarks, it can be deduced that:

$$\bar{\sigma} = \left\langle C(x) : \left(\varepsilon(u(x)) - \varepsilon^{th}(x)\right)\right\rangle = \widetilde{C} : \left(\bar{\varepsilon} - \widetilde{\varepsilon}^{th}\right) \qquad \text{Eq. III-7}$$

where $\bar{\varepsilon}$ and $\widetilde{\varepsilon}^{th}$ are the macroscopic imposed total strain and the macroscopic effective thermal strain tensors, respectively.

One suitable way to estimate the effective thermal strain tensor is to impose $\bar{\varepsilon} = (0)$ and, at the same time, a constant thermal field in the unit cell. Thus, the expression of this thermal strain tensor is the following one:

$$\widetilde{\varepsilon}^{th} = -\widetilde{S} : \bar{\sigma} \qquad \text{Eq. III-8}$$

where $\widetilde{S}$ is the compliance tensor deduced from a previous elastic simulation ($\widetilde{S} = \widetilde{C}^{-1}$) and $\bar{\sigma}$ is the mean stress tensor induced in the volume caused by the applied thermal field under the restriction of $\bar{\varepsilon} = (0)$.

Finally, from Eq. III-8, the effective thermal expansion coefficient tensor $\tilde{\alpha}$ is identified as follows:

$$\tilde{\alpha} = -\frac{\tilde{C}^{-1} : \bar{\sigma}}{\Delta T} \qquad \text{with } \Delta T = T - T_0 \qquad \text{Eq. III-9}$$

where ΔT, imposed on the whole cell, is uniform.

It can be pointed out that, thanks to the applied periodic conditions, a border of the unit cell is not fixed and can deform but the opposite one deforms in the same way, and the relative displacement difference (ΔL) between two opposite points remains equal to zero.

III. Choice of appropriate Representative Volume Elements (R.V.E.) combined with periodic conditions on the boundaries

Specific periodic microstructures have been studied so that the number of inclusions in the representative periodic pattern might be as low as possible to limit the computational time and, at the same time, that the effective thermoelastic behaviour can be as less anisotropic as possible to respect the statistical isotropy of the elaborated materials. Moreover, in order to be able to apply periodic conditions, unit cells were chosen so that the assembly of them might reconstitute all the 3D-space. Three unit cells representative of three specific inclusions or pores arrangements have been examined. The first unit cell corresponds to a spherical inclusion embedded within a cube of matrix phase. This pattern, when periodic displacement conditions are applied to the cell boundary, allows to analyse the behaviour of microstructure having periodic cubic arrangement (C.), as shown in Figure III-1. The symmetry of this arrangement, in term of stiffness, is not isotropic but cubic with 6 equivalent directions. Also the maximum volumic fraction of inclusions is limited to 52.4%. Two other types of periodic arrangements of inclusions or pores (see Figure III-1) were studied:

- the face-centred cubic (F.C.C.) arrangement,
- the hexagonal close-packed (H.C.P.) arrangement.

Both have 12 equivalent directions and the maximum volumic fraction of inclusions is much higher (74%).

The structure of the stiffness tensor is well known for these three arrangements. To obtain the values of its components, Finite Element Periodic Homogenisation (FEPH) was used, the simulations being realised with the Code Aster software [AST].

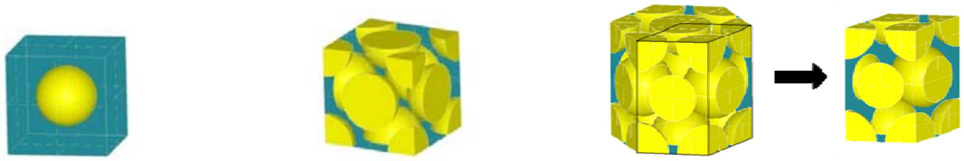

C. arrangement F.C.C. arrangement H.C.P. arrangement

Figure III-1: Modelled cells corresponding to cubic (C.), face-centred cubic (F.C.C.) and hexagonal close-packed (H.C.P.) arrangements

IV. Deviation from isotropy of the simulated effective tensors

IV.1. Calculation of stiffness anisotropy indices

The symmetry of effective stiffness tensors is cubic (Figure III-2) for C. and F.C.C. arrangements and transversely isotropic (Figure III-3) for H.C.P. arrangements [HEA-61]. The cubic and transversely isotropic stiffness tensors are characterized by 3 and 5 elastic constants, respectively, whereas the isotropic one (Figure III-4) is only defined by 2 constants. Therefore, after having calculated all the elastic constants and checked the relations between them, one important task is to estimate the gap to isotropy of such arrangements, in terms of stiffness, before comparing the simulated results, obtained with FEPH, to the experimental results obtained with isotropic materials having random microstructures.

$$\begin{pmatrix} C_{11} & C_{12} & C_{12} & 0 & 0 & 0 \\ C_{12} & C_{11} & C_{12} & 0 & 0 & 0 \\ C_{12} & C_{12} & C_{11} & 0 & 0 & 0 \\ 0 & 0 & 0 & C_{44} & 0 & 0 \\ 0 & 0 & 0 & 0 & C_{44} & 0 \\ 0 & 0 & 0 & 0 & 0 & C_{44} \end{pmatrix}$$

Figure III-2: Theoretical stiffness tensor with cubic symmetry

$$\begin{pmatrix} C_{11} & C_{12} & C_{13} & 0 & 0 & 0 \\ C_{12} & C_{22} & C_{12} & 0 & 0 & 0 \\ C_{13} & C_{12} & C_{11} & 0 & 0 & 0 \\ 0 & 0 & 0 & C_{44} & 0 & 0 \\ 0 & 0 & 0 & 0 & \frac{1}{2}\cdot\left(C_{11}-C_{13}\right) & 0 \\ 0 & 0 & 0 & 0 & 0 & C_{44} \end{pmatrix}$$

Figure III-3: Theoretical stiffness tensor with transversely isotropy (case of isotropy in the 1-3 plane)

$$\begin{pmatrix} C_{11} & C_{12} & C_{12} & 0 & 0 & 0 \\ C_{12} & C_{11} & C_{12} & 0 & 0 & 0 \\ C_{12} & C_{12} & C_{11} & 0 & 0 & 0 \\ 0 & 0 & 0 & \frac{1}{2}(C_{11}-C_{12}) & 0 & 0 \\ 0 & 0 & 0 & 0 & \frac{1}{2}(C_{11}-C_{12}) & 0 \\ 0 & 0 & 0 & 0 & 0 & \frac{1}{2}(C_{11}-C_{12}) \end{pmatrix}$$

Figure III-4: Theoretical stiffness tensor of an isotropic structure

The example of Alumina/glass (G/A) composite with 50 vol.% content of inclusions is considered, first, to compare qualitatively the simulated effective stiffness tensor to the theoretical isotropic one proposed by the Hashin and Shtrikman (HS) model. The effective stiffness tensors of the equivalent isotropic material obtained from the bulk and shear modulus bounds of this model is presented in Figure III-5. The effective stiffness tensors obtained by FEPH with the three types of arrangements are shown in Figure III-6. As it could be expected, the symmetry of the tensors obtained with C. and F.C.C. arrangements is cubic and the constant values for the F.C.C. arrangement are much closer to the isotropic case (HS^- lower bound) than those for the C. arrangement. Moreover, in the case of the H.C.P. arrangement, the constants associated to the isotropic plane (1-3 plane) are not exactly the same, as expected, as those in the third direction (2-direction) but quite close since the maximum difference is around 1 GPa.

$$\begin{pmatrix} 169.5 & 46.9 & 46.9 & 0 & 0 & 0 \\ 46.9 & 169.5 & 46.9 & 0 & 0 & 0 \\ 46.9 & 46.9 & 169.5 & 0 & 0 & 0 \\ 0 & 0 & 0 & 61.3 & 0 & 0 \\ 0 & 0 & 0 & 0 & 61.3 & 0 \\ 0 & 0 & 0 & 0 & 0 & 61.3 \end{pmatrix}$$

-a-

$$\begin{pmatrix} 203.9 & 58.6 & 58.6 & 0 & 0 & 0 \\ 58.6 & 203.9 & 58.6 & 0 & 0 & 0 \\ 58.6 & 58.6 & 203.9 & 0 & 0 & 0 \\ 0 & 0 & 0 & 72.6 & 0 & 0 \\ 0 & 0 & 0 & 0 & 72.6 & 0 \\ 0 & 0 & 0 & 0 & 0 & 72.6 \end{pmatrix}$$

-b-

Figure III-5: Effective stiffness tensor of the equivalent isotropic material obtained from the Hashin and Shtrikman lower (a) and upper (b) bounds (alumina grain volume fraction of 50%)

$$\begin{pmatrix} 182.5 & 45.3 & 45.3 & 0 & 0 & 0 \\ 45.3 & 182.5 & 45.3 & 0 & 0 & 0 \\ 45.3 & 45.3 & 182.5 & 0 & 0 & 0 \\ 0 & 0 & 0 & 60.9 & 0 & 0 \\ 0 & 0 & 0 & 0 & 60.9 & 0 \\ 0 & 0 & 0 & 0 & 0 & 60.9 \end{pmatrix}$$

-a-

$$\begin{pmatrix} 169.3 & 47.7 & 47.7 & 0 & 0 & 0 \\ 47.7 & 169.3 & 47.7 & 0 & 0 & 0 \\ 47.7 & 47.7 & 169.3 & 0 & 0 & 0 \\ 0 & 0 & 0 & 63.5 & 0 & 0 \\ 0 & 0 & 0 & 0 & 63.5 & 0 \\ 0 & 0 & 0 & 0 & 0 & 63.5 \end{pmatrix}$$

-b-

$$\begin{pmatrix} 171.7 & 45.9 & 46.8 & 0 & 0 & 0 \\ 45.9 & 172.6 & 45.9 & 0 & 0 & 0 \\ 46.8 & 45.9 & 171.7 & 0 & 0 & 0 \\ 0 & 0 & 0 & 61.6 & 0 & 0 \\ 0 & 0 & 0 & 0 & 62.4 & 0 \\ 0 & 0 & 0 & 0 & 0 & 61.6 \end{pmatrix}$$

-c-

Figure III-6: Effective stiffness tensors obtained by FEPH with C. (a), F.C.C. (b) and H.C.P. (c) arrangements (alumina inclusions volume content of 50%)

The evaluation of the stiffness anisotropy level of the three arrangements has been done, for different inclusions/pores contents, by using an anisotropy index. Zener [ZEN-48] introduced an index, A, to quantify the anisotropy of cubic crystals:

$$A = \frac{2 \cdot C_{44}}{C_{11} - C_{12}} \qquad \text{Eq. III-10}$$

where C_{11}, C_{12}, C_{44} are the three independent components of the stiffness tensor.

Some authors [SPO-95] prefer to quantify the anisotropy with the index $\Lambda = 1 - A$ instead of A. An equivalent Zener index was calculated for the H.C.P. arrangement. Indeed, since, for our materials, the constants associated to the isotropic plane (1-3 plane) are very close to those in the 2-direction, even at high content (50%) as shown in Figure III-6c, an equivalent Zener index A_{HC} is defined by averaging these constants according to:

$$A_{HC} = \frac{2 \cdot \left(C_{44} + C_{55}\right)}{\left(C_{11} + C_{22}\right) - \left(C_{12} + C_{13}\right)} \qquad \text{Eq. III-11}$$

The evolutions of index A or A_{HC} versus the volumic content of inclusions and the value of porosity for the different arrangements are shown in Figure III-7a and Figure III-7b, respectively. It appears, first, that the gap to isotropy is higher for higher alumina inclusions or pores content. This gap is much higher in G/P composites than in G/A composites because of the higher contrast of elastic properties (Young’s modulus) between the two phases in porous glass materials. Moreover, in both cases (inclusions/pores), the Zener index A obtained with a C. arrangement is rather far from the theoretical isotropic case (A=1) whereas the anisotropic indices obtained for F.C.C. and H.C.P. arrangements are quite close to the theoretical case. Therefore, the assumption of isotropic arrangements for the calculation of Young's modulus and Poisson's ratio seems to be more realistic in the case of F.C.C. and H.C.P. arrangements. In addition, the Zener anisotropy index appears to be the closest one in the case of the H.C.P. arrangement.

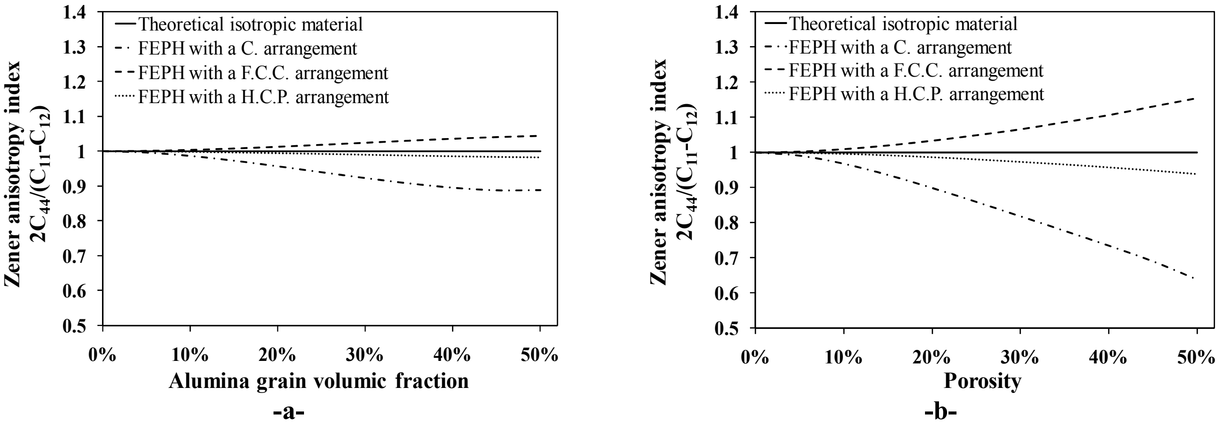

-a- -b-

Figure III-7: Determination of the arrangements anisotropy degree versus inclusions (a) or pores (b) content by calculation of the anisotropy index A and A_{HC} from the simulated results

IV.2. Calculation of a thermal expansion anisotropy index for the H.C.P. arrangement

The effective thermal expansion coefficient tensor was calculated for different inclusions contents for the three types of arrangements, with both alumina inclusions and pores. No thermal angular distortion was observed for these arrangements. This is not surprising, given that both phases are isotropic and, so, do not introduce a mechanical thermal angular distortion in the composites. Generally speaking, three symmetry classes of thermal expansion exist [BOR-10]: orthotropic, transversely isotropic and isotropic (cubic): it has been checked that the symmetry of thermal expansion of the C. and F.C.C. arrangements is isotropic and the one of the H.C.P. arrangement is transversely isotropic as shown in literature (see Figure III-8). Therefore, the gap to isotropy has only been estimated for the H.C.P. arrangement: similarly to the anistropic index A_{HC}, a thermal expansion anisotropy index, B_{HC} is defined as follows:

$$B_{HC} = \frac{\alpha_2}{\alpha_1} \qquad \text{Eq. III-12}$$

where α_1 is the thermal expansion coefficient in the 1 and 3-directions and α_2 is the thermal expansion coefficient in the 2-direction (Figure III-8b).

$$\begin{pmatrix} \alpha_1 \\ \alpha_1 \\ \alpha_1 \\ 0 \\ 0 \\ 0 \end{pmatrix} \qquad \begin{pmatrix} \alpha_1 \\ \alpha_2 \\ \alpha_1 \\ 0 \\ 0 \\ 0 \end{pmatrix}$$

-a- Isotropy **-b- Transversely isotropy**

Figure III-8: (a) Isotropic (C. and F.C.C. arrangements) thermal expansion coefficient tensor and (b) transversely isotropic (H.C.P. arrangement) thermal expansion coefficient tensor (isotropic in the 1-3 plane)

The evolutions of the anisotropy index B_{HC} versus the volume fraction of alumina inclusions and pores were estimated. It was shown that B_{HC} remains equal to 1 (theoretical isotropic case) for all the inclusions/pores contents. Consequently, there is no difference of thermal expansion between the different directions (ie: the 2-direction and the 1-3 directions). Therefore, the C., F.C.C. and H.C.P. arrangements can be considered as isotropic for the calculation of the effective CTE.

V. Comparison of the simulated thermoelastic properties with the measured ones and with Hashin and Shtrikman bounds

The thermoelastic properties, E, ν and α, obtained using the FEPH, for the different unit cell configurations (C., F.C.C. and H.C.P. arrangements) and type of heterogeneous materials (G/A and G/P materials) were calculated and compared with the experimental data [TES-03] and results from the HS bounds. These results are summarized in Figure III-9 to Figure III-11.

Figure III-9 compares Young's modulus versus the volume content of inclusions and pores. For both composites, the Young's modulus E^{HS^-} and E^{HS^+} deduced from the lower and upper HS bounds delimit these experimental data ($E_{\exp}$). As usually observed since the stiffness of the alumina inclusion is higher than those of matrix, $E_{\exp}^{G/A}$ is closer to E^{HS^-}. Conversely, as expected for the porous composite Young's modulus $E_{\exp}^{G/P}$ is closer to E^{HS^+}. The maximum deviation of the experimental results $E_{\exp}$ from the $E^{HS^\pm}$ is reported in Table III-2 for both composites. It appears that the maximum deviation is quite higher for G/P materials (10.3%) than the one for G/A materials (4.3%). This may be explained by the low values of Young's modulus for G/P materials compared to G/A materials. The prediction of Young's modulus E_{FEPH} obtained by FEPH for the three arrangements are also reported on Figure III-9. The deviation of E_{FEPH} from E^{HS^-} is higher for the C. arrangement, in G/A composites, than for the two other configurations (Table III-2). For the G/P composites, the H.C.P. arrangement of pores leads values of Young's modulus that are very close to the E^{HS^+} while the C. and F.C.C. arrangements exhibit higher deviations but still in the same range as the experimental results. Moreover, Figure III-9-b shows that the C. arrangement results remain above the HS upper bound and quite far from the other simulated and experimental results. Thus, in both cases of G/A and G/P materials, the F.C.C. and H.C.P. arrangements seem to be suitable numerical models, which is in agreement with the rather low anisotropy indices previously calculated.

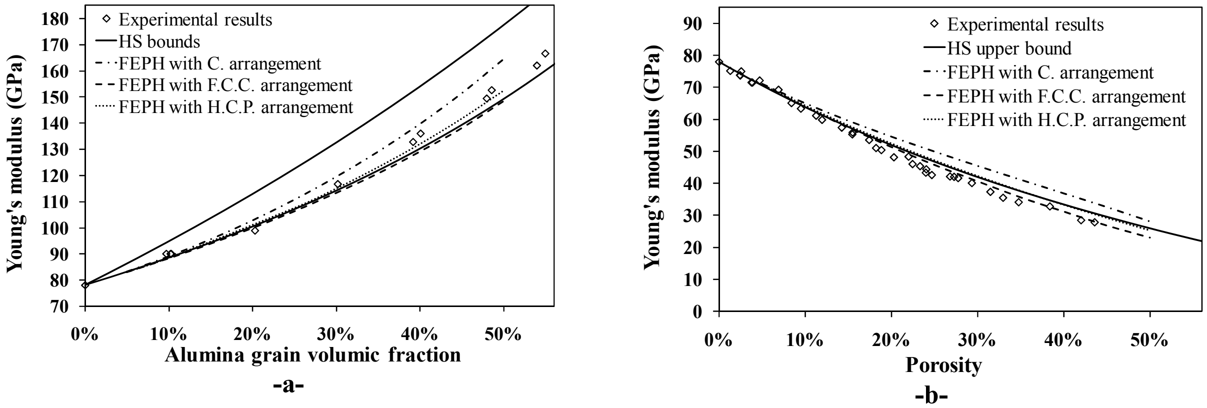

-a-

-b-

Figure III-9: Comparison between the simulated, analytical and experimental Young's moduli versus inclusions (a) or pores (b) content

	a) G/A composites		b) G/P composites	
	v.%	HS^- deviation (%)	v.%	HS^+ deviation (%)
C. arrangement	50	10.3	40	10.1
F.C.C. arrangement	35	0.9	50	11.2
H.C.P. arrangement	50	2.2	50	2.8
Experimental data	40.1	4.3	42	10.3

Table III-2: Maximum deviation of Young's modulus for the six periodic microstructures and the designed composites compared to Young's modulus calculated with the HS bounds

In the same way, Figure III-10 shows Poisson's ratio ($\nu_{\exp}$, ν_{FEPH} and $\nu^{HS^\pm}$) versus inclusions and pores content. First, it appears that experimental data $\nu_{\exp}$ are more dispersed in case of G/P composites than in case of G/A composites. This comes from the usual higher difficulty of ultrasonic measurements with porous materials. In addition, for G/A composites, $\nu_{\exp}$ is close to the $\nu^{HS^\pm}$ (see also Table III-3). This is an expected result because the Poisson's ratios of the two phases are close, so the variation of the effective Poisson's ratio depends only slightly on the concentration of inclusions.

When compared with the $\nu^{HS^\pm}$, ν_{FEPH} gives uneven results depending on the type of arrangement of inclusions in the periodic medium (Figure III-10 and Table III-3). For H.C.P.

arrangement of inclusions, ν_{FEPH} is very close to the $\nu^{HS^{\pm}}$ in both cases. For C. and F.C.C. arrangements, it must be pointed out that the effective Poisson's ratio diverge from the constant tendency of experimental results when the inclusion content is higher than approximately 5-10%. This may be related to the higher anisotropic effect observed with higher concentration of inclusions.

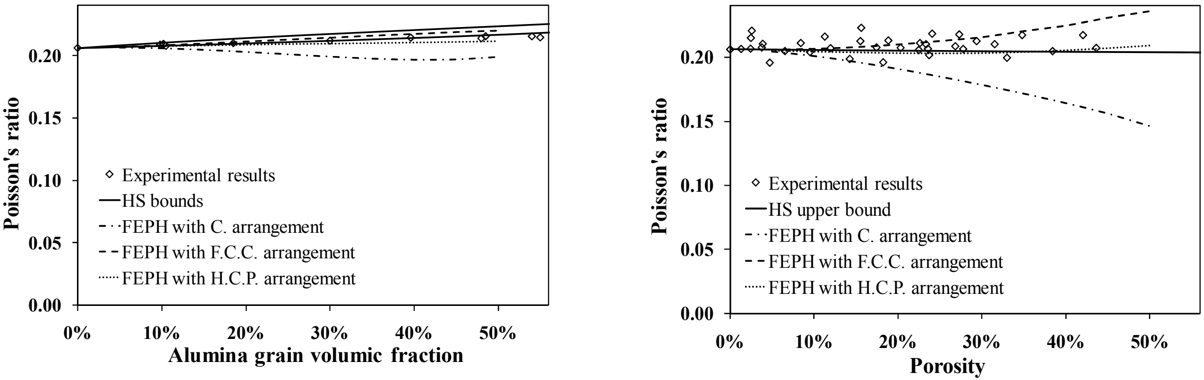

-a- -b-

Figure III-10: Comparison between the simulated, analytical and experimental Poisson's ratios versus inclusions (a) or pores (b) content

	G/A composites		G/P composites	
	v.%	HS$^-$ deviation (%)	v.%	HS$^+$ deviation (%)
C. arrangement	45	8.5	50	28.2
F.C.C. arrangement	45	1.5	50	15.9
H.C.P. arrangement	50	2.3	50	2.7
Experimental data	55	1.7	15.6	8.7

Table III-3: Maximum deviation of Poisson's ratio for the six periodic microstructures and the designed composites compared to Poisson's ratios calculated with the HS bounds

Finally, Figure III-11 shows the effective thermal expansion coefficient α versus inclusions content. The simulated results obtained with the three arrangements are close to the experimental data and to the HS bounds.

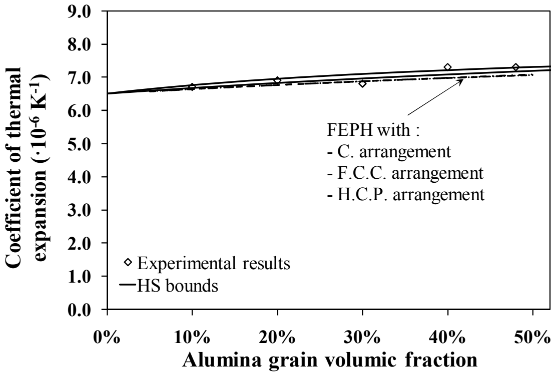

Figure III-11: Comparison between the simulated, analytical and experimental thermal expansion coefficient versus inclusions content

VI. Conclusion

This chapter dealt with a preliminary work realised on non-thermally damaged materials, namely glass/alumina (G/A) and glass/pores (G/P) composites. The main objective was to manage to use the periodic homogenisation method properly and to propose (and validate) quasi-isotropic periodic arrangements with a low number of inclusions. Indeed, a simple microstructure is needed to be able to introduce damage in a next step (Chapter V) requiring much more powerful calculation resources.

The approach developed has consisted in comparing the effective thermoelastic properties obtained by finite element periodic homogenisation with experimental data obtained on designed G/A and G/P composites and thermoelastic properties deduced from the HS bounds, assuming in all case that the heterogeneous medium is isotropic. Three arrangements of inclusions have been analysed, namely cubic (C.), face-centred cubic (F.C.C.) and hexagonal close-packed (H.C.P.) ones.

Anisotropy indices (A, A_{HC}, B_{HC}), calculated from the effective stiffness tensors and the effective thermal expansion coefficient tensors, have allowed to show the low degree of anisotropy especially for the F.C.C. and H.C.P. arrangements. Then, by assuming that the unit cells allow to depict R.V.E. with phases having isotropic thermoelastic behaviour, the effective Young’s modulus, Poisson’s ratio and coefficient of thermal expansion were calculated from the simulated results and compared to the experimental data and the properties deduced from the HS bounds.

The three periodic microstructures simulated with FEPH are able to give a quite accurate estimate of the macroscopic Young's modulus and CTE, sufficient compared to the scattering of the experimental data. The estimates of the effective Poisson's ratio are also accurate but, in the case of G/P composites, the results with C. and F.C.C arrangements diverge from both experimental data and the Poisson's ratio determined from the HS^+ bound. The quite good agreement between these results allows to validate the choice of F.C.C and H.C.P. microstructures combined with periodic conditions for the next study (Chapter V) on magnesia-spinel composites involving possible damage in the magnesia matrix.

Chapter IV. Characterisation of thermal damage induced by thermal expansion mismatch in magnesia-spinel materials and impact on the mechanical behaviour

I. Elastic properties at room temperature

I.1. Single constituents: porosity influence

In the previous chapter, the evolution of the elastic properties versus porosity were well described by the Hashin and Shrikman model, but in the case of pure magnesia and spinel materials, the experimental results are rather far from this model [GRA-10]. Therefore, another analytical model is needed.

The influence of porosity on the elastic properties is an old issue and many formulations have been proposed in literature for several decades [SPR-61, ISH-67, COB-56, MAC-50, NEM-99, CHR-00]. Pabst et al. have reviewed [PAB-06] some of these formulations and proposed a new one [PAB-04]. This model is expressed by:

$$E_r = \frac{E}{E_o} = \left(1 - \xi \cdot P + (P-1) \cdot P^2\right)\left(\frac{1 - P/P_c}{1 - P}\right) \qquad \text{Eq. IV-1}$$

where: E, E_0 and E_r are the Young modulus at the considered porosity, the dense Young modulus, and the relative Young modulus at the considered porosity; ξ is a parameter to be determined by fitting experimentally measured data (ξ = 2 with isometric pores); and P and P_c are the porosity and the percolation threshold, respectively. The percolation threshold is the critical porosity above which the pores are supposed to be connected and to form long-range connectivity in the material.

This analytical model has been used as reference for the study of the elastic properties of the single constituents versus porosity.

The experimental Young's modulus evolution versus porosity (different samples) of pure magnesia and pure spinel are shown in Figure IV-1a and Figure IV-1b, for a given porosity range. As expected, for both materials, the Young's modulus is significantly decreased by increasing the porosity. The analytical Pabst-Gregorova model is also represented in Figure IV-1a and Figure

IV-1b. The value of the geometrical parameter ξ was fixed to 2 for both magnesia and spinel by assuming the pores to be isometric. These dotted lines reported in these figures were obtained, by fitting the experimental results, for a percolation threshold P_c assumed to be equal to 45% and values of dense Young's modulus E_0 of magnesia and spinel assumed to be equal to 290 and 280 GPa, respectively. As a remark, the value of E_0 for magnesia, deduced here, is slightly lower than the value obtained by Chung [CHU-63] on magnesia monocrystals and polycrystals, namely 305 GPa, from the stiffness constants C_{ij}. According to Figure IV-1a and Figure IV-1b, the Pabst-Gregorova seems to describe well the Young's modulus evolution versus porosity of both magnesia and spinel. Indeed, the values obtained on single aggregates by nano-indentation (and local ultrasonic measurements in immersion) are very close to this model, as well as the values obtained on disc samples by ultrasonic means. Nevertheless, the experimental values obtained on bricks are quite lower than the model in dotted lines. Since the disc samples were obtained only from fines and the bricks from different granulometric categories (fines, 0-1 mm and 1-3 mm grains), these lower results could come from the more complex microstructures of bricks with, for example, imperfect bond between aggregates and fines.

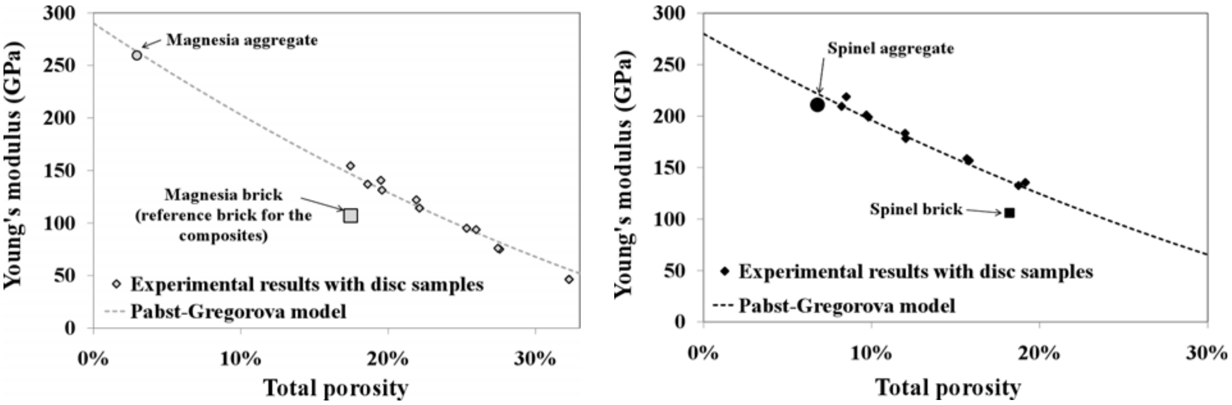

-a-　　　　-b-

Figure IV-1: Young's modulus evolution versus porosity of (a) magnesia (aggregate, disc samples and brick) and (b) spinel (aggregate, disc samples and brick), and comparison with the Pabst-Gregorova model

Finally, the experimental results obtained on spinel aggregates and on the magnesia reference brick are considered, in the next paragraph, as the values of Young's modulus of the two constituents of the magnesia-spinel composites, namely the spinel aggregates and the magnesia matrix.

I.2. Magnesia-spinel composites: spinel content influence and comparison with the Hashin and Shtrikman model

The experimental Young's modulus values previously obtained for the magnesia matrix and the spinel inclusions, namely 110 GPa and 210 GPa respectively, are considered in Figure IV-2 representing the Young's modulus evolution versus spinel inclusions content of the magnesia-spinel composites. These two values, corresponding, respectively, to 0% and 100% of spinel inclusions allow to deduce the lower bound of the Hashin and Shtrikman model (Figure IV-2) representing the hypothetical undamaged evolution of Young's modulus versus inclusions content. As a remark, due to their high heterogeneities, the experimental Young's modulus of the magnesia-spinel bricks were not obtained by usual ultrasonic measurements in infinite medium mode but by ultrasonic measurements in long bar mode allowing to work at lower frequencies.

As we could expect, the experimental and analytical results are not well correlated. According to the HS model, an increasing spinel inclusion content should increase Young's modulus of the composite, which is not observed experimentally. Indeed, it appears that increasing the spinel inclusion fraction induces a decrease in Young's modulus.

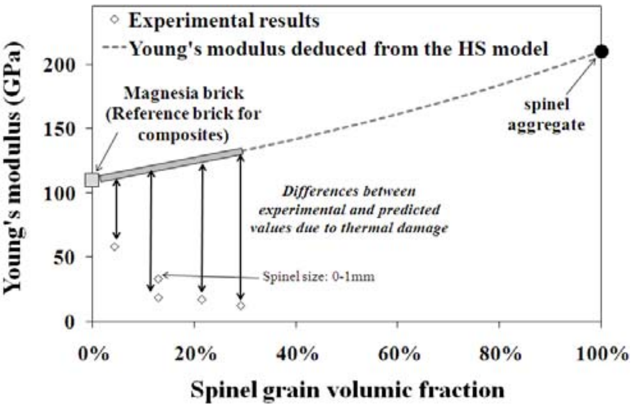

Figure IV-2: Evolution of experimental Young's modulus of the magnesia-spinel composites versus spinel inclusions content and comparison with the lower bound of the Hashin & Strikman model

In fact, lower Young's modulus values are in agreement with the presence of a microcracks network in these thermally damaged materials. Then, the spinel inclusion content (with a grain size of 1-3mm) seems to have a very high impact on the results since only 5 wt.% is enough to divide the Young's modulus by two. Furthermore, the composite containing 15 wt.% of 0-1mm spinel grains exhibits a higher Young's modulus than the one composed of 15 wt.% of 1-3mm spinel grains. Thus, the elastic properties at room temperature seem to be less affected with smaller inclusions. As a remark, Aksel et al. [AKS-03c] studied the influence of the addition of spinel inclusions within a magnesia matrix, but for fine-grained magnesia-spinel composites (several tens of micrometers), involving much higher Young's modulus values, and observed also a decrease of Young's modulus versus spinel content.

As mentioned before, thermal damage can be estimated by calculating the gap (%) to the Hashin and Shtrikman lower bound:

$$D_{th} = \frac{\left(E_{HS^-} - E_{\exp}\right)}{E_{HS^-}} \qquad \text{Eq. IV-2}$$

where D_{th}, E_{HS}- and E_{exp} are a thermal damage parameter (Kachanov type parameter [KAC-58]), the analytical (HS model) and the experimental Young's modulus values, respectively.

Figure IV-3 shows that the relation between the spinel content and the thermal damage parameter is not linear. In order to clarify the influence of the spinel inclusions (content and size) on the thermal damage of composites, high temperature investigations have been carried out and are presented in the next paragraph.

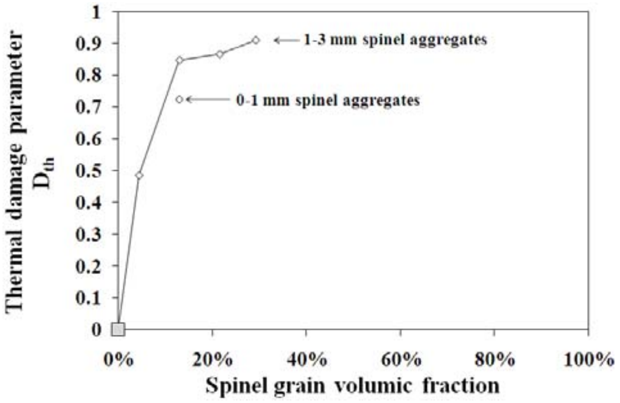

Figure IV-3: Evolution of the D_{th} thermal damage parameter, calculated from the experimental and theoretical (HS model) Young's modulus values

II. High temperature evolution: thermal micro damage during cooling

II.1. Evolution of Young's modulus in dependence of temperature

In a first step, the Young's modulus of the two single constituents of the composites were determined in dependence of temperature. To do that, long bar samples were extracted from elaborated bricks. For magnesia matrix, the magnesia reference brick, previously presented, was considered. For spinel inclusions, since it was experimentally not possible to characterise the

Young's modulus of a single aggregate at high temperature, a spinel brick has been elaborated (as shown in Figure IV-1b). Then, since the porosity of this spinel brick is much higher, and the Young's modulus much lower, than the one of a spinel aggregate (Figure IV-1b), the evolution of the Young's modulus of a spinel aggregate in dependence of temperature has been recalculated (Figure IV-4), by proportionality (correction factor), from the Young's modulus evolution of the spinel brick.

According to this figure, the evolutions of the Young's modulus of the magnesia matrix and the spinel inclusions, in dependence of temperature, are quasi linear, reversible and exhibit almost the same slope. Moreover, from these two evolutions, a theoretical undamaged evolution zone, provided by the Hashin and Shtrikman model for the magnesia-spinel composites and corresponding to a spinel content between 5 and 34 wt.%, has been added on Figure IV-4.

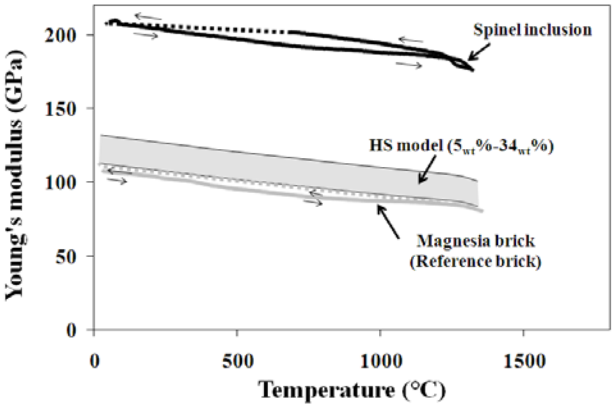

Figure IV-4: Evolutions of the Young's modulus of the two single constituents in dependence of temperature and theoretical evolutions (HS model) of the magnesia-spinel composites

In a second step, the evolutions of the Young's modulus of the magnesia-spinel composites, in dependence of temperature, were determined and compared to the Hashin and Shtrikman model. These experimental evolutions are shown in Figure IV-5a, with a spinel grain size of 1-3mm and different spinel contents (5-34 wt.%), and in Figure IV-5b, with a spinel content of 15 wt.% and different spinel grain sizes (0-1 mm and 1-3 mm). First, as already observed in Figure IV-2, the experimental values at room temperature are far below the analytical ones. Then, by considering the whole curves, it appears that the combination of the two single constituents provides hysteretic evolutions of the Young's modulus with a value at room temperature much lower than those of magnesia or spinel alone. This is characteristic for thermally damaged materials with microcracks in the microstructure [HUG-07]: the high increase and decrease of Young's modulus during thermal cycle are mainly due to microcracks closure (heating) and microcracks opening (cooling), respectively. The temperature corresponding to the beginning of crack opening, characterised by the maximum value, during cooling, seems to be the same for all of the model materials, namely 950°C approximately. Then, the major decrease in Young's modulus occurs in the 950°C-600°C range, approximately. According to the results obtained with 1-3mm spinel inclusions (Figure IV-5a), a higher spinel content induces a lower Young's modulus value at room temperature (already discussed in Figure IV-2). Of course, when temperature increases, the effect of thermal expansion mismatch tends to close microcracks and Young's modulus increases for all the composite materials, but the same classification is still observed at high temperature. In case of a fully crack healing, Young's modulus of composites should reach the estimated values of an hypothetical non-microcracked material (HS model). In fact, the maximum value at 950°C during cooling being rather lower than these values, it seems that, even at high temperature, microcracks are not fully closed within the different composite materials.

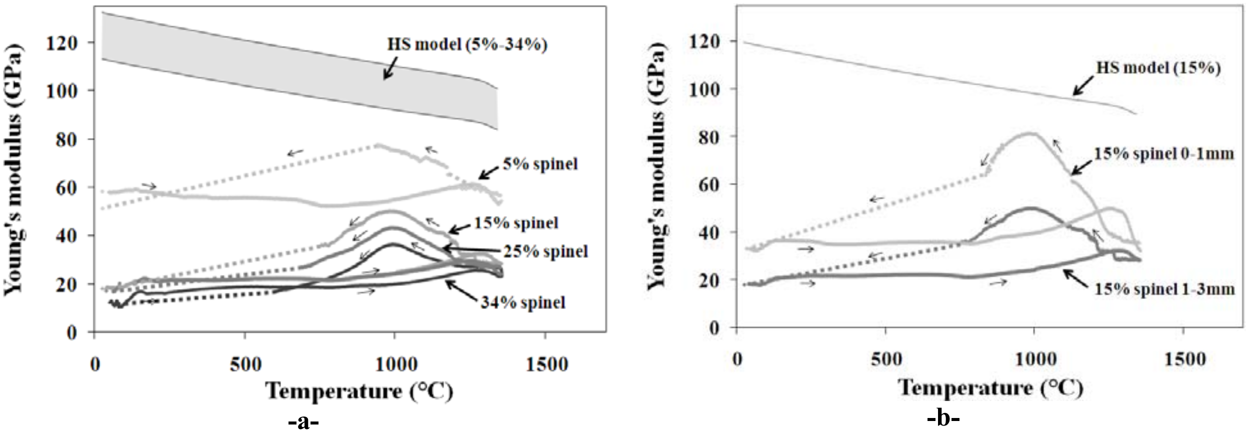

Figure IV-5: Evolutions of Young's modulus, in dependence of temperature, of the magnesia-spinel composites with a spinel grain size of 1-3mm and different spinel contents (a) and with a spinel content of 15wt.% and different spinel grain sizes (b)

According to Figure IV-5b, the 0-1mm composite exhibits a Young's modulus at room temperature higher than the 1-3mm composite (as already shown in Figure IV-2). Moreover, the relative amplitude of the increase/decrease of Young's modulus appears to be much higher for the 0-1mm composite than for the 1-3mm composite. In other words, smaller spinel inclusions involve higher Young's modulus values at room temperature (lower damage within the microstructure), and higher increase in Young's modulus during heating (easier microcracks closure). A possible explanation could be that microcracks, present in the microstructure of the 0-1mm composite, are smaller but more numerous. Indeed, this would justify the fact that the Young's modulus values are higher at room temperature. In addition, smaller microcracks could also facilitate closure mechanisms at high temperature.

As an additional remark, the measurement of Young’s modulus during the final stage of cooling is usually not possible due to failure of the alumina cement used to stick the sample to the waveguide because of thermal expansion mismatch between this alumina cement and the magnesia-spinel sample. By re-measuring the Young’s modulus at room temperature after the thermal cycle, the final evolution at the end of cooling is assumed and plotted in dotted line (Figure IV-5a). The thermal expansion mismatch between the alumina cement and the sample is higher when the spinel content is lower. This may explain why the loss of signal appears earlier during cooling for the 5% composite (Figure IV-5a), but also for the pure magnesia sample (Figure IV-4).

II.2. Evolution of the thermal expansion

The evolutions of thermal expansion of both single constituents and magnesia/spinel materials are presented in Figure IV-6. Firstly, the significant difference between the curves slopes of the magnesia and spinel samples highlights the thermal expansion mismatch existing between the two phases of the magnesia-spinel composites. Moreover, these two thermal expansion curves are not linear. The slopes at low and high temperature are quite different but reversible. Concerning the two-phase materials, the overall shape of the curves is closely related to the spinel inclusion volume fraction. During cooling, the slopes decrease significantly, especially at the end of cooling, which entails rather small residual thermal strain.

Furthermore, it has been observed previously that microcrack opening occurs during cooling, below 1000°C. Therefore, it may be of interest to determine the thermal expansion coefficients of the magnesia-spinel composites during cooling, above and below this temperature and to compare these values with the Hashin and Shtrikman model. A high difference between experimental and analytical results could again confirm microcracking. Thus, the evolution of the thermal expansion coefficient in dependence of the spinel inclusion content at both the beginning (1200-1000°C) and the end of cooling (400-200°C) are shown in Figure IV-7. It appears that the thermal expansion coefficients measured at the beginning of cooling are in very good agreement with the lower bound of the Hashin and Shtrikman model whereas those measured at the end of cooling are not so close to these analytical values. Indeed, these measured values are lower than this model and the relative difference seems to increase slightly when the spinel content increases. According to these observations, a huge part of the microcracks present in the microstructure seem to be closed at the beginning of cooling. At lower temperature, stress relaxation, involved by microcracks opening during cooling, leads to lower thermal expansion values than expected.

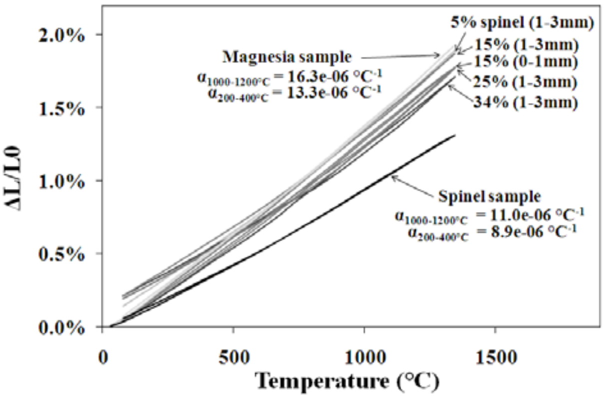

Figure IV-6: Evolutions of thermal expansion of the magnesia/spinel composites and the two constituents

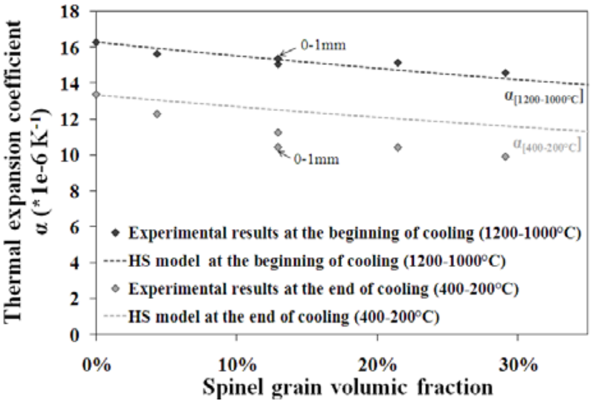

Figure IV-7: Influence of the spinel inclusion content on the thermal expansion coefficient of composites at both the beginning (1200-1000°C) and the end (400-200°C) of cooling

II.3. Evolution of acoustic emission at high temperature

Acoustic emission tests at high temperature were also carried out in order to validate the hypothesis of microcrack opening during cooling, below 1000°C, and to compare the results for the different magnesia-spinel composites. The acoustic emission results obtained for some of the considered materials are shown in Figure IV-8a and Figure IV-8b. According to Figure IV-8a, the acoustic activity of a magnesia sample is very low compared to those of the other materials. For these two model materials (5 wt.% and 15 wt.% of spinel), acoustic activity is slightly present during heating, but is much higher during cooling, especially between 950°C and 550°C. This is in good agreement with the previous observations regarding the evolutions of the Young's modulus in dependence of temperature. Indeed, the presence of a quite small number of hits during heating can be explained by the mechanical closure of microcracks [CHO-08] whereas the sudden high increase of hits during the cooling stage may be interpreted as the re-opening of microcracks caused by thermal expansion mismatches. Moreover, Figure IV-8a shows that a higher spinel content in model materials induces a higher cumulated number of hits during thermal cycling. This can be explained by the fact that more microcracks get opened during cooling when the spinel content is higher, as already proposed from Figure IV-5a.

Furthermore, according to Figure IV-8b, a smaller inclusion size seems to increase significantly the total cumulated number of hits. This would justify the fact that, as previously assumed from Figure IV-5b, the number of microcracks in the 0-1mm composite is higher than the one in the 1-3 mm composite, even if these "small" microcracks affect less the Young's modulus value.

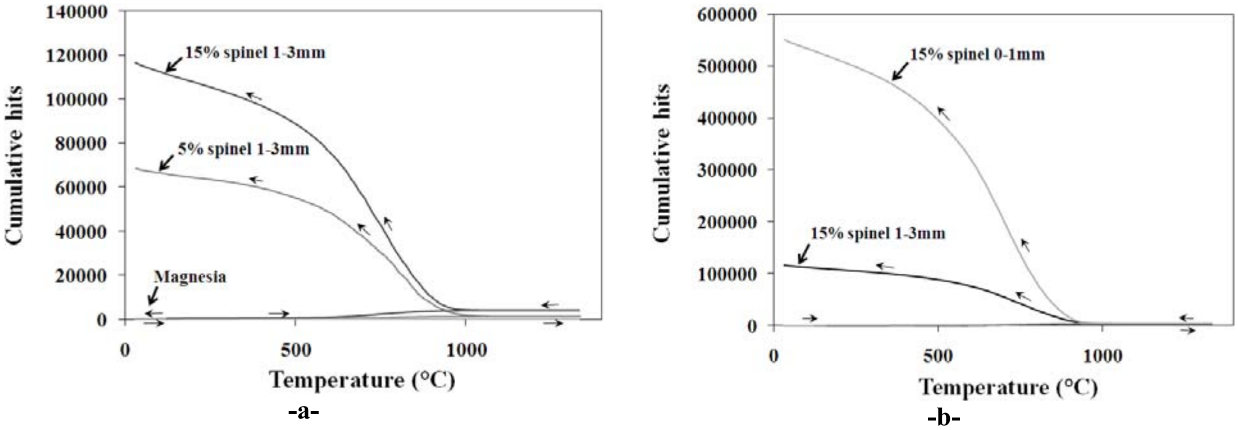

Figure IV-8: Evolution of acoustic emission versus temperature during thermal cycle up to 1350°C – Influence of the spinel inclusions content (a) and the spinel grain size (b)

III. Influence of thermal micro damage on the mechanical behaviour under tension at room temperature

As previously explained in Chapter I, in reference to literature, the non-linear fracture, the rising R-curve phenomenon and the thermal shock damage resistance are very linked together and the way of improving them is to control the microstructure design. Here, the main changing microstructural parameter is the spinel inclusions content which is closely related to the thermal damage parameter D_{th} (see the previous paragraph). Thus, the thermal micro damage within the magnesia-spinel composites, which occurs during cooling, may have a significant influence on the mechanical behaviour of such materials.

III.1. Stress-strain curves obtained by tensile tests

The stress-strain curves of the single constituents, obtained by tensile tests, are presented in Figure IV-9a and Figure IV-9b. The mechanical behaviours of these two constituents are very different. Indeed, the spinel material (Figure IV-9a) exhibits a nearly linear elastic behaviour with very small damage and a total failure at very low strain level which is characteristic for brittle materials. Concerning the magnesia material, some experimental difficulties have been encountered, which made it impossible to get the entire peak (Figure IV-9b). This problem, also obtained with industrial pure magnesia products, could be due to the combination of magnesia property (micro-damage, plasticity, rupture by cleavage) [DAV-79, GAI-06, STO-63, DAY-64, PAT-70, MAT-04] and inappropriate tensile test device rigidity. The retained solution to overcome this problem was to find a suitable function fitting the valid data in order to re-build an assumed stress-strain curve (assumed curve in Figure IV-9b). Nevertheless, the tensile strength deduced from the assumed curve, and considered later for the calculation of mechanical parameters, might be, all the same, underestimated. Anyway, unlike the spinel material, the magnesia material presents a non-linear behaviour (rather small) before the peak with a significant post-peak region and a high strain to rupture. This behaviour is not common at room temperature for homogeneous ceramic materials and seems to be not so far from the so-called quasi-brittle behaviour of concretes, and some polyphase refractories. A possible explanation of this behaviour is the coarse grain size (1-3 mm and 3-5 mm) distribution of this material (see Table II-3) which was reported to potentially improve fracture and thermal shock resistance of magnesite refractories [UCH-76]. This quasi-brittle behaviour will be taken into account in the simulation part (Chapter V), as well as the linear elastic behaviour of the spinel inclusions.

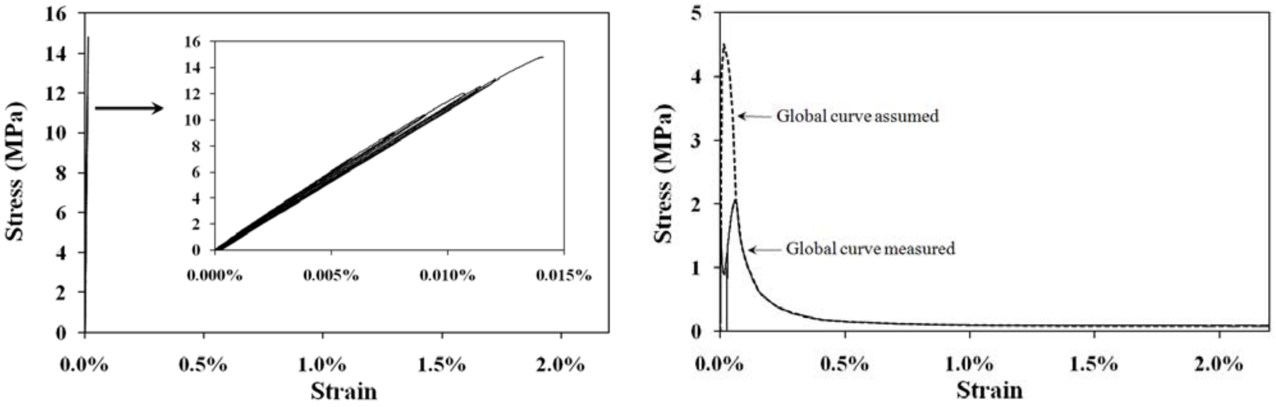

-a- -b-

Figure IV-9: Stress-strain curves of the pure spinel (a) and the pure magnesia (b) materials obtained by tensile tests (Due to experimental problems, the real peak of the curve (b) was not obtained and had to be assumed)

All the magnesia-spinel composites were characterised in tension. But, in order to be able to compare clearly the global curves, with their loading/unloading cycles, only three of them are represented in Figure IV-10a, namely 5, 15 and 25% of spinel inclusions (1-3 mm). According to this figure, the global stress-strain curves in tension present a non-linear mechanical behaviour up to the peak with a significant post-peak region and residual strain when unloading. Moreover, the increase of spinel content seems mainly to decrease the tensile strength. The very beginning of the stress-strain curves of the different composites, as well as the single constituents are presented in Figure IV-10b. It appears that an increasing spinel inclusions content increases the non-linearity of the mechanical behaviour in tension due to a denser pre-existent microcracks network developed during cooling.

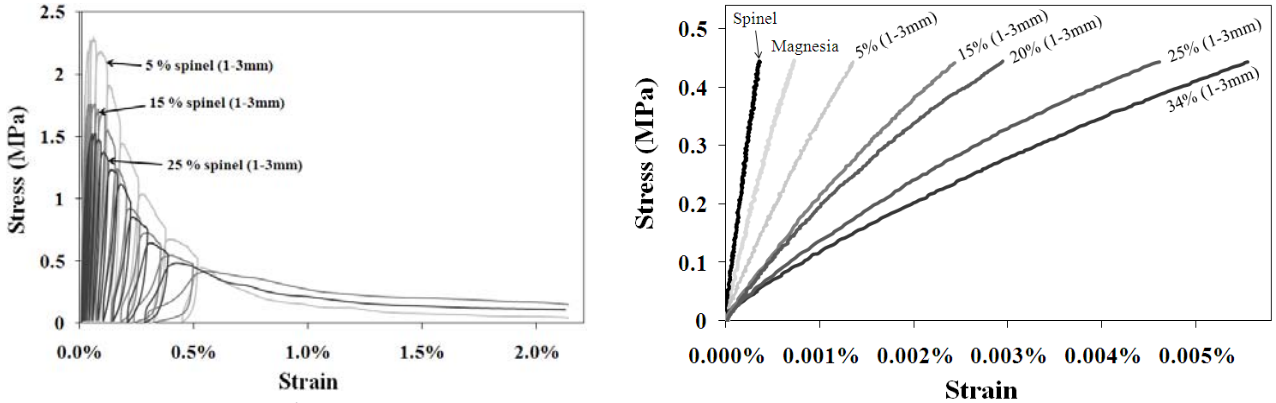

-a- -b-

Figure IV-10: (a) Example of global stress-strain curves obtained with different magnesia-spinel composites, (b) Comparison of the stress-strain curves obtained with both single materials and composites at their very beginning

In order to understand better the influence of thermal damage on the mechanical behaviour, a mechanical damage parameter (Kachanov [KAC-58] type), noted D_{th+mec}, is proposed as follows:

$$D^{i}_{th+mec} = \frac{E_{HS} - E^{i}_{TT}}{E_{HS}} \qquad \text{Eq. IV-3}$$

where E_{HS}, E^{i}_{TT} and D^{i}_{th+mec} are, respectively, the hypothetical undamaged Young's modulus deduced from the lower bound of the Hashin and Shtrikman model, the experimental Young's modulus at the i^{th} unloading/loading cycle of a tensile test (Figure IV-11a), and the calculated value of the mechanical damage parameter at this i^{th} cycle.

The fact that the reference Young's modulus value used to calculate D^{i}_{th+mec} is not the value measured at the first loading step, as usually done, but the analytical HS value, allows to take into account the initial thermal damage occurred during the previous cooling stage of the process. Indeed, the initial value of D_{th+mec} (at $\varepsilon = 0$) corresponds to the value of D_{th} previously calculated. The evolutions of this mechanical damage parameter versus strain of the magnesia-spinel composites and the single constituents are shown in Figure IV-11b. First, as expected, it can be pointed out that, unlike the two single constituents, the magnesia-spinel composites present initial damage before loading in tension. Otherwise, for the spinel material, the increase in mechanical damage is very fast compared to the others and a total failure occurs at very low strain level. The magnesia material also exhibits an increase in damage, but much more progressive with increasing strain value. In the same trend, the mechanical damage within the magnesia-spinel composites occurs more slowly than the two constituents when the strain increases, and, like magnesia, in a progressive way. Finally, the thermal damage occurred within these composites during cooling seems to make them less sensitive to mechanical damage (the materials accept especially high level of damage) and, then, more tolerant to high strain levels, which may, therefore, improve their thermal shock damage resistance.

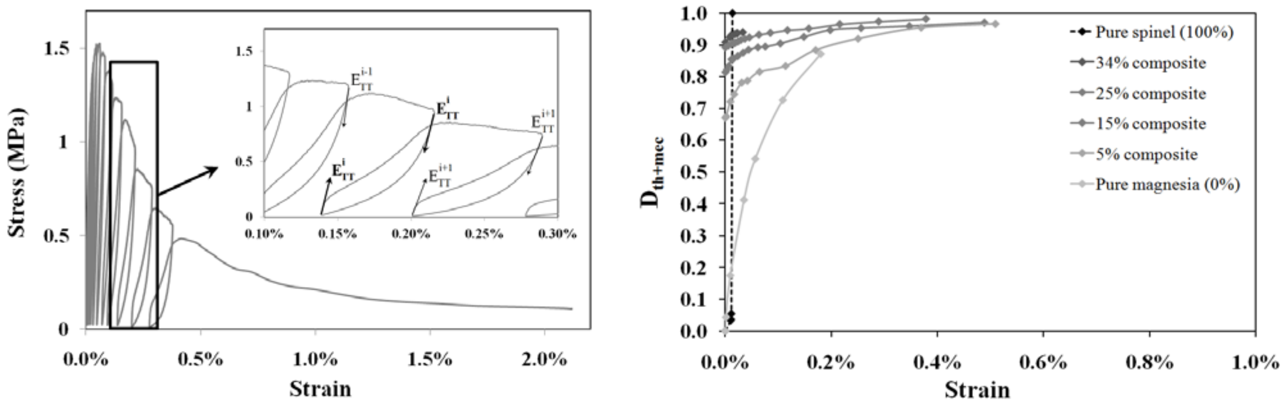

-a-

-b-

Figure IV-11: (a) Determination of the Young's modulus E_{TT} during the whole tensile test allowing to estimate the mechanical damage parameter D_{th+mec}, (b) Evolutions of the mechanical damage parameters D_{th+mec}, taking into account initial thermal damage, of the single and two-phase materials versus strain

III.2. Force-displacement curves obtained by wedge splitting tests

The global force-displacement curves of the pure magnesia and the magnesia-spinel composites obtained by wedge splitting tests are shown in Figure IV-12a. As expected, the mechanical behaviour of magnesia is very different from the other ones since it exhibits a much higher maximum force, a lower strain at the peak, and a thinner peak due to a smaller post-peak region. This is in agreement with the previous observations from tensile test results. Concerning the composites, the increase of spinel content mainly lowers the maximum force but does not influence so much the end of the post-peak region since they are all very close. By considering the very beginning of these force-displacement curves (see Figure IV-12b), it appears, as already observed from tensile tests results, that the spinel addition, and, therefore, the thermal damage introduction, allows to enhance the non-linearity of the mechanical behaviour, especially when the spinel content increases.

As mentioned in Chapter I, this non-linearity, as well as the post-peak regions, is mainly caused by toughening mechanisms occurring around the crack, especially in the following wake region, which may increase the resistance to crack propagation. Thus, it seems interesting, in the future, to be able to identify, from microstructure micrographs (example in Figure IV-13), the evolution of all the deformation phenomena occurring during a wedge splitting test, and compare the results for these different materials. In fact, from micrographs, only the main macrocrack can be detected by the naked eye (Figure IV-13b), but the early apparition of the macrocrack, as well as all the stressed microcracks pre-existing around the middle plane, is not really visible. A work based on Digital Image Correlation (D.I.C.), which should allow to get strain fields versus time from all the micrographs taken during a test, has been begun during the FIRE Master project of Y. Belrhiti [BEL-11] but is still in progress.

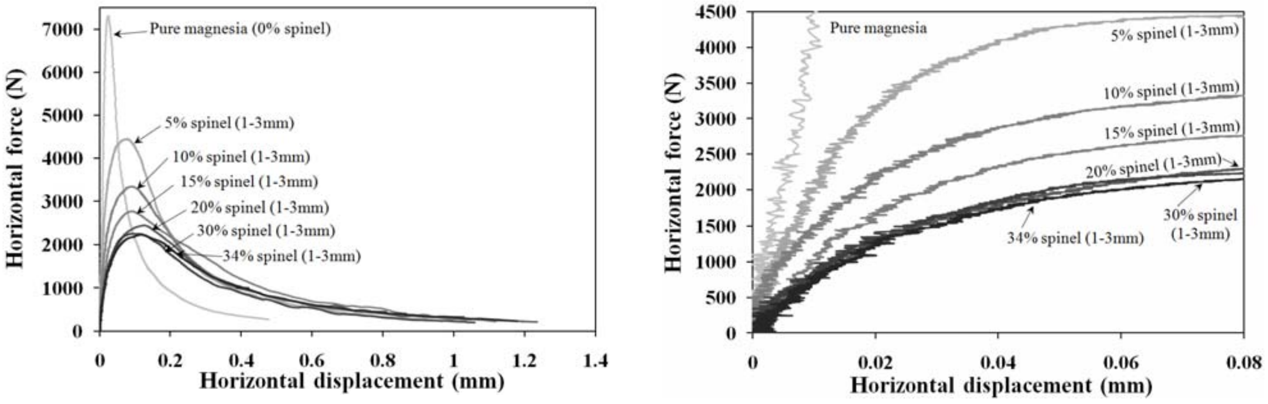

-a- -b-

Figure IV-12: Force-displacement curves of the magnesia material and the magnesia-spinel composites obtained by wedge splitting tests (a) and zoom on the very beginning of these curves (b)

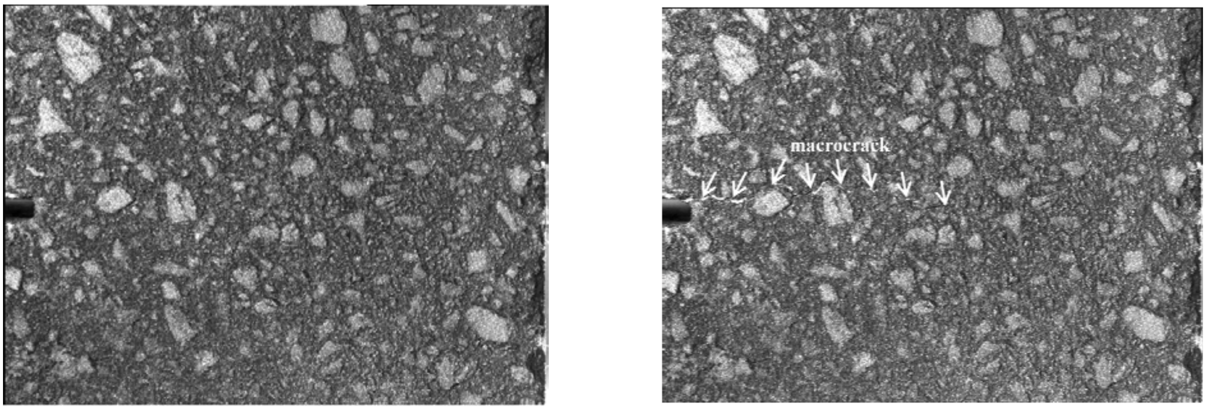

-a- -b-

Figure IV-13: Micrographs at the beginning (a) and during (b) a wedge splitting test on a magnesia-spinel composite with 15% of spinel (1-3mm)

III.3. Tensile and wedge splitting tests: evolution of common key parameters and correlation analysis

III.3.1. Presentation of common mechanical parameters from the two techniques

The tensile and wedge splitting tests are complementary techniques since they do not give exactly the same information. The tensile test, without any notch, provides the stress-strain behaviour of the materials which is often required in numerical models. This test is suitable for the investigation of the non-linearity of the mechanical behaviour before localisation of a macrocrack when the whole sample volume is stressed, inducing a diffuse damage in the volume. The wedge splitting test, having a notch, allows to investigate the formation of a macrocrack and its stable propagation within the sample. The damage is supposed to be mainly concentrated in the section plane below the notch. The non-linearity of the mechanical behaviour can also be investigated even if it does not correspond exactly to the same phenomena as for a tensile test. Indeed, the latter provides the tensile strain while the wedge splitting test provides the crack opening strain in tension.

Although these two mechanical tests are quite different, they both allow to apply uniaxial tension within the studied samples and, thus, provide crucial information concerning the fracture process of the considered material. Therefore, it seems of interest to introduce mechanical parameters for both tests allowing to provide comparable information. A significant work of synthesis was done in order to provide accurate formulas for each couple of parameters. Indeed, as explained below, some differences in the way of calculating the fracture energy entail slightly different formulas for the wedge splitting and tensile tests. Some details, here, concerning these formulas, especially for the thermal shock parameters, might be found to be long by the reader but are, nonetheless, essential for a better understanding.

III.3.1.1. Tensile strengths and fracture energies

Tensile strengths and fracture energies can be directly deduced from the stress-strain (Figure IV-14a) and force-displacement (Figure IV-14b) curves obtained by tensile and wedge splitting tests, respectively.

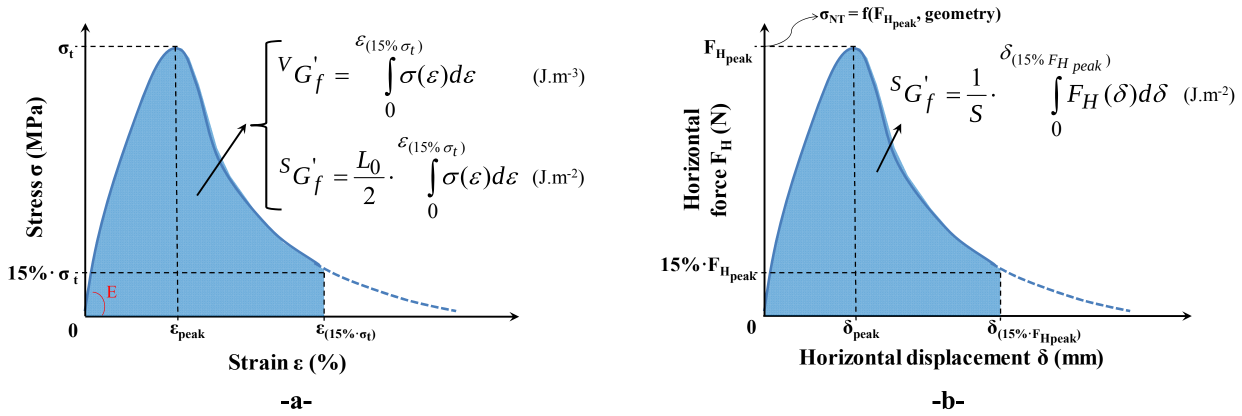

Figure IV-14: Tensile strengths (σ_t and σ_{NT}), and fracture energies ($^{V}G'_f$ and $^{S}G'_f$) obtained from tensile (a) and wedge splitting tests results (b)

The tensile strength σ_t (Figure IV-14a) corresponds to the maximum stress (at the peak) of the stress-strain curve obtained by tensile test. The nominal notch tensile strength σ_{NT} (Figure IV-14b) is deduced from the maximum horizontal force $F_{H_{\max}}$ of the force-displacement curve, obtained by wedge splitting test, as follows [AUE-06]:

$$\sigma_{NT} = \frac{F_{H_{\max}}}{b \cdot h} + \frac{6 \cdot F_{H_{\max}} \cdot y}{b \cdot h^2} \qquad \text{Eq. IV-4}$$

where b and h are the width and the height of the ligament, respectively, and y is the vertical distance from the horizontal force F_H to the centre of gravity of the ligament.

Although these two tensile strengths are not exactly the same (addition of tensile and bending stresses for σ_{NT}), they are considered later for comparison.

The fracture energies are deduced from the total area under the curves obtained by tensile and wedge splitting tests. The determination of the area under the stress-strain curve (tensile test) provides directly a volume fracture energy, $^{V}G_f$ (J.m^{-3}), while the surface fracture energy, usually obtained from wedge splitting test, called specific fracture energy, $^{S}G_f$ (J.m^{-2}), corresponds to the area under the force-displacement curve divided by the section S (see the formula in Figure IV-14b). Moreover, since wedge splitting tests are here not carried out until total rupture, the fracture energy is calculated until 15% of the maximum force ($F_{H_{\max}}$) after the peak and the so-calculated fracture energy is noted $^{S}G'_f$ (Figure IV-14b). For pertinent comparisons, the volume fracture energy obtained by tensile test is also calculated until 15% of the tensile strength (σ_t) after the peak and noted ${}^{V}G_f^{'}$ (Figure IV-14a). As a remark, for the calculation of the volume energy, since the stress-strain curve exhibits different loading/unloading cycles, only the upper envelope of this curve has been considered.

Otherwise, it is possible to get a surface fracture energy from the tensile test by considering the sample section instead of the sample volume (multiplication of the volume energy by the gauge length L_0, Figure IV-14a). Nevertheless, surface fracture energy, for tensile tests, will be calculated only when required for the calculation of thermal shock resistance parameters. It must be pointed out that the calculation of this surface fracture energy involves a factor ½, as it was proposed for the calculation of the work-of-fracture (Eq. I-8), since two surfaces are created. This factor ½ is not considered in the calculation of the specific fracture energy obtained by wedge splitting test. Therefore, when calculating the thermal shock resistance parameters (see next paragraph), the factor ½ will have to appear for wedge splitting test.

III.3.1.2. Energetic brittleness numbers and thermal shock resistance parameters

Energetic brittleness numbers were proposed in literature in order to be able to classify refractories according to their reduced brittleness which is closely related to thermal shock resistance. First, Gogotsi et al. introduced a brittleness number [GOG-78], called here B_1, as the ratio of the specific elastic energy accumulated in the material at fracture to the whole specific energy expended to attain the peak (see Figure IV-15a):

$$B_1 = \frac{\sigma_t^2 / 2E}{\int_0^{\varepsilon_{peak}} \sigma(\varepsilon) d\varepsilon} \qquad \text{Eq. IV-5}$$

where σ_t, ε_{peak} are the stress and the strain at the peak and E is the initial Young's modulus which is assumed to be unchanged at the peak for the calculation of the stored elastic energy.

It can be noticed that this dimensionless brittleness number, is a ratio of two volume energies.

For the present study, similarly to the Gogotsi's brittleness number, another ratio $B_2^{'}$ can be calculated from the tensile test results by also considering the post-peak region of the curve with the volume fracture energy ${}^{V}G_f^{'}$ (see Figure IV-15b):

$$B_2^{'} = \frac{\sigma_t^2 / 2E}{{}^{V}G_f^{'}} \qquad \text{Eq. IV-6}$$

Otherwise, since the specific fracture energy measured by wedge splitting test is a surface energy, Harmuth et al. suggested [HAR-97] to use the following brittleness number, noted here B':

$$B^{'} = \frac{\sigma_{NT}^2 \cdot L}{{}^{S}G_f^{'} \cdot E} \qquad \text{Eq. IV-7}$$

where σ_{NT} and L are the nominal notch tensile strength obtained by wedge splitting test and a specimen dimension, respectively.

A specific dimension of the specimen, L, has to be introduced here because the dimensionless brittleness number B', calculated from wedge splitting tests, does not involve two volume energies but the surface specific fracture energy ${}^{S}G_f^{'}$ (J.m^{-2}) and the volume elastic energy accumulated in the material at fracture. This dimension, representative of a wedge splitting test sample, is arbitrarily chosen and, therefore, the brittleness number B', calculated for wedge splitting tests, should not be directly compared with the brittleness numbers calculated for other techniques, like tensile tests ($B_2^{'}$). Nonetheless, the comparison of their relative evolution, in dependence of either inclusion content or thermal damage parameter, seems possible.

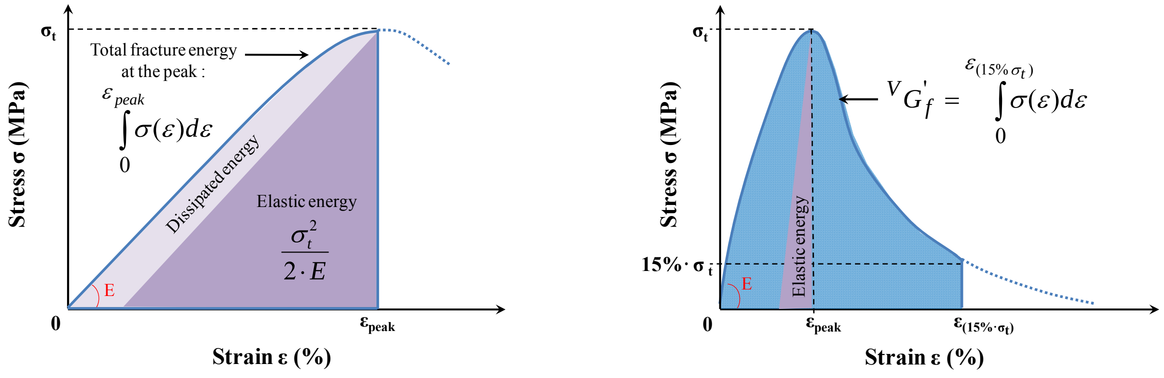

-a- -b-

Figure IV-15: Schematic representations of elastic energy and total energy considered for the calculation of the brittleness numbers B_1 [GOG-78] (a) and $B_2^{'}$ (b) from tensile tests results

As discussed in Chapter I (paragraphs II.1. and II.2.), the thermal shock resistance parameters R'''' and R_{st}, firstly introduced by Hasselman, depended on the surface fracture energy γ_s and then, later, it was proposed to calculate these parameters from the work of fracture γ_{WOF} instead of γ_s. In a similar way, it has been proposed, here, to replace γ_s by the fracture energies ${}^{S}G'_f$ previously introduced for tensile and wedge splitting tests. Indeed, in order to respect the unit of these parameters (R'''' in m and R_{st} in K.m$^{1/2}$), the fracture energy considered here for the tensile test is the surface one (${}^{S}G'_f$). Furthermore, as explained above, the specific fracture energy obtained from wedge splitting tests does not include the factor ½ normally introduced when dealing with surface fracture energies (see calculation of the work of fracture Eq. I-8) unlike the one obtained from tensile tests which includes it. Therefore, for the wedge splitting test, this factor ½ has to be introduced in the formulas of the thermal shock resistance parameters.

Finally, the formulas used to calculate the R_{st} and R'''' thermal shock resistance parameters, from the tensile and wedge splitting tests results, are presented in Table IV-1. Otherwise, a fracture mechanical parameter, called characteristic length [HIL-83] l'_{ch}, is usually calculated from the wedge splitting tests results, as shown in Table IV-1. Since this characteristic length is inversely proportional to B', it can also provide information on brittleness without introducing the specimen size L needed in the formula of B'. The formula used to calculate this characteristic length from wedge splitting tests results has been extended to the case of tensile tests results and introduced in Table IV-1. Now, by comparing the formulas of R'''' and l'_{ch} for one kind of test, it appears that they are quasi-similar since: $R'''' = l'_{ch}/2$. Therefore, these two parameters will provide exactly the same information. Thus, only the characteristic length l'_{ch} is calculated in the next results. Although this length is not denominated as a thermal shock resistance parameter, it will, all the same, give information on the ability to sustain thermal shocks.

	Thermal shock resistance parameters		**Fracture mechanical parameter**
	R_{st}	**R''''**	**l'_{ch}**
Wedge splitting test	$R_{st} = \sqrt{\frac{{}^{S}G'_f}{2 \cdot \alpha^2 \cdot E}}$	$R'''' = \frac{{}^{S}G'_f \cdot E}{2 \cdot \sigma_{NT}^2}$	$l'_{ch} = \frac{{}^{S}G'_f \cdot E}{\sigma_{NT}^2}$
Tensile test	$R_{st} = \sqrt{\frac{{}^{S}G'_f}{\alpha^2 \cdot E}}$	$R'''' = \frac{{}^{S}G'_f \cdot E}{\sigma_t^2}$	$l'_{ch} = \frac{2 \cdot {}^{S}G'_f \cdot E}{\sigma_t^2}$

Table IV-1: Formulas used to calculate the parameters R_{st}, R'''' and l'_{ch} from wedge splitting and tensile tests

III.3.2. Evolution of the mechanical parameters in dependence of the spinel content and the thermal damage parameter

The evolutions of these common mechanical parameters in dependence of the spinel inclusions fraction and the thermal damage parameter D_{th} were determined. Indeed, since the thermal damage within the composites is not proportional to the spinel content, the dependence of these parameters on D_{th} seem of particular interest to investigate the thermal damage influence. In this part, only the magnesia-spinel composites with spinel grain size of 1-3 mm are considered.

Concerning the tensile strengths σ_{NT} and σ_t, obtained from the wedge splitting and tensile tests results, theirs evolutions versus inclusion fraction and thermal damage parameter are shown in Figure IV-16a and Figure IV-16b, respectively. First, in both figures, the global shape evolutions obtained with the two techniques are rather similar. Then, as expected, the spinel inclusions addition decreases the tensile strengths, especially at low spinel content (Figure IV-16a). Moreover, according to Figure IV-16b, the increase of thermal damage obviously decreases the tensile strength, and the relation between the tensile strength and the thermal damage parameter appears nearly linear.

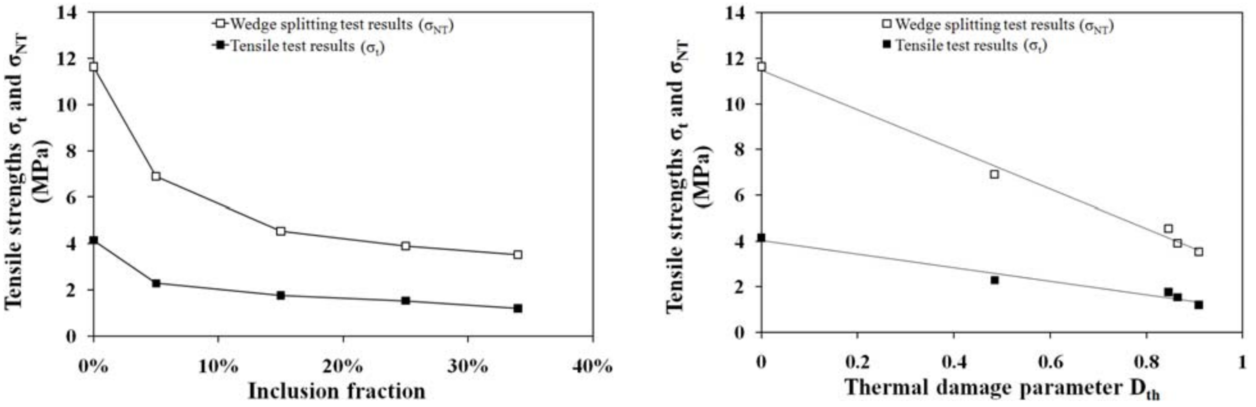

-a- -b-

Figure IV-16: Evolutions of the nominal notch tensile strength σ_{NT} (wedge splitting test) and the tensile strength σ_t (tensile test) versus spinel inclusion fraction (a) and versus thermal damage parameter (b)

The dependences of the fracture energies $^{S}G'_{f}$ and $^{V}G'_{f}$, obtained from the wedge splitting and tensile tests results on inclusions content and thermal damage parameter are presented in Figure IV-17a and Figure IV-17b, respectively. As a remark, there is no result of energy for the 34%-composite obtained by tensile test since it has not been possible to characterise experimentally the post-peak behaviour. For this content, only the stress-strain curve with pre-peak region is considered as a result. Therefore, the parameters involving the fracture energy in their formulas, will not be calculated for this content.

Even if the values of energy are totally different (not the same unit), the global shape evolutions are again quite similar. First, it can be pointed out that the fracture energy of the pure magnesia material, without any addition of spinel inclusions, is already significantly higher than common homogeneous ceramics which are often brittle and present low fracture energies. Secondly, it appears that the addition of spinel allows to increase the fracture energy. Indeed, with only 5 wt.% of spinel inclusions, the thermal damage parameter is rather high (around 0.5) and the increases in fracture energies are above 50%. Such increase of surface fracture energy is in the same range as the one observed by Aksel et al. [AKS-03c] with work-of-fracture tests on fine-grained composites. Nevertheless, with higher spinel contents, and, so, higher thermal damage, the fracture energy is no longer increased but remains in the same range.

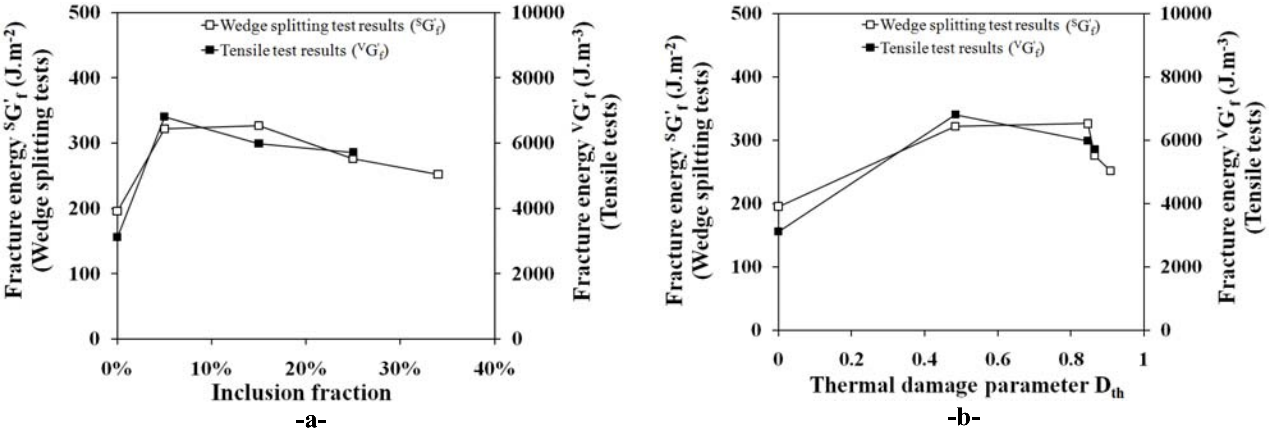

-a- -b-

Figure IV-17: Evolutions of the fracture energies $^{S}G'_f$ (wedge splitting test) and $^{V}G'_f$ (tensile test) versus spinel inclusion fraction (a) and versus thermal damage parameter (b)

Furthermore, Harmuth et al. [HAR-10a, HAR-10b] showed that an industrial magnesia-spinel product does not necessarily present a higher specific fracture energy than an industrial pure magnesia product due to its much lower tensile strength. Thus, they proposed to quantify the ratio of fracture energy to tensile strength, which might be considered as another indicator of brittleness. This ratio, linked to the ultimate crack opening, does not depend on the Young's modulus value. The evolutions of the $^{S}G'_f/\sigma_{NT}$ ratio (in m), for the wedge splitting test, and the $^{V}G'_f/\sigma_t$ ratio (dimensionless), for the tensile test, versus inclusion content and thermal damage parameter are shown in Figure IV-18a and Figure IV-18b. The increase of spinel content allows to increase these ratios, especially at low spinel content. Moreover, the increase of these ratios is nearly linear when considering the thermal damage parameter instead of the spinel content.

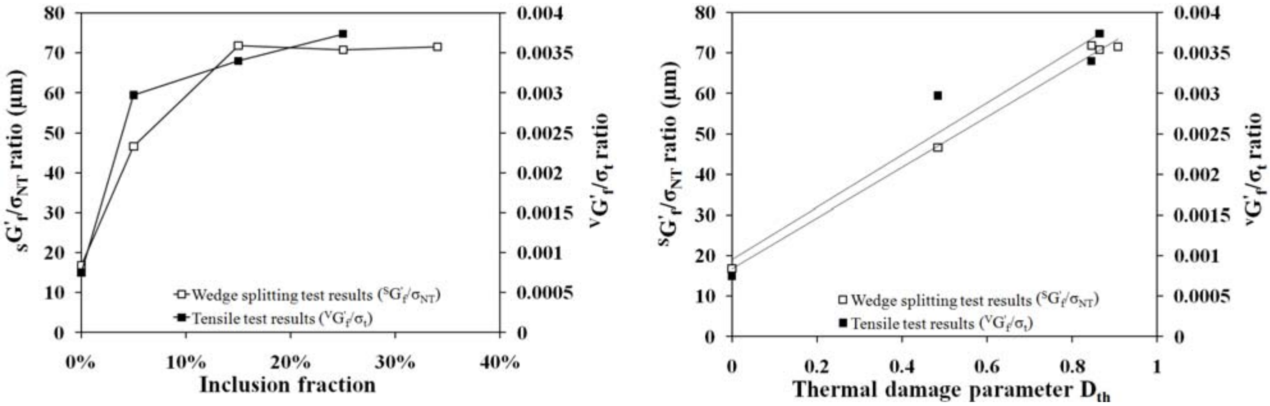

-a- -b-

Figure IV-18: Evolutions of the ${}^{S}G'_f/\sigma_{NT}$ (wedge splitting test) and ${}^{V}G'_f/\sigma_t$ (tensile test) ratios versus spinel inclusion fraction (a) and versus thermal damage parameter (b)

The dependences of the brittleness numbers B' and B'_2, obtained from the wedge splitting and tensile tests results, on inclusions content and thermal damage parameter are presented in Figure IV-19a and Figure IV-19b, respectively. Firstly, even though the B' and B'_2 values cannot be compared (arbitrary L value in B'), it can be pointed out that their global shape evolution versus both spinel content and thermal damage parameter are rather similar since they both exhibit a decrease of brittleness when increasing the spinel inclusion content, and thus, when increasing the thermal damage. Similarly to the previous parameters, the main decrease is observed at low inclusion fraction (< 5 wt.% in Figure IV-19a) and thermal damage parameter (< 0.5 in Figure IV-19b).

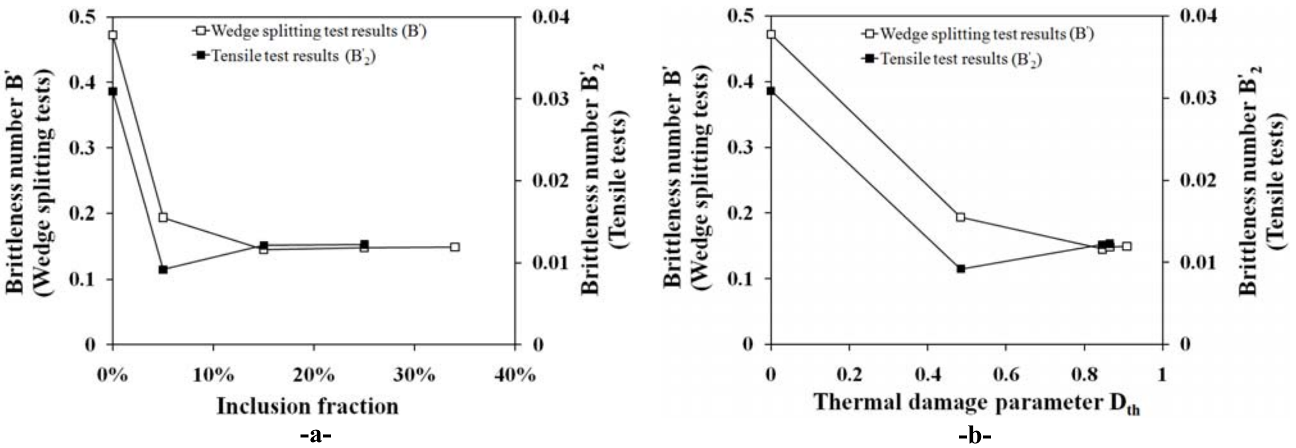

-a- -b-

Figure IV-19: Evolutions of the brittleness numbers B' (wedge splitting test) and B'_2 (tensile test) versus spinel inclusion fraction (a) and versus thermal damage parameter (b)

Concerning the parameters linked to the ability to sustain thermal shocks, the dependences of l'_{ch} on spinel content and thermal damage parameter are shown in Figure IV-20a and Figure IV-20b, while those of R_{st} are presented in Figure IV-21a and Figure IV-21b. According to Figure IV-20, the increase in inclusion fraction and in thermal damage globally increases the l'_{ch} values but those obtained from tensile test are rather higher than those obtained from wedge splitting test, which might come from the rather low tensile strength values obtained from the first test (see the formula of l'_{ch} in Table IV-1). Moreover, a maximum is observed for l'_{ch} (tensile test) while l'_{ch} (wedge splitting test) presents a monotonic increase. According to Figure IV-21, the R_{st} evolutions appear to be very close for the two techniques. By increasing the spinel inclusion fraction (Figure IV-21a), the R_{st} values progressively increase (faster at low content). Regarding the influence of the thermal damage parameter (Figure IV-21b), it appears that its increase makes the R_{st} parameter increase nearly linearly. As a remark, these results show that the spinel addition will allow to increase the values of the R_{st} and l'_{ch} parameters, and, therefore, improve the thermal shock resistance of such magnesia-based materials. Of course, thermal shock resistance tests should be carried out to confirm it.

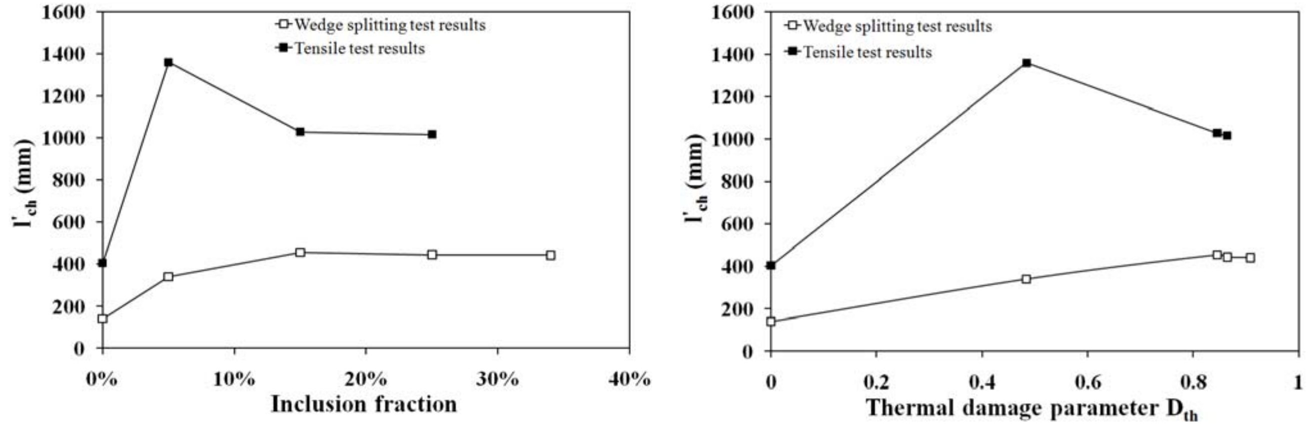

-a- -b-

Figure IV-20: Dependences of the thermal shock resistance parameters l'_{ch} (wedge splitting test) and R'''' (tensile test) on spinel inclusion fraction (a) and thermal damage parameter (b)

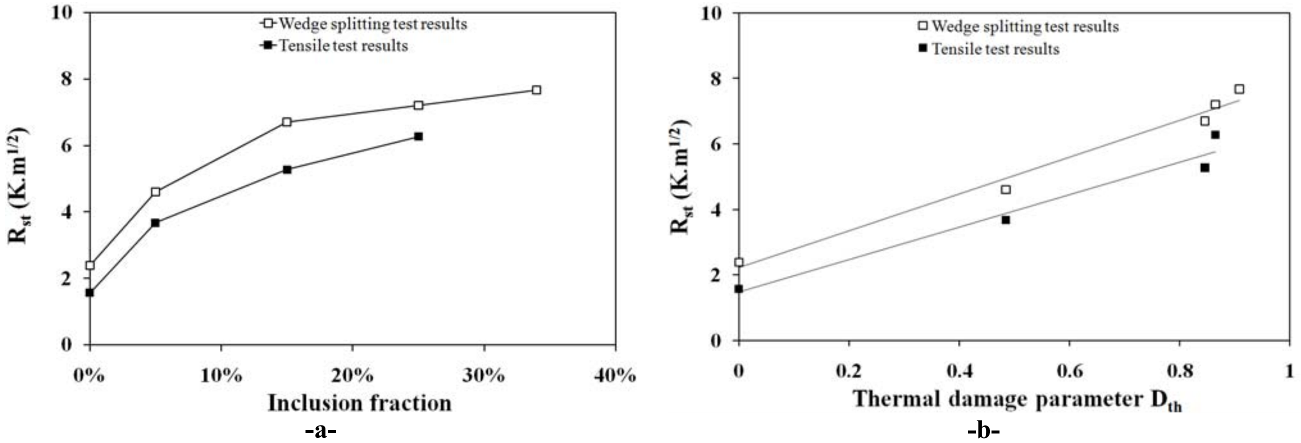

-a- -b-

Figure IV-21: Dependences of the thermal shock resistance parameter R_{st} (obtained from tensile and wedge splitting tests) on spinel inclusion fraction (a) and thermal damage parameter (b)

III.3.3. Correlation analysis

The paragraph III.3.2. has allowed to study the influence of spinel fraction and thermal damage on the different common mechanical parameters. In fact, since most of these dependences seem similar, or inversely similar, it seems of interest to quantify the degree of correlation between these parameters, and other interesting ones. Doing that, in addition to the previous paragraph, the influence of spinel content and thermal damage could be quantified and, in further analysis, the way of improving thermal shock resistance could be discussed.

All the parameters which are considered here are presented in Table IV-2 with the obtained experimental values. The analysis of their correlation was carried out by the use of correlation matrices (Figure IV-22 and Figure IV-23), and separately for tensile and wedge splitting tests results in order to compare, at the same time, if the characteristics provided by the two techniques are similar. Without going into details concerning the procedure providing the correlation matrix, it can be pointed out that each coefficient within this matrix allows to estimate the degree of correlation between two parameters but the knowledge of this matrix, alone, does not allow to determine which parameter is the cause and which one the consequence (no information on causation). Moreover, only one half of the matrix (either above or below the diagonal) has to be completed since this matrix is symmetric.

Spinel content $\%_{spinel}$ (wt.%)			0%	5%	15%	25%	34%
Thermal damage D_{th}			0.00	0.48	0.85	0.87	0.91
Young's modulus	**E_{TT} (GPa)**		89	42	21	17	12
	E_{RFDA} (GPa)		97	50	29	25	22
Tensile strengths	**TT**	**σ_t (MPa)**	4.2	2.3	1.8	1.5	1.2
	WST	**σ_{NT} (MPa)**	11.6	6.9	4.5	3.9	3.5
Fracture energies	**TT**	**$^{V}G'_{f}$ ($J.m^{-3}$)**	3120	6810	5980	5720	_
	WST	**$^{S}G'_{f}$ ($J.m^{-2}$)**	196	322	326	276	252
Brittleness	**TT**	**B'_2**	0.031	0.009	0.012	0.012	
	WST	**B'**	0.47	0.19	0.15	0.15	0.15
Thermal shock resistance	**TT**	**R_{st} ($K.m^{1/2}$)**	1.6	3.7	5.3	6.3	_
	WST	**R_{st} ($K.m^{1/2}$)**	2.4	4.6	6.7	7.2	7.7
	TT	**l'_{ch} (mm)**	405	1360	1029	1017	_
	WST	**l'_{ch} (mm)**	140	341	455	445	442
Thermal expansion α ($\cdot 10^{-6}$ K^{-1})			13.3	12.3	11.2	10.4	9.9

TT, WST and RFDA account for tensile test, wedge splitting test and resonance frequency technique

Table IV-2: Experimental results considered in the correlation analysis

The two correlation matrices obtained from wedge splitting and tensile tests results are shown in Figure IV-22 and Figure IV-23, respectively. In order to represent and compare in a more global way all the data, another form of representation has been proposed. Indeed, since for each type of parameters (ex: tensile strengths, fracture energies...), the sign of its correlation with the other ones is the same for both tensile and wedge splitting tests, radar diagrams (Figure IV-24a to Figure IV-24f) have been plotted by taking into account the absolute values (negative values are not possible with this representation). The blue and dark red plotted areas correspond to the tensile and wedge splitting test results, respectively. The signs of correlation, (+) in green and (-) in red, are specified for each parameter on the graphs. By using this representation tool, one can visualise faster the most correlated parameters with the considered one, and also have an idea about the mean correlation degree of one parameter with all the other ones just by observing the size of the plotted area.

	$\%_{spinel}$	D_{th}	E_{RFDA}	σ_{NT}	${}^{S}G'_{f}$	B'	R_{st}	l'_{ch}	α
$\%_{spinel}$	1								
D_{th}	0.86	1							
E_{RFDA}	-0.84	-1.00	1						
σ_{NT}	-0.86	-1.00	1.00	1					
${}^{S}G'_{f}$	0.10	0.58	-0.62	-0.59	1				
B'	-0.71	-0.95	0.97	0.96	-0.77	1			
R_{st}	0.92	0.99	-0.98	-0.99	0.46	-0.91	1		
l'_{ch}	0.79	0.99	-0.99	-0.99	0.68	-0.98	0.96	1	
α	-0.98	-0.94	0.93	0.95	-0.30	0.83	-0.98	-0.89	1

Figure IV-22: Correlation matrix obtained from the wedge splitting test results presented in Table IV-1

	$\%_{spinel}$	D_{th}	E_{TT}	σ_{t}	${}^{V}G'_{f}$	B'_{2}	R_{st}	l'_{ch}	α
$\%_{spinel}$	1								
D_{th}	0.86	1							
E_{TT}	-0.80	-0.98	1						
σ_{t}	-0.85	-0.98	0.99	1					
${}^{V}G'_{f}$	0.44	0.74	-0.84	-0.84	1				
B'_{2}	-0.58	-0.83	0.92	0.92	-0.99	1			
R_{st}	0.96	0.98	-0.96	-0.96	0.67	-0.78	1		
l'_{ch}	0.36	0.65	-0.78	-0.78	0.99	-0.96	0.59	1	
α	-0.98	-0.94	0.90	0.94	-0.60	0.72	-1.00	-0.52	1

Figure IV-23: Correlation matrix obtained from the tensile test results presented in Table IV-1

First, from all the graphs (from Figure IV-24a to Figure IV-24f), one can observe that two main categories of parameters, with opposite dependences, can be distinguished:

- Spinel content ($\%_{spinel}$), thermal damage (D_{th}), fracture energy (${}^{S}G'_{f}$ and ${}^{V}G'_{f}$) and ability to sustain thermal shocks (R_{st} and l'_{ch})
- Brittleness (B' and B'_{2}), Young's modulus (E_{RFDA} and E_{TT}), tensile strengths (σ_{NT} and σ_{t}) and thermal expansion (α).

These two opposite categories seem to be physically coherent since, for example, the increase of thermal shock resistance implies the increase of spinel content, thermal damage and fracture energy, and the decrease of brittleness, Young's modulus, tensile strength and thermal expansion coefficient.

Secondly, it can be observed that the shapes of the correlation areas are globally the same for all the parameters, except, perhaps, for l'_{ch}.

Anyway, one of the main information provided here is that the considered parameters are much more correlated with the thermal damage parameter (D_{th}) than the spinel content, as it could be expected regarding the previous experimental results obtained in paragraph III.3.2.. Moreover, it appears that D_{th} (see Figure IV-24b) is very correlated with the parameters linked to the ability to resist to thermal shocks, especially with R_{st} for both techniques, and l'_{ch} for the wedge splitting test.

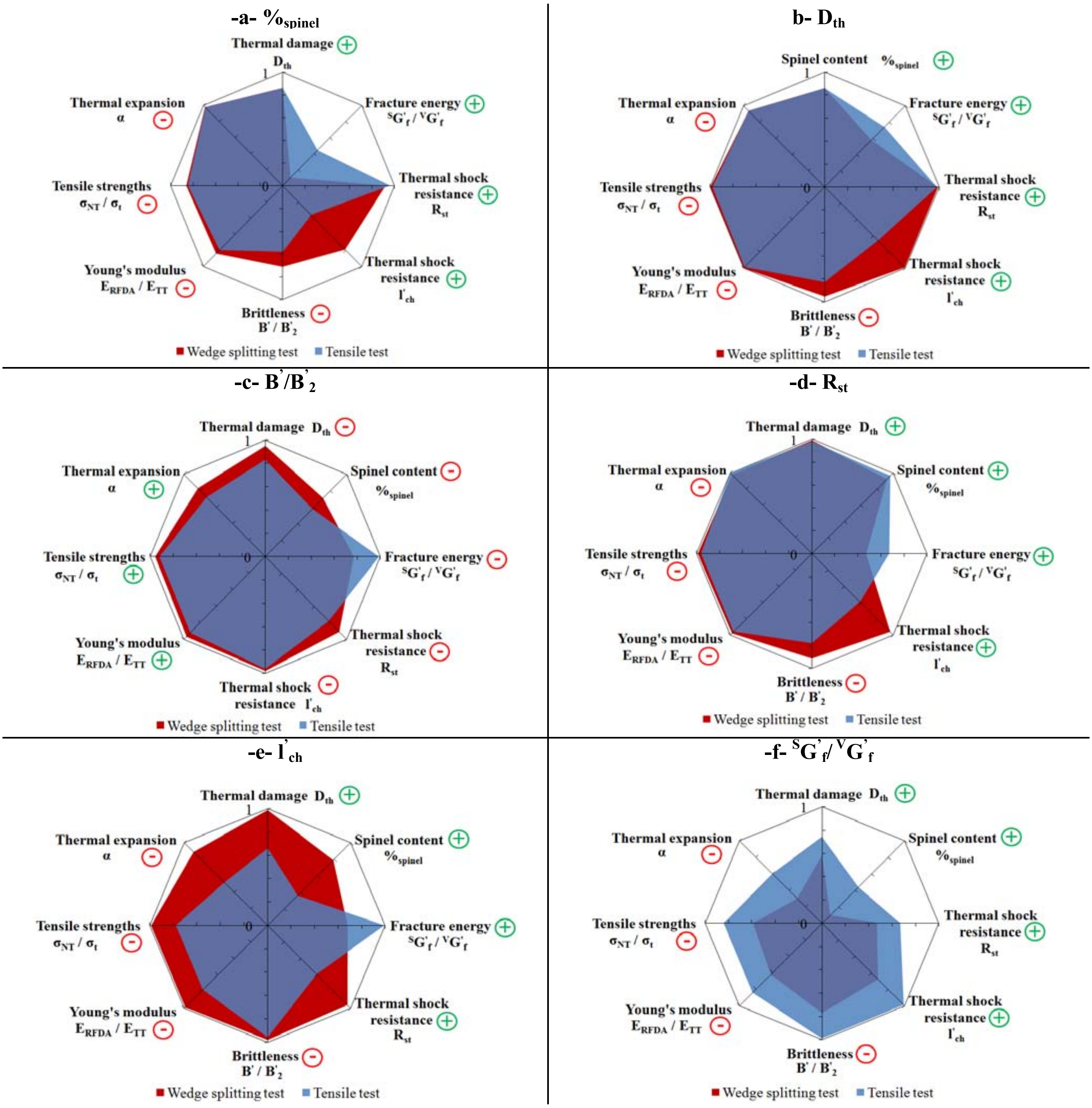

Figure IV-24: Correlation analysis for spinel content (a), thermal damage (b), brittleness (c), ability to sustain thermal shocks (d and e) and fracture energy (f) with radar representations

IV. Conclusion

This chapter aimed at studying experimentally the influence of the thermal damage that occurred during the cooling stage of the process on the mechanical behaviour of the composites.

The first part consisted in highlighting the thermal damage occurrence (within magnesia-spinel composites) through high temperature techniques, and quantifying it at room temperature. The Hashin and Shtrikman model was applied as a reference to quantify the thermal damage pre-existing within the microstructure of those two-phase materials. Indeed, by calculation of a Kachanov type parameter, the influence of the spinel content on thermal damage could be estimated. Moreover, the comparison of the Young's modulus at high temperature (beginning of cooling) with the values predicted by this model allowed to show that microcracks initially present in these materials are not fully closed at the maximum temperature of the thermal cycle.

As expected, the studied magnesia/spinel composites exhibited, with both tensile and wedge splitting tests, non-linear mechanical behaviour under tension up to the peak, high strain-to-rupture values compared to the pure magnesia material and significant post-peak regions. Moreover, during tensile tests, residual strain was observed when unloading. The considered spinel content range allowed to modulate the damage rate, present as a diffuse microcracks network, in order to analyse the influence of this thermal damage on the mechanical damage growth within the composites (non-linearity) when loaded. Thus, it was observed that the increase of spinel content has a real influence on the non-linearity of the mechanical behaviour and that the increase of thermal damage highly decreases the tensile strength and the brittleness, and increases the fracture energy and the thermal shock resistance parameters. In addition, a complementary correlation analysis allowed to quantify the correlation degree between the most relevant parameters and, also, to quantify the thermal damage influence on the mechanical parameters and, more specifically, on thermal shock resistance. The subsequent numerical investigation (Chapter V) will focus on the whole transition from thermal damage to the non-linear mechanical behaviour of magnesia-spinel materials.

Chapter V. Micromechanical modelling of magnesia-spinel refractories: from thermal damage due to thermal expansion mismatch to non-linear mechanical behaviour

I. Preliminary considerations

I.1. Microstructure design of magnesia-spinel composites

Since the elaborated magnesia-spinel composites are supposed to be isotropic in both stiffness and thermal expansion, the modelled composites have to be isotropic, or quasi-isotropic. Nevertheless, the simulation of damage will highly increase the calculation time, as well as the required resources (e.g. RAM). That is why rather simple geometries with a small number of inclusions are required. The subsequent problem is that the reduction of the number of inclusions may irremediably increase the anisotropy of the cell, which must be avoided. This was the main subject of Chapter III which concluded that F.C.C. and H.C.P. cells, combined with periodic conditions, allow to provide quasi-isotropic properties and, therefore, could be considered to represent the microstructure of magnesia-spinel composites. Thus, in the present chapter, a F.C.C. periodic cell (Figure V-1) is considered as the quasi-isotropic periodic Representative Volume Element depicting the microstructure design of the magnesia-spinel composites.

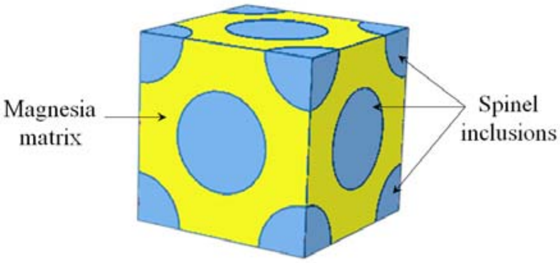

Figure V-1: Quasi-isotropic periodic cell (Face Centred Cubic arrangement) considered for the microstructure design of magnesia-spinel composites

The significant difference of mechanical behaviour between the two constituents, magnesia matrix and spinel inclusions, has been shown in Chapter IV and taken into account in the numerical model. Then, in the later, the mechanical behaviour of the spinel inclusions has been considered as linear elastic and the one of the magnesia matrix has been considered as a damage elastic one (with a post-peak region) in order to well depict damage progression resulting from both temperature variation and mechanical loading. An anisotropic damage model, available in Code Aster and used here to represent well the behaviour of the matrix, is presented in the following paragraph.

I.2. Modelling of the magnesia matrix mechanical behaviour by an anisotropic damage model

I.2.1. Interest of anisotropic continuum damage models

Despite the existence of different anisotropic continuum damage models, isotropic models are still used exclusively in companies in order to represent the behaviour of concrete structures. This is due to the complexity of implementation of such anisotropic models, but also the difficulty of parameters identification, the difficulty of coupling such model with other physical phenomena (creep, plasticity), and, most of the cases, the needed calculation time which can be very long. Therefore, when one wants to simulate a mechanical behaviour, it is very important to wonder if an isotropic model could be satisfying. In the present work, radial microcracks (oriented damage) are expected to occur around the spinel inclusions during cooling. Thus, considering isotropic damage around the inclusions cannot represent well the reality and may provide inaccurate macro-mechanical behaviour. Recently, Sands et al. [SAN-07] proposed a constitutive model, for two-phase materials with thermal expansion mismatch, in which damage is recorded as a damage orientation function held numerically at several orientations.

Most of the existing anisotropic damage models concern strain-based formulation because damage is mainly a strain-controlled phenomenon. According to [CHA-92], a consistent damage model, applied to quasi-brittle materials, has to ensure:

- continuity of stress-strain relation,
- coherent thermodynamic framework,
- asymmetry between tension and compression (strength and softening),
- closure of cracks included in the unilateral properties,
- damage memory in specific direction: the isotropic elastic behaviour of an element becomes anisotropic after damage.

The problem is that most of the anisotropic damage models [CHA-93, HAL-96, FIC-97, DUB-03, MUR-97, CHA-05] do not satisfy all these conditions [CHA-92, COR-02].

More recently, Godard and Badel [GOD-05, BAD-07] proposed a very interesting model which was implemented in the Code Aster. This damage model allows to depict damage without introducing any residual strain (no irreversible strain), and only in the stressed directions (damage anisotropy) when submitted to tension. In order not to depend on the mesh, a regularisation method (strain gradient method) is coupled with this model.

I.2.2. Orthotropic damage model from Code Aster with regularisation method

I.2.2.1. Presentation of the model

The objective of the model developed by [GOD-05, BAD-07] was to dispose of a simple anisotropic model with a rather low number of parameters. Since all phenomena observed experimentally could not be taken into account, specifications were fixed before the development of this model. More details are given in [GOD-05, BAD-07]. The anisotropy induced by concrete damage and the unilateral effects can be described by defining several parameters. These parameters are the following ones:

- α: coupling constant between the damage evolution in tension and the damage evolution in compression. This constant is between 0 and 1, rather close to 1. The default value is 0.9.
- k_0: constant part of the threshold function allowing to calibrate the height of the peak in tension.
- k_1: parameter of the threshold function allowing to increase the compression threshold.
- k_2: control parameter of the shape of the failure envelope for biaxial tests. The default value is $7 \cdot 10^{-4}$.
- γ_B: term of the “blocked” energy (equivalent to an energy of strain hardening) relative to the damage evolution in tension. This parameter allows to control the shape of the peak in tension.
- γ_d: term of the “blocked” energy (equivalent to an energy of strain hardening) relative to the damage evolution in compression. This parameter allows to control the shape of the peak in compression.

As a remark, the control of the peak in tension and the peak in compression is obtained by finding appropriate k_0/γ_B and k_1/γ_d couples, respectively, which allow to fit with the experimental stress-strain curves in tension and in compression. Moreover, the Young's modulus and the Poisson's ratio have to be specified too.

Otherwise, since this damage model is orthotropic in tension and isotropic in compression, the tensile and compressive damages can be represented by a tensor (Figure V-2) and a scalar, respectively. Therefore, six different tensile damage variables (D_1, D_2, D_3, D_4, D_5 and D_6) and one compressive damage variable (D_7) can be observed in post-processing.

$$\left(D_{tension}\right)=\begin{pmatrix} D_1 & D_4 & D_5 \\ D_4 & D_2 & D_6 \\ D_5 & D_6 & D_3 \end{pmatrix}$$

Figure V-2: Tensile damage tensor considered with the anisotropic damage model

I.2.2.2. Main features of the model when loaded in tension and in compression

In order to understand better the mechanical behaviour of this specific damage model and to check the meaning of the different parameters, five different mechanical tests, based on tension and compression, have been simulated on a 3D-element. These simulated tests have been managed with imposed displacements.

The first mechanical test, shown in Figure V-3, consists in applying, in one direction (the 3-direction), different loading/unloading cycles in tension. According to the obtained stress-strain curve, there is a memory of damage in the material since, after a loading/unloading cycle, the slope of the stress-strain curve (stiffness), when re-loading, is the same as the slope of the previous unloading step. Moreover, according to Figure V-3, no residual strain is observed after the different loading/unloading cycles, which is characteristic of pure damage elasticity. In addition, the curve is not totally linear before reaching the maximum stress because strain softening before the peak is also taken into account in the model.

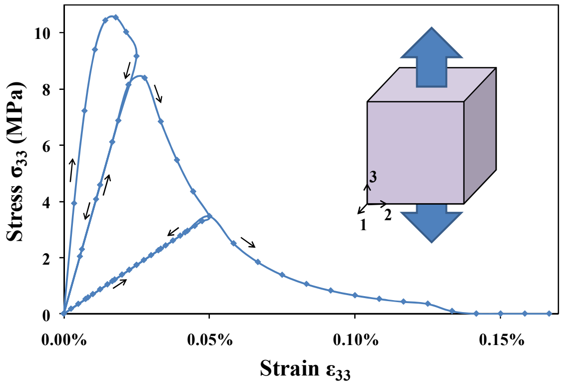

Figure V-3: Simulated tensile test on one element in the 3-direction

The second mechanical test, presented in Figure V-4, consists in applying three different successive tensile tests in different directions. More precisely, the steps 1 and 2 (Figure V-4a) correspond to a loading/unloading cycle in tension in the 3-direction, the steps 3 and 4 (Figure V-4b) correspond to a loading/unloading cycle in tension in the 2-direction, and, finally, the step 5 (Figure V-4c) is a loading step in tension in the 3-direction. According to the stress-strain curve shown in Figure V-4a, during the first tensile test in the 3-direction, the stiffness is reduced in this direction. Then, when applying a tensile test in the 2-direction (Figure V-4b), it appears that the stiffness in this direction is the same as the one at the beginning of the first test (when no damage is present). Thus, the anisotropy of this model in tension is, here, obvious. Moreover, there is still damage memory in the 3-direction (Figure V-4c) even after the loading/unloading cycle in the 2-direction.

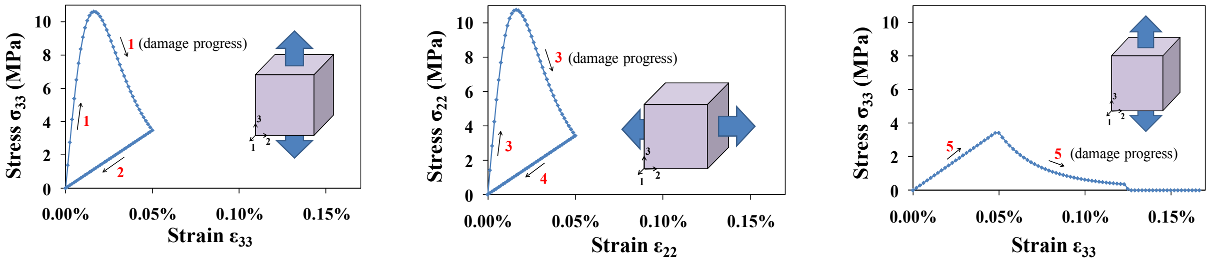

-a- -b- -c-

Figure V-4: Simulated tensile tests on one element in different directions

The third mechanical test, shown in Figure V-5, is composed of successive loading/unloading cycles in compression in only one direction (the 3-direction). According to the obtained stress-strain curve, there is, like in tension, damage memory (regarding the slopes), no residual strain when unloading, and strain softening before reaching the maximum stress.

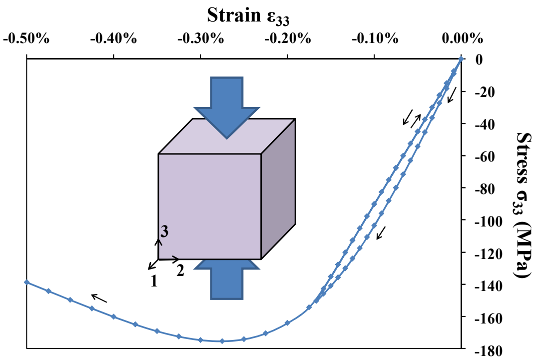

Figure V-5: Simulated compressive test on one element in the 3-direction

The fourth mechanical test, presented in Figure V-6, consists in applying two different successive compressive tests in different directions. More precisely, the steps 1 and 2 correspond to a loading/unloading cycle in compression in the 3-direction and the step 3 corresponds to a loading step in compression in the 2-direction. The stress-strain curves obtained in the 3-direction (blue curve) and in the 2-direction (red curve) are superimposed for the steps 2 and 3. Then, when applying a compression test in the 2-direction (red curve), it appears that the stiffness is the same as the one at the end of the first test (in another direction), which means that damage appears not only in the stressed direction but also in the other directions, confirming the isotropy of this model in compression.

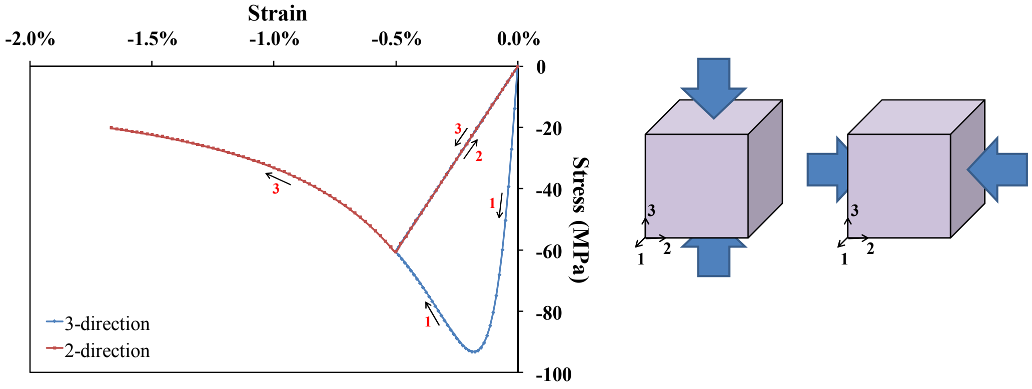

Figure V-6: Simulated compressive tests on one element in different directions

The last mechanical test, presented in Figure V-7, consists in applying successive tensile and compressive tests in the same direction (the 3-direction). More precisely, the steps 1 and 2 correspond to a loading/unloading cycle in tension, the steps 3 and 4 correspond a loading/unloading cycle in compression, and, finally, the step 5 is a loading step in tension. According to the obtained stress-strain curve, it appears, first, that compression (at low level) leads to crack closure. Indeed, the slope of the curve in compression (step 3) is the same as the initial slope (initial stiffness) before tension (step 1). Moreover, it can be pointed out that cracks obtained in tension can get closed in compression, but damage memory is still observable when reloading in tension (step 5). It means that microcracks do not vanish when closed in compression, which is physically realistic.

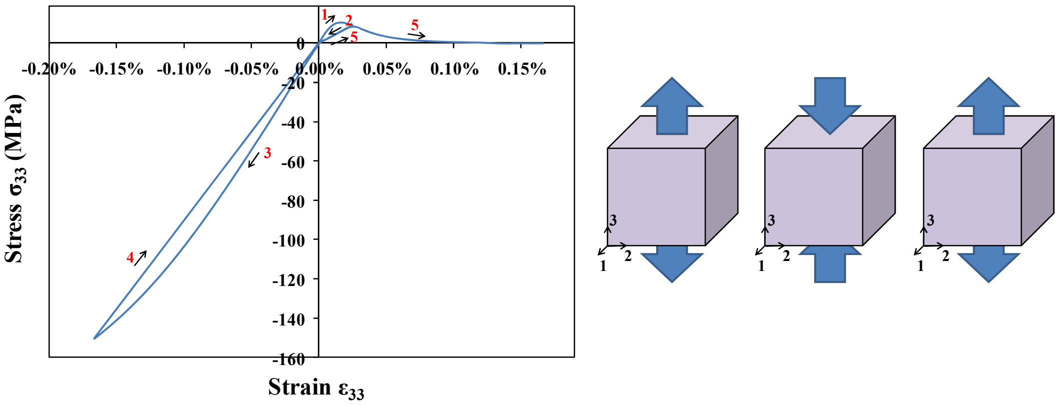

Figure V-7: Simulated tensile and compressive tests on one element in the 3-direction

Otherwise, as already mentioned in Chapter I (paragraph III.4.), in such continuum damage models, problems of damage localisation in one element are usually observed, entailing a high mesh dependency. To overcome that, regularisation methods are often used. Here, a strain gradient method [GOD-05], based on the work of Peerlings et al. [PEE-95], has been chosen in order to delocalise the behaviour law by regularisation of the local strain ε. Indeed, from the local strain tensor ε, calculated for all the nodes independently, a mean, or regularised, strain tensor $\bar{\varepsilon}$ is determined for the nodes located on the quadratic elements vertices (Figure V-8), by taking into account its neighbourhood.

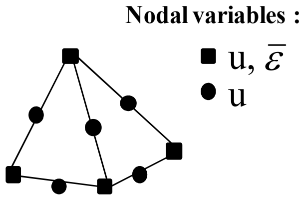

Figure V-8: Tetragonal element (quadratic order) with regularised strain calculated at its vertices

This considered neighbourhood depends on a characteristic length which has to be specified in the model (estimated by the user). Even if they have the same name, this numerical characteristic length is totally different from the experimental characteristic length presented in Chapter IV. After determining the regularised strain tensor $\bar{\varepsilon}$ (Step 1 in Figure V-9a), the damage variables (tensor in tension and scalar in compression) are, then, calculated from this tensor (Step 2 in Figure V-9a). An important remark is the following one: the stress tensor is, then, obtained from these damage variables (deduced from $\bar{\varepsilon}$) and the local strain tensor ε (not $\bar{\varepsilon}$!), as indicated by the dotted line in Figure V-9a (Step 3). Indeed, the use of regularised strains in the calculation of the stresses would “regularise too much” the problem, entailing questions on the solutions existence [AST-10].

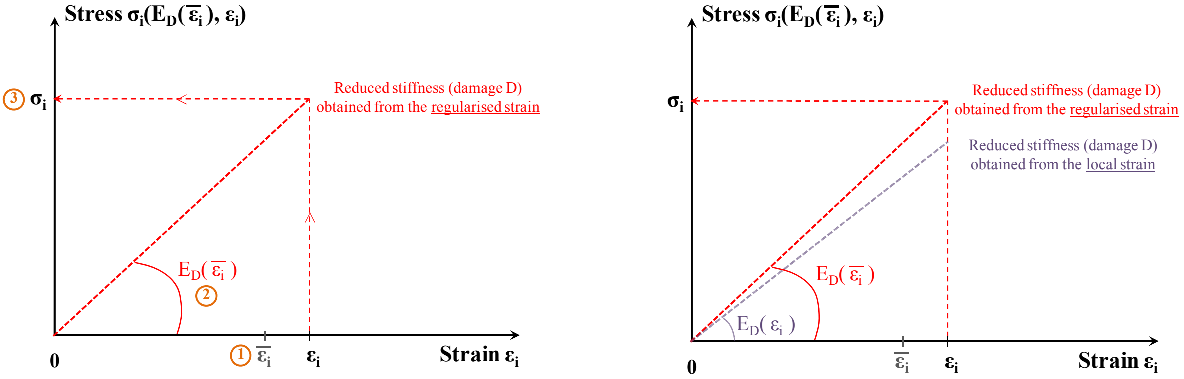

-a- -b-

Figure V-9: (a) Scheme explaining how the stresses are calculated when using the considered regularisation method and (b) associated possible problem of stress value overestimation.

In other words, the fact that the stresses are calculated from damage (depending on $\bar{\varepsilon}$) and the local strains ε can be responsible for overestimated stress values, as presented in Figure V-9b. Indeed, according to this figure, with regularisation of the strains, the damage may be lower than without regularisation, and therefore, the stiffness higher, which logically induces higher stresses. Moreover, since $\bar{\varepsilon}$ is calculated from the characteristic length specified in the model, this length will directly act on this overestimation phenomenon. The optimisation of its value is here very difficult since very time consuming.

To sum up, a regularisation (or delocalisation) method is needed here to overcome the problem of mesh dependency. But, although the strain gradient method used allows to reach this goal, it is not perfect since, in post-treatment, the stress values may be overestimated according to the specified characteristic length. Thus, the more reliable results to consider will be the damage and strain values.

After this brief presentation of the anisotropic model chosen in Code Aster to represent the behaviour of the magnesia matrix, the next part will be devoted to the model parameter adjustment from experimental results.

II. Simulation of a wedge splitting test to adjust the parameters of the anisotropic damage model for the magnesia matrix and illustrate the relevance of using this model

Since the anisotropic damage model is supposed to be assigned to the magnesia matrix, the easiest way to adjust the model parameters should be to apply tension and compression tests on one element, as just done in the previous paragraph. Nevertheless, as mentioned in Chapter IV, tensile tests on pure magnesia samples, especially, have not permitted to get satisfactory results since the overall stress-strain curves could not be obtained and the peak had to be assumed especially. Therefore, the adjustment of the model parameters has been preferentially done from experimental results obtained by wedge splitting tests. Moreover, in addition to identify the model parameters, the simulation of a wedge splitting test could also allow to visualise the stress field involved within the sample during a wedge splitting test and estimate the local damage parameters progression.

II.1. Considered 3D model

Simulation of damage during a wedge splitting test may require significant calculation resources. In order to reduce this demand, and according to the symmetry of a wedge splitting test sample, the 3D geometry considered here is one quarter of the sample (Figure V-10). Moreover, in order to represent physically the load transmission piece (in alumina) and facilitate simulations, a parallelepiped has been introduced in the model (green part in Figure V-11). The real wedge geometry of the transmission piece is not considered here and this piece is supposed to be elastic and with a Young's modulus very much higher than the one of the magnesia sample.

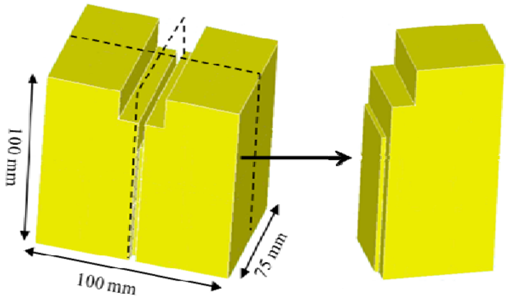

Figure V-10: Simplification of the 3D wedge splitting test geometry by symmetry (one quarter)

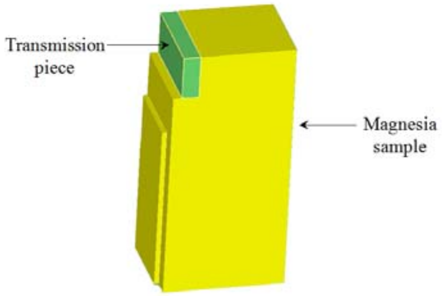

Figure V-11: Consideration of a transmission piece in the model (real geometry not considered here)

The meshing of the whole geometry (Figure V-12a and Figure V-12b), has been realized by paying attention on the zone on interest, namely the face where the crack propagation is expected to occur. Hexahedral elements with quadratic geometric order (20 nodes per element) where chosen

(Figure V-12c). The mesh of the whole model (Figure V-12a and Figure V-12b together) is constituted of 5646 elements and 25940 nodes.


-a- -b- -c-

Figure V-12: Meshes of the magnesia sample (a) and the load transmission piece (b) composed of hexahedral quadratic elements (c)

The boundary conditions of the model have been chosen so that the experimental conditions and the symmetry of the 3D geometry might be respected. These boundary conditions are represented in Figure V-13a. Concerning the load conditions (Figure V-13b), an horizontal displacement is imposed in the x-direction, equal to δ/2 (with δ: displacement considered in the experimental force-displacement curve), and the resulting horizontal force F_H (in the x-direction) is calculated during a post-processing step from the volume average of the stress σ_{xx} in the first layer of elements within the transmission piece in contact (surface S) with the sample.

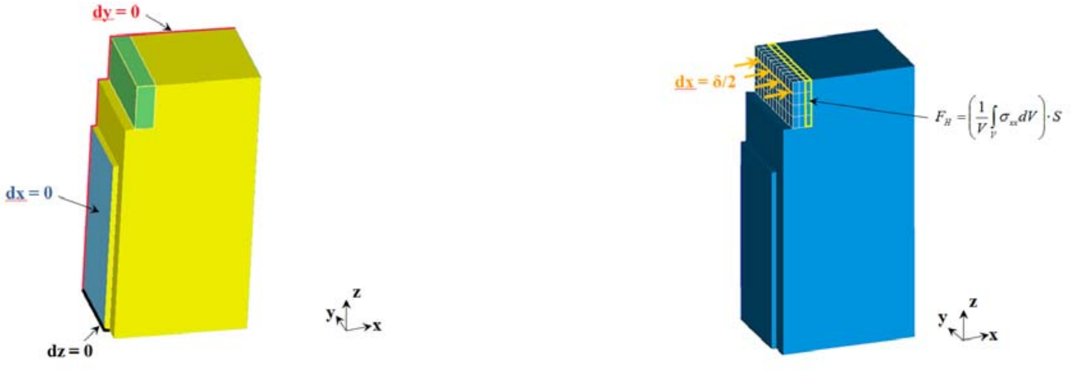

-a- -b-

Figure V-13: (a) Boundary conditions - (b) Load conditions (displacement imposed on the transmission piece) and calculation of the force during a post-processing step

II.2. Simulated results

II.2.1. Values of the adjusted parameters

Different simulations were performed in order to find the suitable model parameters (presented in paragraph I.2.2.1.) allowing to get a simulated force-displacement curve in agreement with the one obtained experimentally on pure magnesia. For two parameters, the default values were kept. Indeed, the coupling constant α between the damage evolutions in tension and in compression, and the control parameter k_2 of the shape of the failure envelope for biaxial tests were fixed to 0.9 and $7 \cdot 10^{-4}$, respectively. Thus, only four parameters had to be adjusted, namely k_0 and γ_B, for tension, and k_1 and γ_D, for compression. It must be reminded that the control of the height and thickness of the peaks, either in tension or in compression, is obtained by the combination of the two corresponding parameters (k_0 and γ_B ; k_1 and γ_D). The first trials have consisted in considering the assumed curve obtained by tensile test on magnesia (even if underestimated), assuming the compressive strength (σ_c) to be much higher than the tensile one (σ_t) (typically $\sigma_t = 0.06 \cdot \sigma_c$) and simulating uniaxial tensile and compressive tests, as done in paragraph I.2.2.2.. When the parameters were considered rather satisfactory, the second step consisted in optimising these parameters from the simulation of a wedge splitting test, for which accurate and reproducible experimental results were obtained on pure magnesia. Finally, the parameters which have been validated are the following ones:

$$\begin{cases} k_0 = 159\,Pa \\ \gamma_B = 4.0 * 10^3 \; J/m^3 \\ k_1 = 40.0 * 10^6 \; Pa \\ \gamma_d = 6.0 * 10^5 \; J/m^3 \end{cases}$$

As a remark, the regularisation method (strain gradient method) was also used in these simulations. For that, the characteristic length was chosen to be equal to about three times the minimum element size (elements located where the crack is expected to occur), and also equal to three times the maximum aggregate size, as it is sometimes advised in literature [BAZ-89]. In the present case, this length corresponds to 9 mm.

Thus, the simulated force-displacement curve, finally obtained, is shown in Figure V-14 and compared with the experimental one obtained on pure magnesia. It appears that the simulated curve exhibits a rather overestimated maximum force value compared to the experimental one, but the evolutions after the peak seem to be very similar. It can be pointed out that this kind of simulations was rather calculation time consuming. Therefore, the parameters could not be optimised in a deeper way.

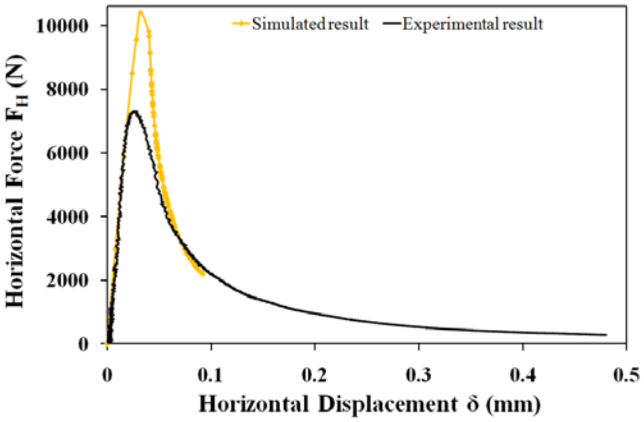

Figure V-14: Comparison of the simulated force-displacement curve with the experimental one

II.2.2. Visualisation of the damage anisotropy and the induced damage zone

First of all, by considering one arbitrary moment during the previous simulation of the wedge splitting test (Figure V-14), for example the last moment of this simulation, it is possible to visualise the tensile damage in different directions (Figure V-15) and, thus, observe the tensile damage anisotropy induced by this mechanical test. Indeed, as expected, the main tensile damage occurs in the horizontal direction (1-direction). Moreover, it appears that tensile damage, with a lower magnitude, also occurs in the 3-direction (vertical direction), which could be attributed to the additional bending induced by this kind of test. As a remark, isotropic compressive damage which is not presented here, is very low compared to these damage levels in tension.

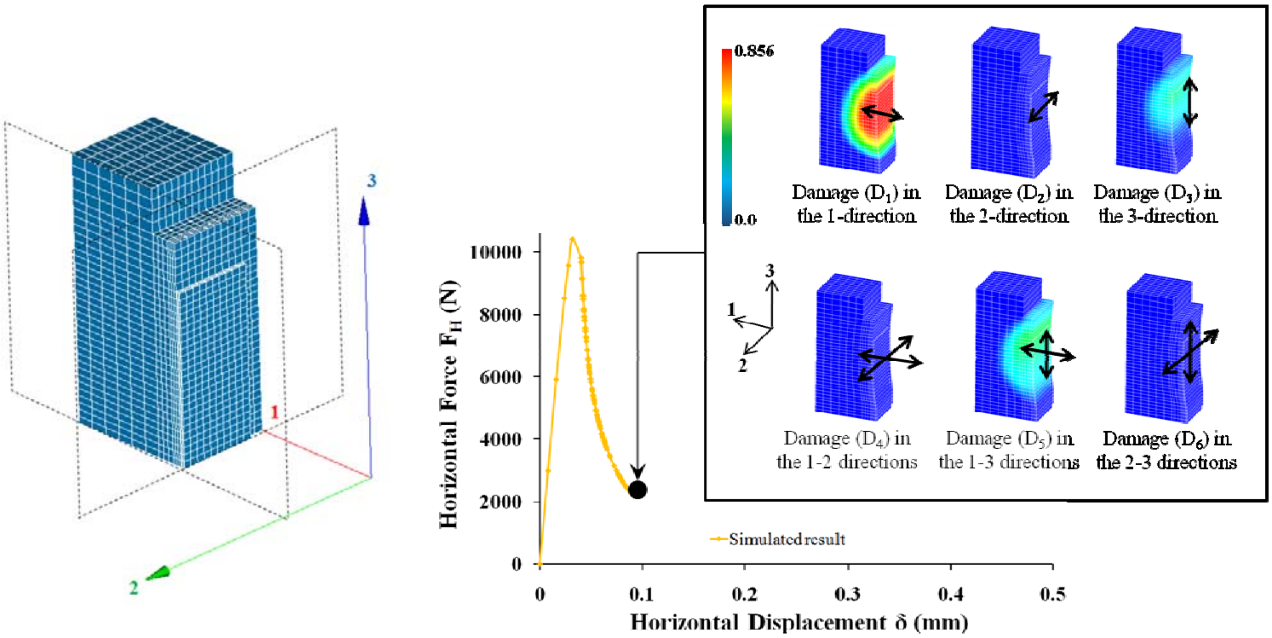

-a- -b-

Figure V-15: (a) Orientation of the sample for the visualisation of damage; (b) Damage variables (D_1 to D_6) in the different directions at a chosen time and visualisation of the damage anisotropy induced by the wedge splitting test

Furthermore, the evolutions of tensile damage in the 1-direction (main direction) and in the 3-direction (damage also present) are shown in Figure V-16. First, as expected, the damage occurs just below the notch and, then, progresses along the middle surface of the sample (the surface on the right side). Nevertheless, this damage is not only located on this surface but also in a rather significant volume around it.

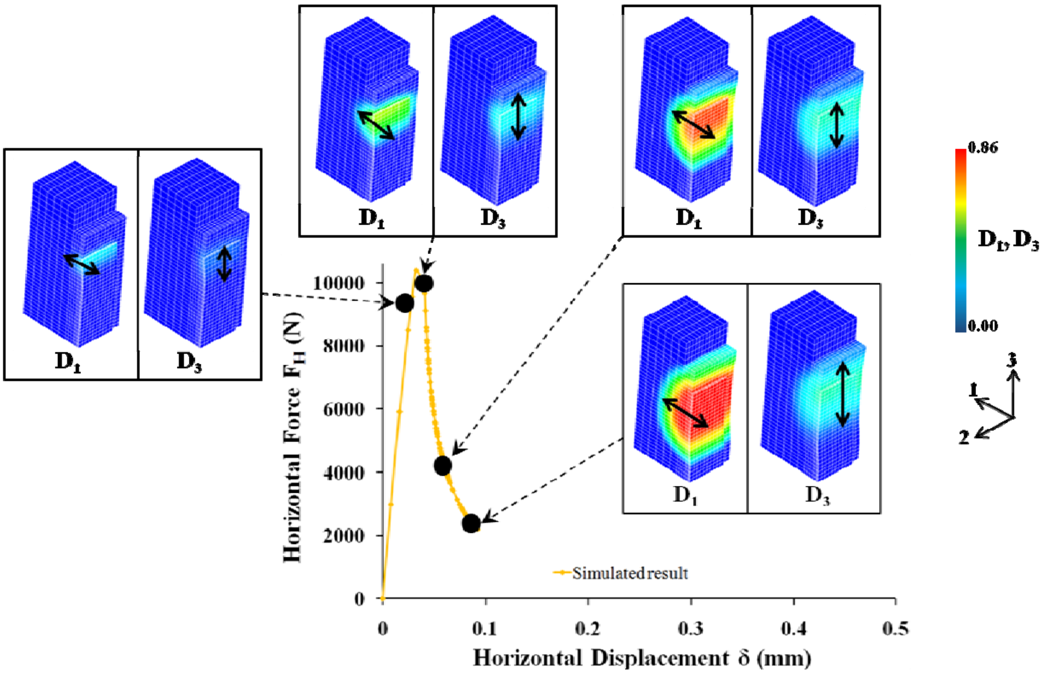

Figure V-16: Evolution of tensile damage (D_1 and D_3) in the 1-direction (main damage) and in the 3-direction during a wedge splitting test

In fact, this evolution seems to be in agreement with previous experimental results (Figure V-17), obtained by acoustic emission [TSC-09] and tomography [HAR-10] (after stopping the test), which showed that the thickness of the damage zone was around 3 cm. Nonetheless, these tests were performed on industrial magnesia-spinel materials and not pure magnesia.

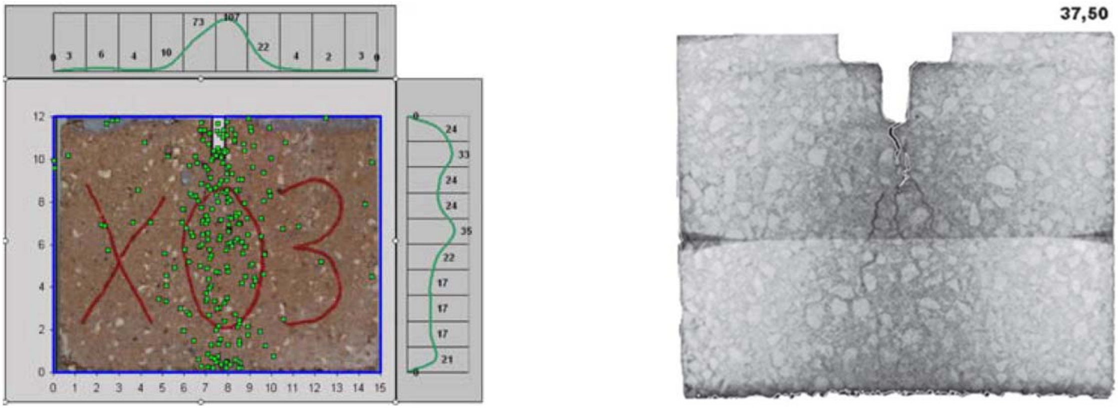

-a- -b-

Figure V-17: Estimation of process zone width by acoustic emission measurements [TSC-09] (a) and tomographic images [HAR-10b] (b) during a wedge splitting test on an industrial magnesia-spinel material

Moreover, looking at the tensile strain field (Figure V-18), it seems that this larger zone might be induced by the macrocrack departure in the corner of the starter notch, which is sometimes observed experimentally. That is why, this 90° angle-corner is sometimes rounded during the machining procedure.

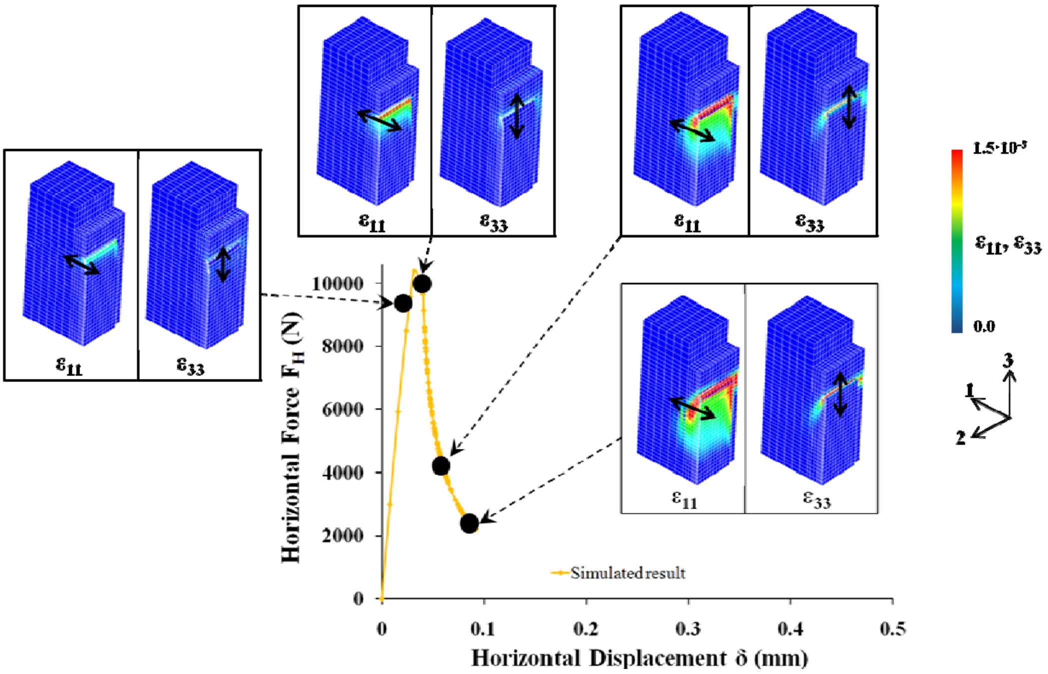

Figure V-18: Evolution of the tensile strains ε_{11} and ε_{33} (positive values) in the 1-direction and in the 3-direction during a wedge splitting test

Another interesting result, obtained in Figure V-19 for the tensile stress field, is that when the macrocrack progresses downwards, the tensile stress field in the crack front does the same but, in the rear of this macrocrack (upwards), stress relaxation is observed. As a remark, since the stresses were overestimated due to the regularisation method used (see the end of paragraph I.2.2.2.), the maximum tensile stress value is, here, arbitrarily fixed to 15 MPa.

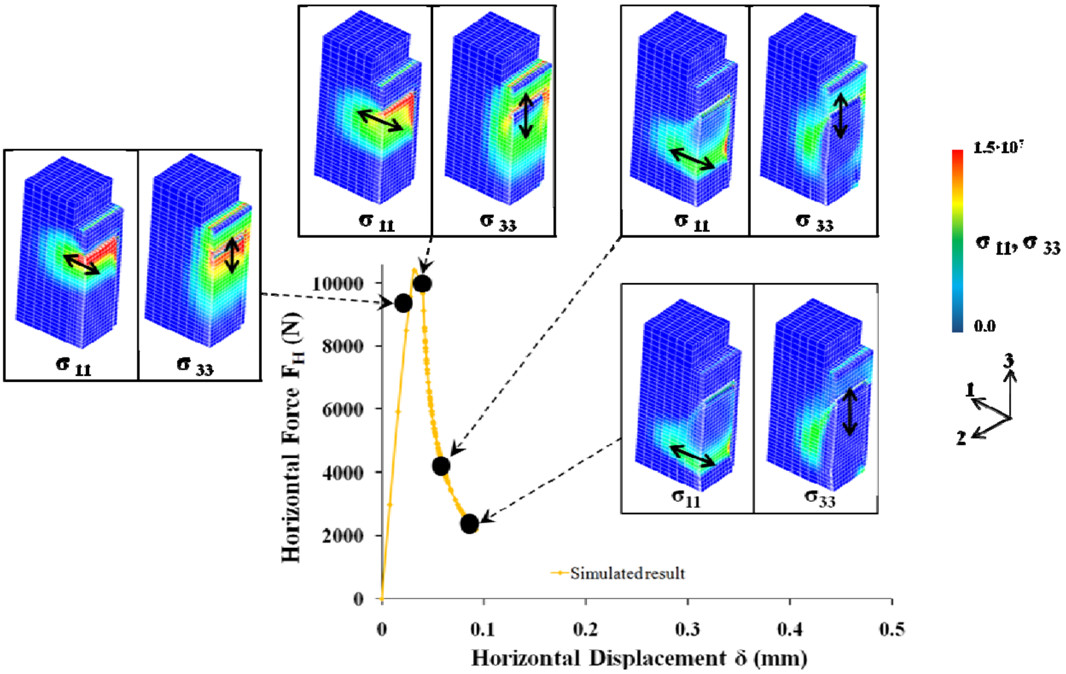

Figure V-19: Evolution of the σ_{11} and σ_{33} tensile stresses (positive values) in the 1-direction and in the 3-direction during a wedge splitting test

These numerical observations are currently being compared with Digital Image Correlation results obtained from experimental wedge splitting tests on pure magnesia and magnesia-spinel composites [BEL-11].

III. Simulation of the thermo-mechanical behaviour of the magnesia-spinel composites

After having proposed suitable model parameters for the magnesia matrix through the simulation of a wedge splitting test, and illustrated the necessity of using this anisotropic model, the present paragraph goes back to the main subject which is the study of the thermo-mechanical behaviour of the magnesia-spinel composites. In the next paragraphs, only simulated results obtained with a 5%-composite will be presented.

The mesh of this composite, presented in Figure V-20, is composed of quadratic tetrahedron elements (10 nodes per element). As a remark, in the special case presented in Figure V-20 (finest mesh used), 19002 periodic relations, between each couple of opposite nodes around the cell, are generated. The considered parameters of the anisotropic damage model are those previously obtained by wedge splitting test. The characteristic length introduced in the regularisation method has been changed depending on the element size.

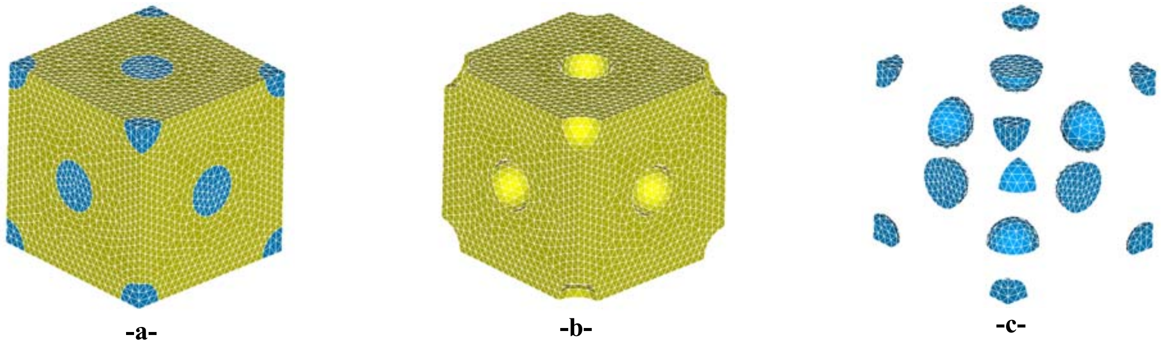

Figure V-20: Meshes of the magnesia-spinel composites (a), the magnesia matrix (b) and the inclusions (c)

III.1. Simulation of the cooling stage of the process

The simulation of the thermal damage phenomenon during the cooling step requires an initial temperature at which the composite can be considered as stress-free. According to the experimental results obtained in Chapter IV, the beginning of the microcracks opening starts at around 950°C when cooled down. Therefore, the initial temperature has been chosen to be 1000°C. Then, the cooling procedure consists in imposing a uniform decreasing temperature on the whole composite. Since the experimental elastic properties (Young's modulus and Poisson's ratio) of the single constituents do not change significantly from room temperature to 1000°C (see Chapter IV), they have been considered in simulations as constant and their values are given in Table V-1. Moreover, according to Chapter IV (Figure IV-6), the thermal expansion coefficients of the two constituents are not constant since they increase with increasing temperature. Nevertheless, the thermal expansion evolutions were supposed to be linear (see the constant CTE values in Table V-1) since the temperature decrease, finally imposed, was rather small ($\Delta T_{max} \approx -180°C$) due to numerical difficulties (calculation resources, mesh fineness and knowledge of the characteristic length). This non-linearity should be taken into account in further works.

	Young's modulus (GPa)	Poisson's ratio	Thermal expansion coefficient (K^{-1})
Magnesia matrix	110	0.17	$15 \cdot 10^{-6}$
Spinel inclusion	210	0.24	$9 \cdot 10^{-6}$

Table V-1: Thermo-elastic properties of the two constituents of the magnesia-spinel composites assumed as constant in the considered temperature ranges

Furthermore, in order to simulate the cooling stage of the process, an important problem had to be solved. Indeed, the damage model chosen for the study, and assigned to the magnesia matrix, does not support temperature dependency. Therefore, it was not possible to associate a thermal expansion behaviour to the matrix ($\alpha=15\cdot10^{-6}\,K^{-1}$). The retained solution was to assign to the elastic spinel inclusions not the real thermal expansion coefficient of spinel ($\alpha=9\cdot10^{-6}\,K^{-1}$) but a coefficient equal to the difference between the coefficients of the two constituents ($\alpha=-6\cdot10^{-6}\,K^{-1}$). Thus, the results of thermal expansion of the composite presented below are obtained after post-treatment of the simulated results by taking into account the thermal expansion coefficient of the matrix.

III.1.1. Visualisation of local radial microcracking

The simulated results, namely stresses, strains and damage, which have been obtained at the end of the considered cooling steps, are presented in Figure V-21 and Figure V-23. Only the results obtained in the magnesia matrix (see the mesh in Figure V-20b) are displayed in order to better visualise the phenomena occurring around the inclusion/matrix interfaces.

Since damage is supposed to be mainly caused by tension (Figure V-22a and b), only the tensile strains and stresses, in the three Cartesian directions, are shown in Figure V-21. This figure shows, first, that the maximum tensile stresses are located near the inclusion/matrix interfaces, and that they are circumferential (see the arrows), as it could be expected according to Figure V-22a.

The simulated results obtained for the damage variables D_1 to D_7 are presented in Figure V-23. Firstly, as expected, no compressive damage (D_7) seems to be present whereas circumferential tensile damage is observed close to the inclusion/matrix interfaces (according to D_1, D_2 and D_3). Therefore, as experimentally expected, during cooling, the circumferential stresses around the inclusions, due to thermal expansion mismatch between the two phases, entail circumferential tensile damage, or, in other words, radial microcracking. Thus, this specific anisotropic damage model allows to depict well the local damage induced by the anisotropic stresses.

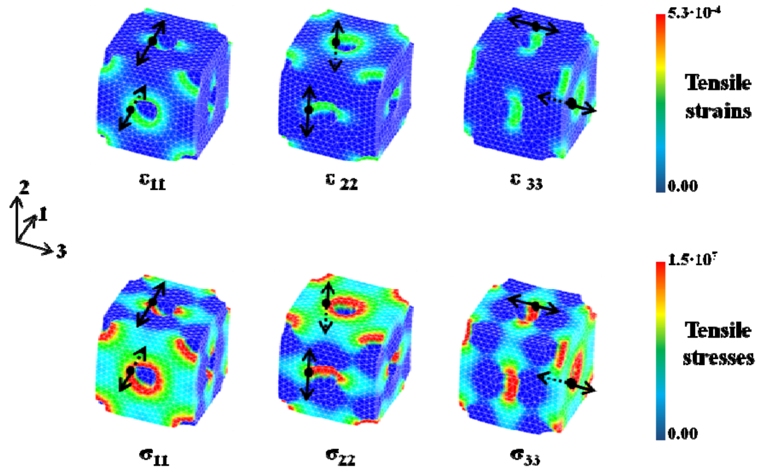

Figure V-21: Visualisation of the anisotropic tensile strains and stresses induced by thermal expansion mismatch during cooling within the magnesia matrix

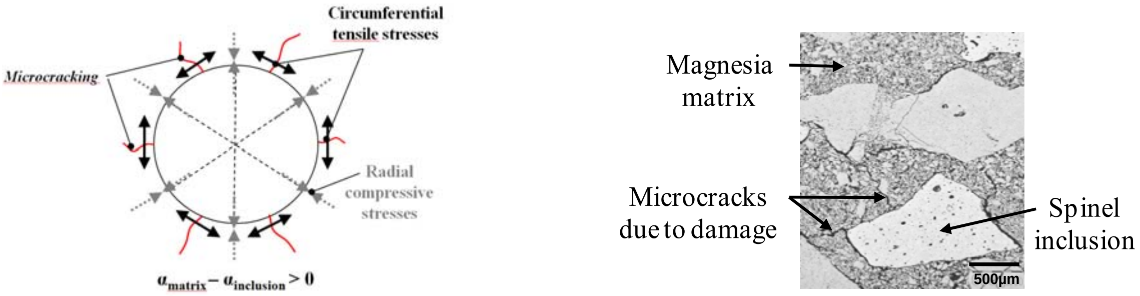

-a-

-b-

Figure V-22: Reminder of the particular theoretical case during cooling (a) supposed to depict the microstructure of the magnesia-spinel composites (b)

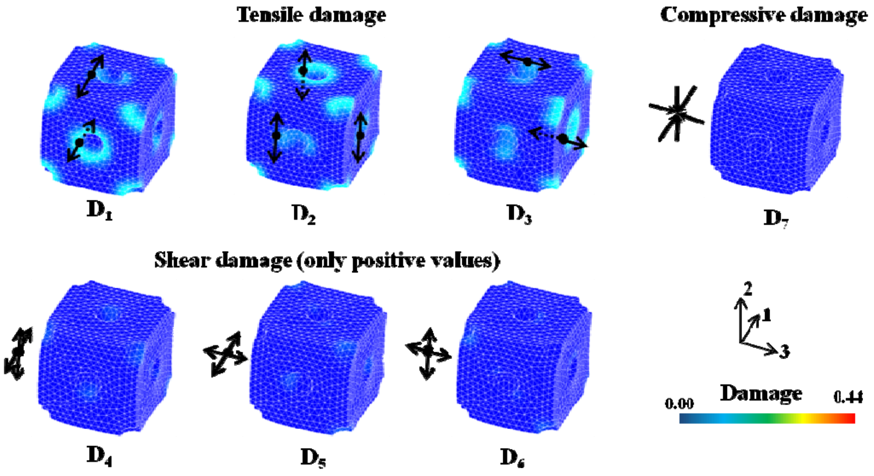

Figure V-23: Visualisation of the anisotropic tensile damage, and isotropic compressive damage, induced by thermal expansion mismatch during cooling within the magnesia matrix

III.1.2. Influence of thermal micro damage on the macro thermal expansion and damage of the composite

After having observed, and validated, in the previous paragraph, the anisotropic character of the thermal micro damage within the microstructure, the influence of this damage on the macro behaviour of the composite, by homogenisation, is studied. As already mentioned at the beginning of paragraph III.1., numerical difficulties (calculation resources, mesh fineness and knowledge of the characteristic length) have only made it possible to simulate small decreases in temperature, the calculations time being, all the same, more than one week. The results of the two different simulations, called Simulation 1 and Simulation 2, are presented here (see simulation parameters in Table V-2). A higher imposed temperature decrease has been possible with Simulation 2, which might come from the finer considered mesh and a higher characteristic length in term of number of elements (normally several elements). In fact, in order to further increase the characteristic length/element size ratio, the mesh should have been finer again, which was, unfortunately, not possible here since the required RAM becomes higher than the available one (48GB).

	Number of quadratic tetragonal elements			**Number of periodic relations**	**Numerical characteristic length**	**Temperature decrease ΔT (°C)**
	Matrix	**Inclusions**	**Total**			
Simulation 1	10757	1288	12045	9708	~1 element	-90
Simulation 2	28108	3094	31202	19002	~2 elements	-180

Table V-2: Presentation of parameters for the two different simulations presented here for the cooling stage of a 5%-magnesia-spinel composite

As a remark, the simulated results have been obtained by non-linear quasi-static simulations which require to introduce a time dependency when defining the load conditions. But, this time is arbitrary and has no influence on the results. It is, here, only used to impose a decreasing uniform temperature field: at one specific time corresponds one specific temperature. Therefore, the time dependency of the following effective parameters has no physical meaning but is needed for the calculations.

Thus, effective macro damage parameters have been determined by calculating the volume average of each damage variable (D_1 to D_7), throughout the cooling step, as follows:

$$\widetilde{D}_i(t) = \langle D_i(t) \rangle_\Omega = \frac{1}{|\Omega|} \int_\Omega D_i(t)\, dV \qquad \text{Eq. V-1}$$

where $\widetilde{D}_i$ and D_i are the homogenised macro damage parameter and the local simulated damage variable, respectively.

The evolutions of both the macro tensile damage parameters ($\widetilde{D}_1$ to $\widetilde{D}_6$) and the macro compressive damage parameter ($\widetilde{D}_7$) versus temperature, obtained with the two different simulations, are shown in Figure V-24a. First, it can be pointed out that the results obtained from Simulation 1 and Simulation 2 are very close. It is observed that the evolutions of the macro damage parameters $\widetilde{D}_4$, $\widetilde{D}_5$ and $\widetilde{D}_6$ (linked to the shear stresses), as well as the macro compressive damage parameter $\widetilde{D}_7$, are very small compared to those of the macro tensile damage parameters $\widetilde{D}_1$, $\widetilde{D}_2$ and $\widetilde{D}_3$. Moreover, it appears that this increasing evolution of tensile damage is rather close to the beginning of the cumulative hits evolution versus temperature experimentally obtained by acoustic emission (Figure V-24b). Otherwise, the evolutions of these three parameters versus temperature could also be compared, in future, with the evolution of the thermal damage parameter D_{th} (introduced in Chapter IV but only at room temperature) versus temperature.

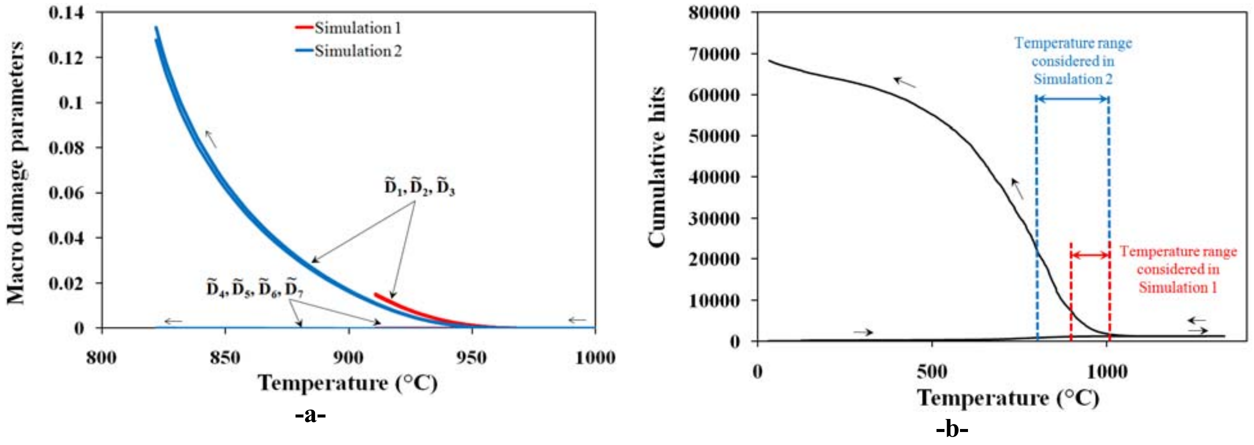

-a-

-b-

Figure V-24: (a) Evolutions of the macro damage parameters in dependence of temperature during the simulated cooling step and (b) high temperature acoustic emission result (cf. Chapter IV), for a 5% magnesia-spinel composite

The influence of the thermal micro damage on the macro thermal expansion evolution of the composite can also be studied. First, since the Face Centred Cubic (F.C.C.) arrangement is isotropic in thermal expansion, the study of thermal expansion is needed in only one of the three directions. Moreover, given that here no external mechanical constraints are present during cooling (free motion), and the periodic conditions make the opposite faces deform in the same way, the effective thermal strain $\tilde{\varepsilon}^{th}$ can be deduced from the normal displacement variation $\Delta\tilde{L}$ between two opposite nodes:

$$\tilde{\varepsilon}^{th}(t) = \frac{\Delta\tilde{L}(t)}{L_0} \qquad \text{Eq. V-2}$$

where L_0 is the initial length of the cubic cell.

Thus, the effective thermal expansion coefficient can be deduced:

$$\tilde{\alpha}(t) = \frac{\Delta\tilde{L}(t)}{L_0 \cdot \Delta T(t)} \qquad \text{Eq. V-3}$$

where ΔT is the imposed temperature difference (negative value for a cooling step).

The evolutions of the effective thermal strain and thermal expansion coefficient versus temperature, obtained with the two different simulations, are presented in Figure V-25a and Figure V-25b, respectively.

First, since the thermal expansion coefficients of the two phases are supposed to be constant in simulations (Table V-1), the thermal expansion coefficient obtained from the HS model is, here, constant (Figure V-25b) and the corresponding thermal expansion evolution is linear (Figure V-25a). According to this figure, the results obtained from Simulation 1 and Simulation 2 appear very close to each other until the end of Simulation 1 and, as expected (see Chapter III), are very near to the HS model at the beginning of cooling, when no damage has occurred. During further cooling (Simulation 2), it appears that the thermal expansion evolution of the composite (Figure V-25a) does not follow the HS model anymore in reason of damage occurrence, inducing a decrease of the thermal expansion coefficient (Figure V-25b). These lower CTE values compared to the hypothetical undamaged evolution (HS model) are in very good agreement with the previous experimental observations (Figure IV-7).

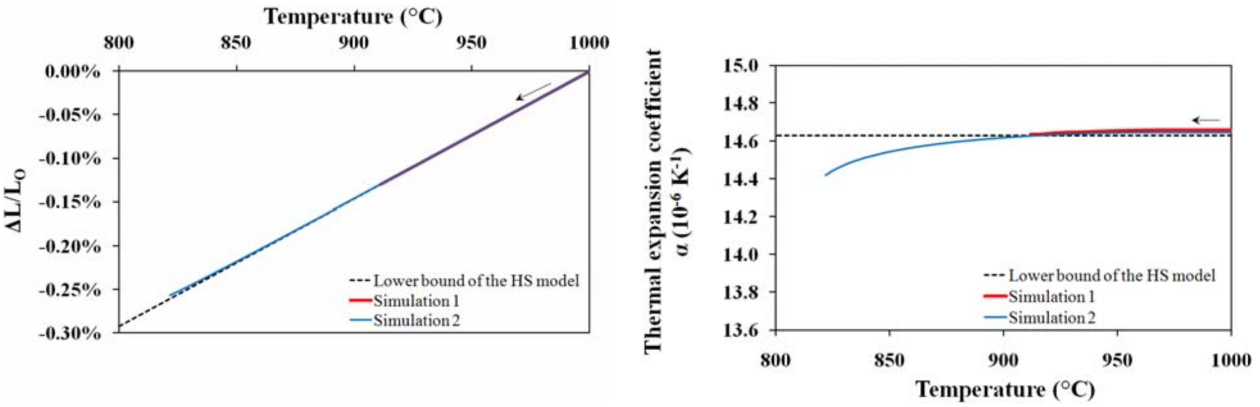

-a- -b-

Figure V-25: Thermal expansion evolution (a) and associated evolution of the thermal expansion coefficient in dependence of temperature (b) during the cooling step; Comparison between the simulated result and the lower bound of the HS model

III.2. Simulation of a tensile test after the cooling step

As already mentioned, the whole cooling process, down to room temperature, could not be simulated. Therefore, the tensile test, simulated after a rather small temperature decrease, cannot be compared with the experimental one performed at room temperature. Nonetheless, the global influence of thermal micro damage, induced by the spinel inclusions addition, can be studied.

Moreover, the simulation of a tensile test after Simulation 2 ($\Delta T \approx -180°C$) was not possible, the composite being probably too thermally damaged. Thus, the simulated tensile test is here obtained after the cooling step of Simulation 1 ($\Delta T \approx -90°C$).

The tensile test is simulated in only one of the three Cartesian directions since the R.V.E. is supposed to be still quasi-isotropic at the end of the cooling step. Indeed, the R.V.E. is quasi-isotropic before cooling (see Chapter III), and, during cooling, the macro thermal damage is quasi-isotropic since $\widetilde{D}_1 = \widetilde{D}_2 = \widetilde{D}_3$ and $\widetilde{D}_4 = \widetilde{D}_5 = \widetilde{D}_6$ (see Figure V-24a). Thus, the simulations of tensile tests in the two other directions would provide the same result.

III.2.1. Visualisation of damage evolution in the microstructure

The simulated tensile and compressive damages, obtained by simulating a mechanical tensile test in the 2-direction (arbitrary direction), are shown in Figure V-26 at one moment during the test. This figure can be compared with Figure V-23 which corresponds to the results at the end of the cooling step, and, consequently, to the beginning of the tensile test. As expected, during this test, the tensile damages in the 1-direction (D_1) and in the 3-direction (D_3) change only in a small extent, remaining nearly the same as those at the end of cooling (Figure V-23), whereas the tensile damage in the 2-direction increases significantly, the higher damage being still near the inclusion-matrix interfaces. Moreover, contrary to Figure V-23, some damage is observed for D_4 (shear in the 1-2 plane) and D_6 (shear in the 2-3 plane) which comes from the high damage in the 2-direction. In addition, there is still quasi no compressive damage (D_7).

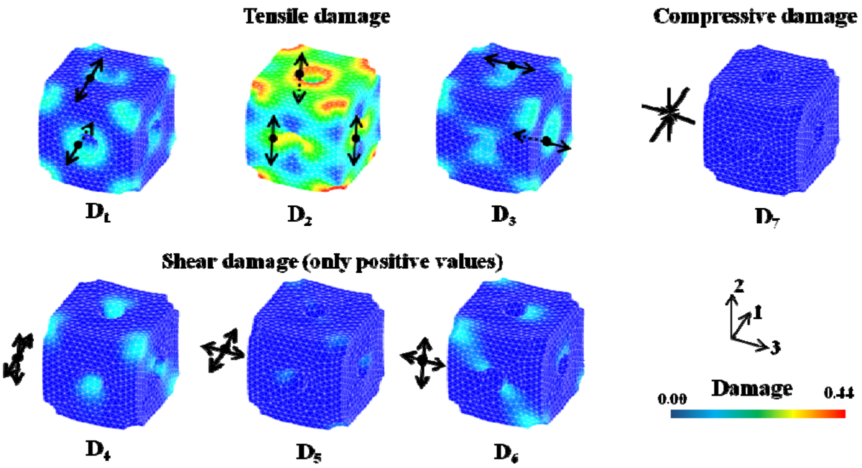

Figure V-26: Visualisation of tensile and compressive damages within the magnesia matrix during a tensile test in the 2-direction

III.2.2. Influence of the micro damage evolution on the macro-mechanical stress-strain behaviour in tension

Similarly to the paragraph III.1.2., effective macro damage, stress and strain are here determined by homogenisation. Furthermore, the reader has to be aware that the time t, considered here, starts at the beginning of the cooling stage and not at the beginning of the mechanical test.

Since the main objective is to obtain the macro stress-strain behaviour from the simulation of a tensile test in the 2-direction, the effective stress and strain tensors are here not totally determined, as it was done in Chapter III. Indeed, only the effective stress $\tilde{\sigma}_{22}$ and strain $\tilde{\varepsilon}_{22}$ are, here, calculated. Thus, in order to begin the macro stress-strain curve at $\tilde{\varepsilon}_{22} = 0$, the macro strain resulting from cooling must be subtracted. Finally, it comes:

$$\tilde{\sigma}_{22}\left(t_{during\ tension}\right) = \frac{1}{|\Omega|}\int_{\Omega} \sigma_{22}(t)\, dV \qquad \text{Eq. V-4}$$

and:

$$\tilde{\varepsilon}_{22}\left(t_{during\ tension}\right)=\frac{\Delta\tilde{u}_2(t)-C}{L_0+C} \qquad \text{Eq. V-5}$$

where $\Delta\tilde{u}_2(t)$ is the macro displacement variation in the 2-direction since the beginning of cooling and during the tensile test, and C is a constant corresponding to the initial macro displacement variation resulting from the cooling step.

The evolution of the macro stress-strain curve of the 5%-composite, calculated in this way, is shown in Figure V-27 in comparison with those initially assigned to the single constituents, namely the spinel inclusions and the magnesia matrix. The most remarkable result is that the introduction of spinel inclusions within a single magnesia material has allowed to increase the non-linearity of the mechanical behaviour in tension, as it was experimentally observed in Chapter IV. As a remark, without considering a preliminary cooling step involving thermal damage, theoretically, the introduction of stiff inclusions within a softer matrix would have finally provide, for the composite, a stress-strain curve above that one of the matrix and with an initial slope (Young's modulus) higher than that one of the matrix. This justifies the necessity of taking this preliminary cooling step into account. Moreover, the tensile strength is also significantly reduced.

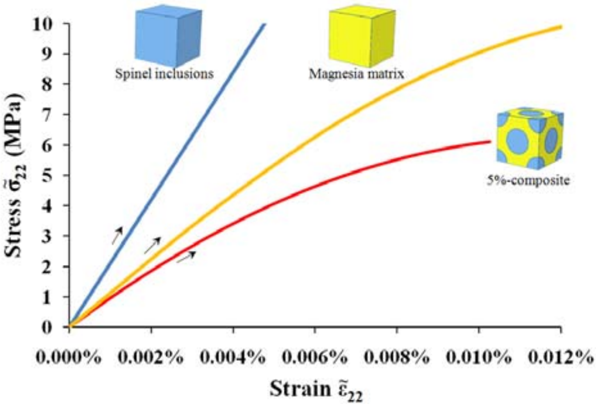

Figure V-27: Macro stress-strain behaviour of the magnesia-spinel composite in comparison with those initially assigned to the single constituents

Now, by focusing only on the mechanical behaviour of the magnesia-spinel composite, loading-unloading steps, experimentally performed, were also taken into account in the simulations. The evolutions of the macro stress and local damage, and the macro damage parameters in dependence of the macro strain are presented in Figure V-28a and Figure V-28b, respectively.

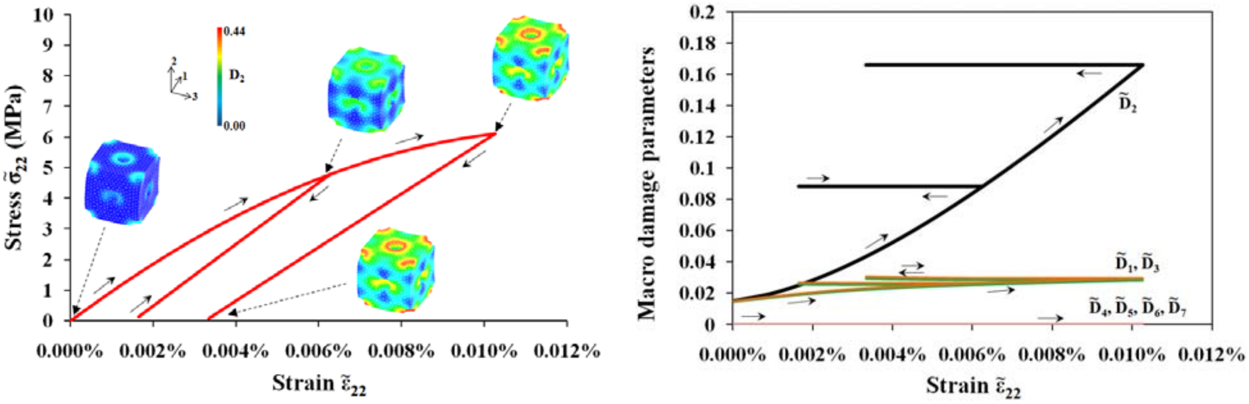

-a- -b-

Figure V-28: Evolutions of the macro stress, and local damage, (a) and the macro damage parameters (b) in dependence of the macro strain after two loading/unloading steps

According to Figure V-28a, an interesting result is that residual strain is observed when unloading, which is not initially included in the damage model used for the matrix and which here comes from the previous cooling stage. This residual strain is also observed on the experimental stress-strain curves of the composites. Moreover, as expected, the slope (Young's modulus) of the curve is lower for the second unloading step than for the first one (due to damage). In Figure V-28a, the local tensile damage evolution in the 2-direction is also exhibited. Before loading, tensile damage is already present within the composite due to the preliminary cooling step. Then, when loading, tensile damage in the 2-direction increases progressively in the whole volume, with a much higher value around the inclusions. More precisely, the main tensile damage in the matrix seems to be located in the equatorial plane of the inclusions. Furthermore, as expected, according to Figure V-28a, the unloading steps do not entail additional damage within the microstructure.

In Figure V-28b, damage at macro-scale is obtained by calculating macro damage parameters in the same way as done during the cooling stage (Eq. V-1). The initial level of macro tensile damage before loading under tension (end of cooling) is the same in the three Cartesian directions: $\widetilde{D}_1 = \widetilde{D}_2 = \widetilde{D}_3$. Then, the simulation of a tensile test in the 2-direction obviously increases the tensile damage ($\widetilde{D}_2$) in this direction. As a remark, macro tensile damage in the 1- and 3-directions ($\widetilde{D}_1$ and $\widetilde{D}_3$) remains quasi-constant (very low increase) during the mechanical test while the other macro damage parameters ($\widetilde{D}_4, \widetilde{D}_5, \widetilde{D}_6$ and $\widetilde{D}_7$) remain close to zero. In addition, as locally observed in Figure V-28a, the unloading steps do not cause additional macro damage within the microstructure.

IV. Conclusion

After having experimentally studied, in Chapter IV, the thermal damage occurrence in magnesia-spinel composites during cooling and its influence on the non-linearity of the macro mechanical behaviour of such materials, this chapter aimed at providing complementary numerical results for a better understanding, and prediction, of the microstructure/property relations, and, of course, validating some of the previous hypotheses regarding the experimental results.

The first part of this chapter has consisted in proposing an anisotropic damage model able to simulate the expected radial microcracking in the magnesia matrix. The potential of this damage model was shown and, afterwards, the adjustment of its parameters for the matrix has been done, through the simulation of a wedge splitting test on a pure magnesia sample.

The second part of this chapter has been focused on the thermo-mechanical behaviour of the magnesia-spinel composites. The design of quasi-isotropic periodic Representative Volume Element for these composites and the use of the anisotropic damage model have allowed to simulate the radial matrix microcracking around the spinel inclusions during the cooling stage of the process, but, up to now, only for a rather small decrease in temperature. Nevertheless, the obtained global evolutions of the macro tensile damage parameters versus temperature (at the beginning of cooling) were in good agreement with the experimental high temperature acoustic emission results, and so did the effective thermal expansion evolution of the composite with the experimental thermal expansion results.

Then, the simulation of a subsequent tensile test, after this cooling step, has allowed to determine the macro stress-strain behaviour of the magnesia-spinel composite. As experimentally observed, this simulated curve exhibited, compared to the one of the magnesia matrix, a lower stiffness (initial slope), a higher non-linearity and a residual strain when unloading.

Concerning the perspectives of this numerical work, some further efforts should be made to better understand the impact of the characteristic length, introduced in the regularisation method, and its relation with the element size of the mesh, in order to find the best way of estimating it. Then, some solutions should be found to simulate the whole cooling stage of the process down to room temperature. By doing that, the simulated macro stress-strain curve could be compared to the experimental one already obtained. Moreover, the evolution of the macro tensile damage parameters during cooling and during a subsequent tensile test should be compared to the evolutions of the experimental thermal D_{th} and mechanical D_{th+mec} parameters, previously introduced. Finally, it might be interesting to consider non-spherical inclusions in the model but the anisotropy of the cell may be, then, increased. Thus, new quasi-isotropic R.V.E. would have to be found, involving probably more inclusions and, therefore, more calculation resources.

Conclusion and perspectives

In addition to their high temperature sustainability, refractory materials, if chosen for the right application, can also exhibit high resistance against both corrosion, multi-axial mechanical loads and severe thermal shocks. The high local thermal stresses induced by thermal shocks can be catastrophic for some installations even if the other required properties are met. The ability to sustain severe thermal shocks is known to be related to the local crack growth resistance mechanisms within the microstructure of such materials, as well as the non-linearity of their stress-strain law. Nevertheless, although experiments by trial and error have provided, over the last decades, a significant industrial knowledge in this field, the way of improving the thermal shock resistance of refractories remains today not fully understood and predictable.

The present thesis aimed at investigating the relationships which exist between the microstructure of refractories and their thermomechanical properties, and especially, at building a better understanding of the microstructural key-points allowing to develop non-linear mechanical behaviour.

From the grain size distribution of industrial magnesia-spinel materials, used in cement rotary kilns, simpler two-phase materials composed of a magnesia matrix and spinel inclusions were elaborated with different spinel contents. The thermal expansion mismatch between spinel and magnesia induces, during cooling, matrix microcracking around the spinel inclusions.

The experimental part allowed, in a first step, to clarify and quantify the thermal damage occurrence during the cooling stage within these magnesia-spinel composites in relation with their spinel inclusions content. In a second step, the fracture behaviour of these materials was investigated at room temperature by two destructive mechanical tests, namely tensile and wedge splitting tests. On composites these two techniques both revealed non-linear mechanical behaviours in tension, high strain-to-rupture values compared to the pure magnesia material and significant post-peak regions. Moreover, during tensile tests, residual strain was observed when unloading. Additionally, the spinel content range, inducing different thermal damage levels, allowed to investigate, in a deeper way, the influence of thermal damage on the fracture behaviour. Indeed, the increase of thermal damage, due to a higher content of spinel inclusions, increases the non-linearity of the mechanical behaviour in tension. Furthermore, it decreases the tensile strength and the brittleness, and increases the fracture energy, as well as the thermal shock resistance parameters. A complementary correlation analysis allowed to quantify the correlation degree between the most relevant parameters and, also, to quantify the thermal damage influence on the mechanical parameters and, more specifically, on thermal shock damage resistance.

The numerical part focused on the whole transition from thermal damage to the non-linear mechanical behaviour of magnesia-spinel materials. More precisely, the main objective was to build a consistent 3D-model able to depict the microcracks occurrence in these magnesia-spinel materials during a uniform temperature decrease from high temperature (stress-free state) to room temperature and able to provide, after this cooling step, a macroscopic non-linear mechanical behaviour.

Since the numerical introduction of damage is known to highly increase the calculation time, the first step of this numerical part consisted in combining Finite Element Periodic Homogenisation (F.E.P.H.) with simple, but quasi-isotropic, Representative Volume Elements (R.V.E), with a small number of inclusions. The choices of periodic Face-Centred Cubic (F.C.C.) and Hexagonal Closed-Packed (H.C.P.) arrangements were validated by considering only non-thermally damaged materials (glass/alumina and glass/pores composites).

The second step consisted in using these quasi-isotropic periodic arrangements with magnesia-spinel composites and adding possible damage in the matrix, the spinel inclusions remaining elastic. To do that, an anisotropic damage model, able to simulate the expected radial microcracking in the magnesia matrix, was proposed. The advantage of using this anisotropic model for the magnesia matrix was illustrated by simulating a wedge splitting test on pure magnesia. Then, the model parameters were adjusted from experimental wedge splitting test results performed on a pure magnesia material. After its parameterisation, this anisotropic damage model was introduced in the matrix of the modelled two-phase periodic composites. Thus, the simulation of a cooling step from 1000°C (only a rather small temperature decrease up to now), allowed to observe, locally, radial matrix microcracking around the spinel inclusions. At macroscopic scale, the global evolutions of effective tensile damage, and effective thermal expansion, versus temperature were in good agreement with the previous experimental results. Finally, by simulating a subsequent tensile test after this cooling step, the macro stress-strain behaviour of the considered magnesia-spinel composite could be obtained. From this result it was concluded, as experimentally observed, that the spinel inclusions addition within the magnesia matrix allowed to increase the non-linearity of the mechanical behaviour, decrease both the stiffness and the tensile strength, and induce residual strain when unloading.

The perspectives of this work could be numerous. First, concerning the experimental part, the use of Digital Image Correlation (D.I.C.) coupled with a mechanical test seems to be an interesting route to investigate the local toughening mechanisms, such as microcracking, crack branching and aggregate bridging, which entail non-linear fracture. These D.I.C. images could also be compared with simulated wedge splitting test results obtained on magnesia and magnesia-spinel composites.

Concerning the numerical part, some further efforts should be made to better understand the impact of the characteristic length, introduced in the regularisation method, and its relation with the element size of the mesh, in order to find the best way of estimating it. Then, some solutions should be found to simulate the whole cooling stage of the process down to room temperature. By doing that, the simulated macro stress-strain curve could be compared to the experimental one already obtained. Moreover, several inclusions contents should be considered in the numerical model, as experimentally done. Otherwise, the evolution of the macro tensile damage parameters during cooling and during a subsequent tensile test should be compared to the evolutions of the experimental thermal D_{th} and mechanical D_{th+mec} parameters, previously introduced. Finally, it might be interesting to consider non-spherical inclusions in the model but the anisotropy of the cell may be, then, increased. Thus, new quasi-isotropic R.V.E. would have to be found, involving probably more inclusions and, therefore, more calculation resources.

References

[ADA-81] T.A. Adams, D.J. Landini, C.A. Schmacher, R.C. Bradt, Micro- and macro-crack growth in alumina refractories, Bull. Amer. Cer. Soc., 60 (7), 1981, 730-735.

[AIF-84] E. Aifantis, On the microstructural origin of certain inelastic models, Transactions of ASME, J. Mat. Engng. Tech., 106, 1984, 326-330.

[AKS-02] C. Aksel, B. Rand, F.L. Riley, P.D. Warren, Mechanical properties of magnesia-spinel composites, J. Eur. Ceram. Soc., 22 (5), 2002, 745-754.

[AKS-03a] C. Aksel, P.D. Warren, Work of fracture and fracture surface energy of magnesia-spinel composites, Compos. Sci. Technol., 63 (10), 2003, 1433-1440.

[AKS-03b] C. Aksel, P.D. Warren, Thermal shock parameters [R, R''' and R''''] of magnesia–spinel composites, J. Eur. Ceram. Soc., 23 (2), 2003, 301-308.

[AKS-03c] C. Aksel, F.L. Riley, Effect of the particle size distribution of spinel on the mechanical properties and thermal shock performance of MgO-spinel composites. J. Eur. Ceram. Soc., 23 (16), 2003, 3079-3087.

[AKS-04a] C. Aksel, B. Rand, F.L. Riley, P.D. Warren, Thermal shock behaviour of magnesia–spinel composites, J. Eur. Ceram. Soc., 24 (9), 2004, 2839-2845.

[AKS-04b] C. Aksel, P.D. Warren, F.L. Riley, Fracture behaviour of magnesia and magnesia-spinel composites before and after thermal shock, J. Eur. Ceram. Soc., 24 (8), 2004, 2407-2416.

[AKS-04c] C. Aksel, P.D. Warren, F.L. Riley, Magnesia–spinel microcomposites, J. Eur. Ceram. Soc., 24 (10-11), 2004, 3119-3128.

[ALZ-07] A. Alzina, E. Toussaint, A. Béakou, Multiscale modeling of the thermoelastic behavior of braided fabric composites for cryogenic structures, Int. J. Solids Struct., 44 (21), 2007, 6842-6859.

[AND-02] K. Andreev, H. Harmuth, Application of finite element modeling to the thermo-mechanical behaviour of refractories, In: Hendriks, Rots, editors, Finite elements in civil engineering applications, Swets & Zeitlinger, 2002, 61-67.

[AND-03] K. Andreev, H. Harmuth, FEM simulation of the thermo-mechanical behaviour and failure of refractories - a case study, J. Mater. Process. Tech., 143-144, 2003, 72-77.

[AST] www.code-aster.org

[AST-10] Modélisation non locale à gradient de déformation, Code Aster Reference Manual, Document R5.04.02, 2010.

[AUE-06] T. Auer, Ch. Manhart, H. Harmuth, Contributions to refractory fracture mechanical and fractographic investigations, RHI Bull., 2006, 38-42.

[AUS-32] Austria Patent No. 158208 (2 March 1932).

[BAD-07] P. Badel, V. Godard, J-B Leblond, Application of some anisotropic damage model to the prediction of the failure of some complex industrial concrete structure, Int. J. Solids Struct., 44 (18-19), 2007, 5848-5874.

[BAH-09] O. Bahloul, Evolutions en fonction de la température de propriétés élastiques de bétons réfractaires à base de carbure de silicium, Thesis, University of Limoges, 2009.

[BAZ-76] Z.P. Bazant, Instability, ductility and size effect in strain softening concrete, J. Eng. Mech., ASCE 102, 1976, 331-344.

[BAZ-83] Z.P. Bazant, B.H. Oh, Crack band theory for fracture of concrete, Mater. Struct. 16 RILEM, Paris, France, 1983, 155-177.

[BAZ-89] Z.P. Bazant, G. Pijaudier-Cabot, Measurement characteristic length nonlocal continuum, J. Eng. Mech., 115 (4), 1989, 755-767.

[BAZ-02] Z.P. Bazant, M. Jirasek, Nonlocal integral formulations of plasticity and damage: survey of progress, J. Eng. Mech. ASCE 128, 2002, 1119-1149.

[BEL-11] Y. Belhriti, Fracture mechanical investigations on refractories using wedge splitting test and digital image correlation , ENSCI final years internship report, Limoges, 2011.

[BER-57] V.P. Berdennikov, Measurement of surface tension of solids, Zh. Fiz. Khim., 5 (2-3), 1934, 358-371; summarized by V.K. Kuznetsov, Surface energy of solids, Her Majesty's Stationery Office, London,1957, 226-234.

[BIL-05] N. Bilger, F. Auslender, M., J.-C. Michel, H. Moulinec, P. Suquet, A. Zaoui, Effect of a nonuniform distribution of voids on the plastic response of voided materials: a computational and statistical analysis, Int. J. Solids Struct., 42 (2), 2005, 517-538.

[BLO-05] E. Blond, N. Schmitt, F. Hild, Ph. Blumenfeld, J. Poirier, Modelling of high temperature asymmetric creep behavior of ceramics, J. Eur. Ceram. Soc., 25 (11), 2005, 1819-1827.

[BOR-01] M. Bornert, T. Bretheau, P. Gilormini, Homogénéisation en mécanique des matériaux 1 - Matériaux aléatoires élastiques et milieux périodiques, Hermès Science Publications, 2001, 57-91.

[BOR-10] M. Bornert, R. Brenner, Modélisation du comportement des matériaux hétérogènes et composites, lecture given at the E.N.S.T.A., 10/02/2010.

[BOU-01] M. Boussuge, Some numerical approaches of creep, thermal shock, damage and delayed failure of ceramics and refractories, Bull. Mater. Sci., 24, 2001, 97-100.

[BOU-04] M. Boussuge, Thermo-mechanical behaviour: from ceramics to refractories, Advances in refractories for the metallurgical industries IV, In: M. Rigaud, C. Allaire, editors, Proceedings of the 43rd annual conference of metallurgists of CIM, 2004, 605-616.

[BRA-87] F. Bradley, A.C.D. Chaklader, A. Mitchell, Thermal stress fracture of refractory lining components. Part 1: Thermo-elastic analysis, Metall. Trans., 18B, 1987, 355-363.

[BRA-81] R.C. Bradt, Problems and possibilities with cracks in ceramics, Sci Ceram Vol. 11 Göteborg, Sweden: Swedish Ceramic Society, 1981, 349-360.

[BRA-04] R.C. Bradt, Fracture of Refractories, In: C.A. Schacht, ed, Refractories Handbook, Schacht Consulting Services, Pittsburgh, Pennsylvania, U.S.A., 2004, 11-38.

[BRA-85] D.J. Bray, Toxicity of chromium compounds formed in refractories, Bull. Amer. Ceram. Soc., 64, 1985, 1012-1026.

[BRI-08] G. Briche, N. Tessier-Doyen, M. Huger, T. Chotard, Investigation of the damage behaviour of refractory model materials at high temperature by combined pulse echography and acoustic emission techniques, J. Eur. Ceram. Soc., 28 (15), 2008, 2835-2843.

[BRO-66] W.F. Brown Jr., J.E. Srawley, Plane strain crack toughness testing of high-strength metallic materials, Amer. Soc. Test. Mater., Spec. Tech. Publ., 410, 1966, 13-15.

[BRU-85] F.W. Brust, T. Nishioka, S.N. Atluri, M. Nakagaki, Further studies on elastic-plastic stable fracture utilizing the T* integral, Eng. Fract. Mech., 22 (6), 1985, 1079-1103.

[BUC-99] G. Buchebner, H. Harmuth, Magnesia-hercynite bricks – an innovative burnt basic refractory, Proc. UNITECR 1999, Berlin, Germany, German Refractories Association, 1999, 201-203.

[CHA-88] J.L. Chaboche, Continuum damage mechanics, Part I: General concepts, J. Appl. Mech., 55, 1988, 59-64.

[CHA-92] J.L. Chaboche, Damage induced anisotropy: on the difficulties associated with the active/passive unilateral condition, Int. J. Damage Mech., 1, 1992, 148-174.

[CHA-93] J.L. Chaboche, Development of continuum damage mechanics for elastic solids sustaining anisotropic and unilateral damage, Int. J. Damage. Mech., 2, 1993, 311-329.

[CHA-05] N. Challamel, C. Lanos, C. Casandjian, Strain-based anisotropic damage modelling and unilateral effects, Int. J. Mech. Sci., 47, 2005, 459-473.

[CHI-85] Chien YT, Ko YC, High temperature fracture energy and thermal stress resistance parameter of bauxite brick, Am. Ceram. Soc. Bull., 64, 1985, 1017-1020.

[CHO-08] T. Chotard, J. Soro, H. Lemercier, M. Huger, C. Gault, High temperature characterization of Cordierite-Mullite refractory by ultrasonic means, J. Eur. Ceram. Soc., 28, 2008, 2129-2135.

[CHR-00] R. M. Christensen, Mechanics of cellular and other low-density materials, Int. J. Solids Struct., 37, 2000, 93-104.

[CHU-63] D.H. Chung, Elastic moduli of single crystal and polycrystalline MgO, Philos. Mag., 8 (89), 1963, 833-41.

[CLA-76] G.A. Clarke, W.R. Andrews, P. Paris, D.W. Schmidt, Single specimen test for Jic determination. Mechanics of crack growth, ASTM STP, N°590, 1976, 27-42.

[COB-56] R.L. Coble, W. D. Kingery, Effect of porosity on physical properties of sintered alumina, J. Am. Ceram. Soc., 39, 1956, 377-385.

[COO-82] S.C. Cooper, P.T.A. Hodson, Magnesia-magnesium aluminate spinel as a refractory, Trans. J. Br. Ceram. Soc., 81, 1982, 121.

[COR-02] F. Cormery, H. Welemane, A critical review of some damage models with unilateral effect, Mechanics Research Communications, 29, 2002, 391-395.

[CUT-93] T. Cutard, Caractérisation ultrasonore à haute température et sous contrainte de traction de composites céramique-céramique, Thèse, Université de Limoges, 1993.

[CUT-94] T. Cutard, D. Fargeot, C. Gault, M. Huger, Time delay and phase shift measurement for ultrasonic pulses using auto correlation methods, J. Appl. Phys., 75 (4), 1994, 1909-1913.

[DAL-88] R. Dal Maschio, B. Fabbri, C. Fiori, Industrial applications of refractories containing magnesium aluminate spinel, Industrial Ceramics, 8, 1988, 121-126.

[DAM-08] F. Damhof, W.A.M. Brekelmans, M.G.D. Geers, Non-local modeling of thermal shock damage in refractory materials, Eng. Fract. Mech., 75 (16), 2008, 4706-4720.

[DAM-11] F. Damhof, W.A.M. Brekelmans, M.G.D. Geers, Non-local modelling of cyclic thermal shock damage including parameter estimation, Eng. Fract. Mech., 78 (9), 2011, 1846-1861.

[DAV-79] R.W. Davidge, Mechanical behavior of ceramics, Cambridge University Press, 1979.

[DAY-64] R.B. Day, R.J. Stokes, Mechanical behavior of magnesium oxide at high temperature, J. Am. Ceram. Soc., 47 (10), 1964, 493-503.

[DRA-07] A.S. Drago, M-J. Pindera, Micro-macromechanical analysis of heterogeneous materials: Macroscopically homogeneous vs periodic microstructures, Compos. Sci. Technol., 67 (6), 2007, 1243-1263.

[DUB-03] J.F. Dubé, G. Pijaudier-Cabot, C. La Borderie, Modèle d'endommagement microplans, Revue Française de Génie Civil, 7, 2003, 621-634.

[FIC-97] S. Fichant, G. Pijaudier-Cabot, C. La Borderie, Continuum damage modelling: approximation of crack induced anisotropy, Mech. Res. Commun., 24, 1997, 109-114.

[GAI-06] Y. Gaillard, C. Tromas, J. Woirgard, Quantitative analysis of dislocation pile-ups nucleated during nanoindentation in MgO, Acta Mater., 54, 2006, 1409-1417.

[GAS-01] A. Gasser, P. Boisse, J. Rousseau, Y. Dutheillet, Thermomechanical behaviour analysis and simulation of steel/refractory composite linings, Compos. Sci. Technol., 61 (14), 2001, 2095-2100.

[GAS-05] A. Gasser, K. Terny-Rebeyrotte, P. Boisse, J. Poirier, A multi-scale approach for refractory structure modeling, In: Smith JD, editor, Proceedings of UNITECR 05, Am. Ceram. Soc., 2005, 998-1002.

[GAU-85] C. Gault, F. Platon, D. Le Bras, Ultrasonic measurement of Young Modulus of Al_2O_3-Based refractories at high temperatures, Mater. Sci. Eng., 74, 1985, 101-111.

[GEE-98] M.G.D. Geers, R. de Borst, W.A.M. Brekelmans, R.H.J. Peerlings, Strain-based transient-gradient damage model for failure analyses, Comput. Method. Appl. M., 160, 1998, pp 133-153.

[GIL-60] J.J. Gilman, Direct measurements of surface energies of crystals, J. Appl. Phys., 31 (12), 1960, 2208-2218.

[GIL-97] MAJ van Gils, LJMG Dortmans, G. de With, Thermal shock predictions for refractory ceramics, In: Hetnarski RB, Noda N, Ghoneim H, editors, Proceedings of the second international symposium on thermal stresses and related topics, Rochester Institute of Technology, 1997, 682-97.

[GOD-05] V. Godard, Modélisation de l'endommagement anisotrope du béton avec prise en compte de l'effet unilatéral: Application à la simulation numérique des enceintes de confinement, Thesis, University Paris VI, 2005.

[GOG-78] G.A. Gogotsi, Y.L. Groushevski, K.K. Strelov, The significance on non-elastic deformation in the fracture of heterogeneous ceramic materials, Ceramurgia International, 4 (3), 1978, 113-118.

[GOG-93] G.A. Gogotsi, The significance on non-elastic deformation in the thermal shock fracture of heterogeneous ceramic materials, In: Schnieder GA, Petzow G, eds, Thermal shock and thermal fatigue behaviour of advanced ceramics, NATO ASI Series E: Applied Sciences, 241, Dordrecht, The Netherlands: Kluwer Academic Publishers, 1993, 279-291.

[GRA-10] R. Grasset-Bourdel, A. Alzina, M. Huger, T. Chotard, R. Emler, D. Gruber, H. Harmuth, Development of a microstructural methodology to establish structure/property relations of refractories and first results for magnesia-spinel materials, in Editor's Oprea and Hemrick, *Advances in Refractories V*, The Canadian Institute of Mining, Metallurgy and Petroleum, Vancouver, 2010, 425-439.

[GRI-20] A.A. Griffith, Phenomena of rupture and flow in solids, Phil. Trans. Roy. Soc. (London), 221 A [4], 1920, 163-198.

[GRU-04] D. Gruber, K. Andreev, H. Harmuth, FEM simulation of the thermomechanical behaviour of the refractory lining of a blast furnace, J. Mater. Process. Tech., 155-156, 2004, 1539-1543.

[HAL-96] D. Halm, A. Dragon, A model of anisotropic damage by mesocrack growth: unilateral effect, Int. J. Damage Mech., 5, 1996, 384-402.

[HAR-95] H. Harmuth, Stability of crack propagation associated with fracture energy determined by wedge splitting specimen, Theor. and App. Fract. Mech., 23 (2), 1995, 103-108.

[HAR-96] H. Harmuth, K. Rieder, M. Krobath, E.K. Tschegg, Investigation of the nonlinear fracture behaviour of ordinary ceramic refractory materials, Mater. Sci. Eng. A, 214 (1-2), 1996, 53-61.

[HAR-97] H. Harmuth, E.K. Tschegg, A fracture mechanics approach to the development of refractory materials with reduced brittleness, Fatigue Fract. Eng. M., 20, 1979, 1585-1603.

[HAR-10a] H. Harmuth, Characterisation of the fracture path in 'flexible' refractories, 12th International Ceramics Congress CIMTEC 2010, June 6-11, Montecatini Terma, Italy, 2010.

[HAR-10b] H. Harmuth, R.C. Bradt, Investigation of refractory brittleness by fracture mechanical and fractographic methods, Interceram refractories, Refractories manual 2010, 6-10.

[HAS-62a] Z. Hashin and S. Shtrikman, On Some Variational Principles in Anisotropic and Nonhomogeneous Elasticity, J. Mech. Phys. Solids, 10, 1962, 335-342.

[HAS-62b] Z. Hashin, The Elastic Moduli of Heterogeneous Materials, J. Appl. Mech., 29 (1), 1962, 143-150.

[HAS-63a] Z. Hashin and S. Shtrikman, A Variational Approach to the Theory of the Elastic Behavior of Multiphase Materials, J. Mech. Phys. Solids, 11, 1963, 127-140.

[HAS-63b] D.P.H. Hasselman, Elastic energy at fracture and surface energy as design criteria for thermal shock, J. Am. Ceram. Soc., 46 (11), 1963, 535-540.

[HAS-69] D.P.H. Hasselman, Unified theory of thermal shock fracture intiation and crack propagation in brittle ceramics, J. Am. Ceram. Soc., 52 (11), 1969, 600-604.

[HEA-05] W.L. Headrick, M. Karukus, X. Laing, Refractory for black liquor gassifiers, University of Missouri-Rolla, Rolla, MO 65409-1130, DOE Award Number DEFC26-02NT41491, 2005.

[HEA-61] R.F.S. Hearmon, An introduction to applied anisotropic elasticity, Oxford university press, London, 1961.

[HEN-97] R.J. Henderson, H.W. Chandler, I. Strawbridge, A model for non-linear behaviour of refractories. Br. Ceram. Trans. J., 96 (3), 1997, 85–91.

[HEN-99] R.J. Henderson, H.W. Chandler, The fracture behaviour of dual phase composite refractories. In Engineering with Ceramics, ed. W. E. Lee and B. Derby, British Ceramic Proceedings 59, The Institute of Materials, 1999, 225-231.

[HIL-67] R. Hill, The essential structure of constitutive laws for metal composites and polycrystals, J. Mech. Phys. Solids, 15, 1967, 79-95.

[HIL-83] A. Hillerborg, Chapter 4.1 Analysis of one single crack, In: F.H. Wittman, Elsevier Science Publishers B.V., Fracture Mechanics of Concrete, Amsterdam, 1983, 223-249.

[HOM-80] J. Homeny, T. Darroudi, R.C. Bradt, J-integral measurements of the fracture of 50% m alumina refractories, J. Amer. Cer. Soc., 63 (5-6), 1980, 326-331.

[HUE-77] H. Huebner, W. Jillek, Sub-critical crack extension and crack resistance in polycrystalline alumina, J. Mater. Sci., 12, 1977, 117-125.

[HUE-90] C. Huet, Application of variational concepts to size effects in elastic heterogeneous bodies, J. Mech. Phys. Solids, 38 (6), 1990, 813-841.

[HUG-92] M. Huger, Oxydation et endommagement d'origine thermique évalués par techniques ultrasonores à haute température de composites SiC/C/SiC non protégés, Thesis, University of Limoges, 1992.

[HUG-02] M. Huger, D. Fargeot, C. Gault, High-temperature measurement of ultrasonic wave velocity in refractory materials, High Temp. - High Press., 34, 2002, 193-201.

[HUG-07] M. Huger, N. Tessier-Doyen, T. Chotard, C. Gault, Microstructural effects associated to CTE mismatch for enhancing the thermal shock resistance of refractories: investigation by high temperature ultrasounds, Ceram. For. Inter.fi/Ber.DKG, 84 (9), 2007, 93-103.

[IRW-58] G.R. Irwin, Encyclopedia of Physics, Vol. VI, Edited by Siegfried Flugge, Springer-Verlag, Berlin, 1958, 551-590.

[ISH-67] O. Ishai, L. J. Cohen, Elastic properties of filled and porous epoxy composites, Int. J. Mech. Sci., 9 (8), 1967, 539-546.

[JOL-07] Y. Joliff, J. Absi, M. Huger, J.C. Glandus, Experimental and numerical study of the room temperature elastic modulus of model materials with partly bonded matrix/particles interfaces, Comp. Mater. Sci., 39, 2007, 267-273.

[JOL-08] Y. Joliff, J. Absi, M. Huger, J.C. Glandus, Experimental and numerical study of the elastic modulus vs temperature of debonded model materials, Comp. Mater. Sci., 44 (2), 2008, 826-831.

[KAC-58] L.M. Kachanov, Time of the rupture process under creep conditions, Izv. Akad. Nauk., SSR. Otd. Tech. Nauk, 8, 1958, 26-31.

[KAK-07] M. Ghassemi Kakroudi, Comportement thermomécanique en traction de bétons réfractaires: influence de la nature des agrégats et de l'histoire thermique, Thesis, University of Limoges, 2007.

[KAK-08] M. Ghassemi Kakroudi, E. Yeugo-Fogaing, C. Gault, M. Huger, T. Chotard, Effect of thermal treatment on damage mechanical behaviour of refractory castables: Comparison between bauxite and andalusite aggregates, J. Eur. Ceram. Soc., 28, 2008, 2471-2478.

[KAK-09] M. Ghassemi Kakroudi, M. Huger, C. Gault, T. Chotard, Damage evaluation of two alumina refractory castables, J. Eur. Ceram. Soc., 29, 2009, 2211-2218.

[KAN-03] T. Kanit, Notion of Representative Volume Element for Heterogeneous Materials: Statistical and Numerical Approach, Thesis, Ecole Nationale Supérieure des Mines de Paris, 2003.

[KEI-89] A. Keisuke, Evaluation of thermal stress in refractory bricks by the finite element method, Taikabutsu Overseas, 10 (4), 1989.

[KER-62] F. Kerkhof, Synthetic materials: structure, physical behavior, and testing, Vol. I, Edited by Rudolf Nitsche and K.A. Wolf, Springer-Verlag, Berlin, 1962, 440-484.

[KIM-84] Kimura, Yasuda, Nishio, Development of magnesia spinel bricks for rotary cement kilns in Japan, Interceram, 1984 (Special Issue), 22-28.

[KIN-55] W.D. Kingery, Factors Affecting Thermal Stress Resistance of Ceramics Materials, J. Am. Ceram. Soc., 38 (1), 1955, 3-15.

[KNA-90] J. Knauder, R. Rathner, Thermo-mechanical analysis of basic refractories in a bottom blowing converter, Radex-Rundschau, 4, 1990, 354-364.

[LAG-92] J.-L. Lagrange, B. Passilly, M. Parlier, P. Colomban, Détermination des Propriétés Mécaniques Locales des Constituants de Composites Céramique-Céramique, C.R. 8ème Journées Nationales sur les Composites (JNC-8), Palaiseau, AMAC Paris, 1992.

[LAR-74] D.R. Larson, J.A. Coppola, D.P.H. Hasselman, R.C. Bradt, Fracture toughness and spalling behavior of high-Al_2O_3 refractories, J. Am. Ceram. Soc., 57 (10), 1974, 417-421.

[LIA-05] X. Liang, W.L. Headrick, L.R. Dharani, S. Zhao, J. Wei, Failure analysis of refractory cup under thermal loading and chemical attack using continuum damage mechanics, In: J.D. Smith, editor, Proceedings of UNITECR 05, The American Ceramic Society, 2005, 980-984.

[LOR-05] E. Lorentz, A. Benallal, Gradient constitutive relations: numerical aspects and application to gradient damage, Comput. Method. Appl. M., 194, 2005, pp 5191-5220.

[LUC-03] B.M. Luccioni, M.I. Figueroa, R.F. Danesi, Thermo-mechanic model for concrete exposed to elevated temperatures, Eng. Struct., 25, 2003, 729–742.

[LUT-91a] H.E. Lutz, N. Claussen, M.V. Swain, K^R-curve behavior of duplex ceramics, J. Amer. Cer. Soc., 74 (1), 1991, 11-18.

[LUT-91b] H.E. Lutz, M.V. Swain, Interrelation between flaw resistance, R-curve behavior and thermal shock strength degradation in ceramics, J. Amer. Cer. Soc., 74 (11), 1991, 2859-2868.

[LUT-91c] H.E. Lutz, N. Claussen, Duplex ceramics: II. Strength and toughness, J. Eur. Ceram. Soc., 7 (4), 1991, 219-226.

[MAC-50] J. K. Mackenzie, The elastic constants of a solid containing spherical holes, Proc. Phys. Soc. Lond. B, 63, 1950, 2-11.

[MAD-07] K. Madi, S. Forest, M. Boussuge, S. Gailliègue, E. Lataste, J.-Y. Bu_ère, D. Bernard, D. Jeulin, Finite element simulations of the deformation of fused-cast refractories based on X-ray computed tomography, Comp. Mater. Sci., 2007, 39 (1), 224-229.

[MAR-87] D.B. Marshall, J.E. Ritter, Reliability of advanced structural ceramics and ceramic matrix composites - A review, Am. Ceram. Soc. Bull., 66 (2), 1987, 309-317.

[MAR-88] D.B. Marshall, M.V. Swain, Crack resistance curves in magnesia-partially-stabilized zirconia, J. Am. Ceram. Soc., 71 (6), 1988, 399-407.

[MAT-08] J.D. Mathias, N. Tessier-Doyen, Homogenization of glass/alumina two-phase materials using a cohesive zone model, Comp. Mater. Sci., 43 (4), 2008, 1081-1085.

[MAT-04] K. Matsunaga, S. Ii, C. Iwamoto, T. Yamamoto, Y. Ikuhara, In situ observation of crack propagation in magnesium oxide ceramics, Institute Of Physics Publishing, Nanotechnology 15, 2004, S376–S381.

[MIC-99] J.C. Michel, H. Moulinec, P. Suquet, E_ective properties of composite materials with periodic microstructure: a computational approach, Comput. Method. Appl. M., 172, 1999, 109-143.

[MIS-01] L.L. Mishnaevsky Jr, S. Schmauder, Continuum mesomechanical finite element modeling in materials development: A state-of-the-art review, Appl. Mech. Rev., 54 (1), 2001, 49-74.

[MOE-99] N. Moës, J. Dolbow, T. Belytschko, A finite element method for crack growth without remeshing, Int. J. Numer. Meth. Eng., 46 (1), 1999, 131-150.

[MOU-98] H. Moulinec, P. Suquet, A numerical method for computing the overall response of nonlinear composites with complex microstructure, Comput. Method. Appl. M., 1998, 157, 69-94.

[MUR-97] S. Murakami, K. Kamiya, Constitutive and damage evolution equations of elastic-brittle materials based on irreversible thermodynamics, Int. J. Mech. Sci., 39 (4), 1997, 473-486.

[NAK-64] J. Nakayama, Bending method for direct measurement of fracture energy of brittle material, Japan. J. Appl. Phys., 3 (7), 1964, 422-423.

[NAK-65] J. Nakayama, Direct measurement of fracture energies of brittle heterogeneous materials, J. Am. Ceram. Soc., 48 (11), 1965, 583-587.

[NAK-66] J. Nakayama, M. Ishizuka, Experimental evidence for thermal shock damage resistance, Amer. Ceram. Soc. Bull., 45 (7), 1966, 666-669.

[NEM-93] S. Nemat-Nasser, M. Hori, Micromechanics: overall properties of heterogeneous materials, North-Holland, Amsterdam (Netherland), 1993.

[NEM-99] S. Nemat-Nasser, M. Hori, Micromechanics-Overall Properties of Heterogeneous Materials (2nd ed.), North-Holland/Elsevier, Amsterdam, 1999, 1-786.

[NEN-02] W. Nentech, F. Meftah, J.M. Reynouard, An elasto-plastic damage model for plain concrete subjected to high temperatures, Eng. Struct., 24, 2002, 597-611.

[OLI-92] W.C. Oliver, G. M. Pharr, An improved technique for determining hardness and elastic modulus using load and displacement sensing indentation experiments, J. Mater. Res., 7 (6), 1992, 1564-83.

[OST-08] M. Ostoja-Starzewski, Microstructural randomness and scaling in mechanics of materials, Boca Raton: Chapman & Hall/CRC, 2008.

[PAB-04] W. Pabst, E. Gregorova, New relation for the porosity dependence of the effective tensile modulus of brittle materials, J. Mater. Sci., 39, 2004, 3501-3503.

[PAB-06] W. Pabst, E. Gregorova, G. Ticha, Elasticity of porous ceramics-A critical study of modulus-porosity relations, J. Eur. Ceram. Soc, 26, 2006, 1085-1097.

[PAL-93] S. Paletto, G. Fantozzi, Nanoindentation: Théorie et Applications, Rev. Comp. Mater. Avancés, 3 (2), 1993, 139-160.

[PAP-74] E.P. Papadakis, Ultrasonic measurements of Young's modulus and extensional wave attenuation in refractory: Metal wires at elevated temperature with application to ultrasonic thermometry, J. Appl. Phys., 45(6), 1974, 2409-2420.

[PAT-09] C. Patapy, C. Gault, M. Huger, T. Chotard, Acoustic characterization and microstructure of high zirconia electrofused refractories, J. Eur. Ceram. Soc., 29 (16), 2009, 3355-3362.

[PAT-10] C. Patapy, A. Proust, D. Marlot, M. Huger, T. Chotard, Characterization by acoustic emission pattern recognition of microstructure evolution in a fused-cast refractory during high temperature cycling, J. Eur. Ceram. Soc., 30 (15), 2010, 3093-3101.

[PAT-70] M.S. Paterson, C.W. Weaver, Deformation of polycrystalline MgO under pressure, J. Am. Ceram. Soc., 53 (8), 1970, 463-471.

[PEE-95] R.H.J. Peerlings, R. de Borst, W.A.M. Brekelmans, J.H.P. de Vree, Computational modelling of gradient-enhanced damage for fracture and fatigue problems of plain concrete, In: Owen, D.R.J., Onate, E. (Eds.), Computational Plasticity, Fundamentals and Applications, 1995, 975–986.

[PEE-96] R.H.J. Peerlings, R. de Borst, W.A.M. Brekelmans, J.H.P. de Vree, Gradient enhanced damage for quasi-brittle materials, Int. J. Numer. Meth. Eng., 39, 1996, 3391-3403.

[PEE-01] R.H.J. Peerlings, M.G.D. Geers, R. de Borst, W.A.M. Brekelmans, A critical comparison of nonlocal and gradient-enhanced softening continua, Int. J. Solids Struct., 38, 2001, 7723-7746.

[PIJ-87] G. Pijaudier-Cabot, Z.P. Bazant, Nonlocal damage theory, J. Eng. Mech., ASCE 113, 1987, 1512-1533.

[PIE-81] S. Pietruszczak, Z. Mroz, Finite element analysis of deformation of strain softening materials, Int. J. Numer. Meth. Eng., 17, 1981, 327-334.

[PIN-07] M.J. Pindera, Y. Bansal, On the micromechanics-based simulation of metal matrix composite response, J. Eng. Mater. Technol., 129 (3), 2007, 468-482.

[PIN-09] M.J. Pindera, H. Khatam, A.S. Drago, Y. Bansal, Micromechanics of spacially uniform heterogeneous media: a critical review and emerging approaches, Composites: Part B, 40, 2009, 349-378.

[POP-99] E.P. Popov, In "Engineering Mechanics of Solids", Upper Saddle River, NJ: Prentice Hall, 1999, 111-115.

[PRO-01] N. Prompt, E. Ouedraogo, T. Joly, P. Stutz, Thermo-mechanical modeling of a refractory structure: the wear layer of a blast furnace trough, In: Proceedings of UNITECR 01, Am. Ceram. Soc., 2001, 282-288.

[QI-09] B. Qi, J. Absi, N. Tessier-Doyen, Experimental and numerical study of the Young's modulus vs temperature for heterogeneous model materials with polygonal inclusions, Comp. Mater. Sci., 46 (4), 2009, 996-1001.

[REU-29] A. Reuss, Berechnung der Fliessgrenze von Mischkristallen auf Grund der Plastizitätsbedingung für Einkristalle, Z. angew. Math. u. Mech., 9 (1), 1929, 49-58.

[RIC-68] J.R. Rice, A path independent integral and the approximate analysis of strain concentration by notches and cracks, J. App. Mech., 35 (6), 1968, 379-386.

[RIT-88] R.O. Ritchie, Mechanisms of fatigue crack propagation in metals, ceramics, and composites: role of crack-tip shielding, Mater. Sci. Eng., A103, 1988, 15-28.

[ROE-56] F.C. Roesler, Brittle fractures near equilibrium, Proc. Phys. Soc. (London), 69 (442B), 1956, 981-992.

[ROS-86] L.R.F. Rose, M.V. Swain, Two R curves for partially stabilized zirconia, J. Am. Ceram. Soc., 69 (3), 1986, 203-207.

[ROS-70] B. W. Rosen, Z. Hashin, Effective Thermal Expansion Coefficients and Specific Heats of Composite Materials, Int. J. Eng. Sci., 8, 1970, 157-173.

[RUB-99] D. Rubesa, Thermal stress fracture and spalling of well blocks in steel ladles - modeling and numerical simulation, Veitsch-Radex Rundschau, 2, 1999, 3-24.

[SAK-86] M. Sakai, R.C. Bradt, Graphical methods for determining the nonlinear fracture parameters of silica and carbon refractory composites, In: Bradt RC et al. eds. Fract Mech of Ceramics, Vol VII, New York, NY: Plenum Publishing Corp., 1986, 127-142.

[SAK-92] M. Sakai, H. Ichikawa, Work-of-fracture of brittle materials with microcracking and crack bridging, Int. J. Fracture, 55 (1), 1992, 65-80.

[SAK-93] M. Sakai, R.C. Bradt, Fracture toughness testing of brittle materials, Int. Mat. Reviews, 38 (2), 1993, 53-78.

[SAN-07] C.M. Sands, R.J. Henderson, H.W. Chandler, A three dimensional computational model of the mechanical response of a dual-phase ceramic, Comp. Mater. Sci., 39 (4), 2007, 862-870.

[SCH-02] N. Schmitt, A. Burr, Y. Berthaud, J. Poirier, Micromechanics applied to the thermal shock behaviour of refractory ceramics, Mech. Mater., 34 (11), 2002, 725-747.

[SCH-93a] G.A. Schneider, G. Petzow, eds, Thermal shock and thermal fatigue behaviour of advanced ceramics, NATO ASI Series E: Applied Sciences, 241, Dordrecht, The Netherlands: Kluwer Academic, 1993.

[SCH-93b] J.P. Schneider, B. Coste, Thermo-mechanical modeling of thermal shock in anodes, In: Proceedings of the conference on light metals, The Minerals, Metals & Materials Society, 1993.

[SCH-94] W. Schulle, V.T. Anh, J. Ulbricht, Improvement of the thermal shock resistance of magnesia refractories by special microstructures (in German), Stahl und Eisen, Special Issue October 1994 (37. Int. Refract. Congr., Aachen, Germany), 132-135.

[SHA-61] E.B. Shand, Fracture velocity and fracture energy of glass in the fracture range, J. Am. Ceram. Soc., 44 (1), 1961, 21-26.

[SIM-00] F. Simonin, C. Olagnon, S. Maximilien, G. Fantozzi, L.A. Diaz, R. Torrecillas, Thermo-mechanical behaviour of high-alumina refractory castables with synthetic spinel additions, J. Am. Ceram. Soc., 83, 2000, 2481-2490.

[SOA-91] J.S. Soady, S. Plint, A quantitative thermal shock approach to the development of magnesia-spinel refractories for the cement kiln, UNITECR 91, Aachen, Germany, 1991, 443-449.

[SPO-95] P. S. Spoor, J.D. Maynard, A. R. Kortan, Elastic isotropy and anisotropy in quasicrystalline and cubic AlCuLi, Phys. Rev. Lett., 75, 1995, 3462-3465.

[SPR-61] R.M. Spriggs, Expression for effect of porosity on elastic modulus of polycrystalline refractory materials, particularly aluminum oxide, J. Am. Ceram. Soc., 44, 1961, 628-629.

[STE-83] R.W. Steinbrech, R. Knehans, W. Schaarwaechter, Increase of crack resistance during slow crack growth in Al_2O_3 bend specimens, J. Mater. Sci., 18, 1983, 265-270.

[STO-63] R.J. Stokes, C.H. Li, Dislocations and the tensile strength of magnesium oxide, J. Am. Ceram. Soc., 46 (9), 1963, 423-434.

[SUQ-83] P. Suquet, Analyse limite et homogénéisation, C.R. Acad. Sci. Paris, Série II, 296, 1983, 1355-1358.

[SUQ-87] P. Suquet, Elements of homogenization for inelastic solid mechanics, in E. Sanchez-Palencia and A. Zaoui, eds, Homogenization Techniques for Composite Media, volume 272 of Lecture Notes in Physics, Springer, Berlin, 1987, 193-278.

[SWA-83] M.V. Swain, R-curve behavior of magnesia-partially stabilised zirconia and its significance to thermal shock, Fracture Mechanics of Ceramics, Vol. 6. Edited by R.C. Bradt A.G. Evans, D.P.H. Hasselman, F.F. Lange, Plenum Press, New York, 1983, 345-359.

[SWA-90] M.V. Swain, R-curve behavior and thermal shock resistance of ceramics, J. Am. Ceram. Soc., 73 (3), 1990, 621-628.

[TAB-92] W. Tabber, H.J. Klischat, Magnesia-spinel bricks for the cement industry, Proceedings Beijing China Symposium, China, 1992, 424-430.

[TAN-95] D.M. Tan, K.A. Rieder, H. Harmuth, E.K. Tschegg, Determination of R-curves of ordinary refractory ceramics from measurements of a new wedge splitting test method, Fortschrittsberichte der Deutschen Keramischen Gesellschaft, 1995, 71-76.

[TAT-66] H.G. Tattersall, G. Tappin, Work of fracture and its measurement in metals and ceramics, J. Mat. Soc., 1 (3), 1966, 296-301.

[TES-03] N. Tessier-Doyen, Etude expérimentale et numérique du comportement thermomécanique de matériaux réfractaires modèles, Thesis, University of Limoges, 2003.

[TES-06] N. Tessier-Doyen, J.C. Glandus, M. Huger, Untypical Young's modulus evolution of model refractories at high temperature, J. Eur. Cer. Soc., 26 (3), 2006, 289-295.

[TES-07] N. Tessier-Doyen, J.C. Glandus, M. Huger, Experimental and numerical study of elastic behavior of heterogeneous model materials with spherical inclusions, J. Mater. Sci., 2007, 42, 5826-5834.

[TOK-91] K. Tokunaga, H. Kozuka, T. Honda, F. Tanemura, Further improvements in high temperature strength, coating adherence, and corrosion resistance of magnesia-spinel bricks for rotary cement kiln, UNITECR 91, Aachen, Germany, 1991, 431-435.

[TSC-86] E.K. Tschegg, Equipment and appropriate specimen shapes for tests to measure fracture values, 31.1.1986, AT no. 390328, Austrian Patent Office, Austria (Prüfeinrichtung zur Ermittlung von bruchmechanischen Kennwerten sowie hiefür geeignete Prüfkörper, 31.1.1986, Patentschrift Nr. 390328).

[TSC-91] E.K. Tschegg, New equipment for fracture tests on concrete, Mater. Test. (Mater), 33, 1991, 338-342.

[TSC-94] E.K. Tschegg, H. Harmuth, Lasteinleitungsvorrichtung für Hochtemperaturprüfungen, Patent. 402767, Österr: Patentamt Vienna, 1994.

[TSC-09] E.K. Tschegg, K.T. Fendt, Ch. Manhart, H. Harmuth, Uniaxial and biaxial fracture behaviour of refractory materials, Eng. Fract. Mech., 76, 2009, 2249-2259.

[TVE-97] V. Tvergaard, Studies of void growth in a thin ductile layer between ceramics, Comput. Mech., 20, 1997, 184-191.

[UCH-76] J.J. Uchno, R.C. Bradt, D.P.H. Hasselman, Fracture surface energies of magnesite refractories, Ceram. Bull., 55 (7), 1976, 665-668.

[VOI-1887] W. Voigt, Theoretische Studien über die Elasticitätsverhältnisse der Krystalle, Abh. Kgl. Ges. Wiss. Göttingen, Math. Kl, 34, 1887, 3-51.

[WAC-09] J.B. Wachtman, Mechanical properties of Ceramics, 2nd ed. W. R. Cannon, M.J. Matthewson, Wiley & Sons, Inc., Publication, 2009.

[WEI-95] S. Weihe, B. Kroeplin, Fictitious crack models: A classification approach, Proc FRAMCOS II (2nd Int Conf Fracture Mechanics of Concrete and Concrete Structures), F.H. Wittmann (ed), Aedificatio Publ, 2, 1995, 825-840.

[WEI-98] S. Weihe, B. Kroeplin, R. de Borst, Classification of smeared crack models based on material and structural properties, Int. J. Solids Struct., 35 (12), 1998, 1289-1308.

[WIE-64] S.M. Wiederhorn, Fracture surface energy of soda-lime glass, Proceedings of conference on role of grain boundaries and surfaces in ceramics, North Carolina State (USA), 1964.

[YAN-04] Q.S. Yang, W. Becker, Numerical investigation for stress, strain and energy homogenization of orthotropic composite with periodic microstructure and non-symmetric inclusions, Comp. Mater. Sci., 31, 2004, 169-180.

[ZEN-48] C. Zener, Elasticity and Anelasticity of Metals, University of Chicago Press, Chicago, 1948, 160-163.

Abstract :

The present thesis aimed at investigating the relationships which exist between the microstructure of refractories and their thermomechanical properties, and especially, better understanding the microstructure key-points allowing to develop a non-linear mechanical behaviour. From the grain size distribution of industrial magnesia-spinel materials, used in cement rotary kilns for their thermal shock resistance, simpler two-phase materials, composed of a magnesia matrix and spinel inclusions, were elaborated with different spinel contents. The thermal expansion mismatch between spinel and magnesia induces, during cooling, matrix microcracking around the spinel inclusions. The experimental part allowed to clarify, and quantify, the thermal damage occurrence during the cooling stage within these magnesia-spinel composites, in relation with their spinel inclusions content. Then, the influence of this thermal damage on the non-linearity of the mechanical behaviour of these composites was studied. The main objective of the numerical part was to build a consistent 3D FEM model able to well depict the microcracks occurence within these magnesia-spinel materials during a uniform temperature decrease beginning at high temperature (stress-free state) and able to provide, after this cooling step, a macroscopic non-linear mechanical behaviour. The design of simple, but quasi-isotropic, Representative Volume Elements (R.V.E) by periodic homogenisation, and the use of an anisotropic damage model, with a regularisation method, have allowed to simulate, locally, the matrix microcracking around the inclusions during cooling, and the damage growth in the volume during a subsequent tensile test. Moreover, the global evolutions of homogenised simulated parameters, during both the cooling stage and the tensile test, were in good agreement with previous macro-scaled experiments results.

Keywords : Refractories, thermal shock resistance, mechanical behaviour, magnesia-spinel materials, thermal expansion mismatch, microcracks, homogenisation methods, FEM damage model.

Résumé :

Cette thèse avait pour objectif d'étudier les relations existant entre la microstructure de matériaux réfractaires et leurs propriétés thermomécaniques, et, en particulier, à mieux comprendre les paramètres microstructuraux clés permettant de développer un comportement mécanique non-linéaire. A partir de la distribution granulométrique de matériaux magnésie-spinelle industriels, utilisés dans les fours rotatifs de cimenterie pour leur résistance aux chocs thermiques, des matériaux biphasés simplifiés, constitués d'une matrice de magnésie et d'inclusions de spinelle, ont été élaborées en intégrant différentes teneurs en inclusions. Le différentiel de dilatation thermique entre le spinelle et la magnésie induit, pendant le refroidissement, de la microfissuration matricielle autour des inclusions de spinelle. La partie expérimentale de cette étude a permis de clarifier, et de quantifier, le développement de l'endommagement thermique au sein de ces composites magnésie-spinelle durant l'étape de refroidissement, en relation avec leur teneur en inclusions de spinelle. L'influence de cet endommagement thermique sur la non-linéarité du comportement mécanique de ces composites a, ensuite, été étudiée. L'objectif principal de la partie numérique était de construire un modèle 3D, par méthode éléments finis, capable de décrire la microfissuration au sein de ces matériaux magnésie-spinelle pendant l'étape de refroidissement post-frittage (haute température = état de contraintes nulles), et pouvant entraîner, après cette étape, un comportement mécanique macroscopique non-linéaire. La conception de Volumes Elémentaires Représentatifs (V.E.R.) simples, mais quasi-isotropes, associée à l'utilisation d'une méthode d'homogénéisation périodique, et à la mise en œuvre d'un modèle d'endommagement anisotrope, ont permis de simuler localement la microfissuration matricielle autour des inclusions pendant le refroidissement, ainsi que la croissance de l'endommagement au sein du volume pendant l'essai de traction. Ainsi, les évolutions globales de paramètres simulés homogénéisés, aussi bien pendant le refroidissement que pendant l'essai de traction, se sont avérées être en bon accord avec des résultats expérimentaux obtenus à l'échelle macroscopique.

Mots clés : Réfractaires, résistance aux chocs thermiques, comportement mécanique, matériaux magnésie-spinelle, différentiel de dilatation thermique, microfissures, méthodes d'homogénéisation, modèle numérique d'endommagement.